Kinetic Modeling of Pyruvate Recycling Pathways in Pancreatic β-Cells.

by

Rahul Rahul

A thesis
presented to the University of Waterloo
in fulfillment of the
thesis requirement for the degree of
Doctor of Philosophy
in
Applied Mathematics

Waterloo, Ontario, Canada, 2012

I hereby declare that I am the sole author of this thesis. This is a true copy of the thesis, including any required final revisions, as accepted by my examiners.

I understand that my thesis may be made electronically available to the public.

Abstract

A variety of signaling mechanisms are employed to maintain healthy levels of glucose in the blood stream. The hormone insulin is one of the primary regulators of glucose homeostasis. Insulin, which activates glucose uptake, is released from pancreatic β-cells in a bi-phasic manner. The first phase is triggered by increased ATP levels in the cell. The second release phase is triggered by the so-called amplifying pathway [37, 80], which has not been fully characterized. Recent experimental evidence indicates that pyruvate-recycling pathways are key components of the amplifying pathway. The fuel intermediates from these pathways may be the signaling factors that couple insulin-release to glucose availability. The co-factor nicotinamide adenine dinucleotide phosphate (NADPH) has been identified as a putative coupling factor. In this work we develop a kinetic model for the tricarboxylic acid cycle and pyruvate recycling pathways, building on the previous modeling efforts of Westermark *et al.* [110]. and Yugi and Tomita [116]. We successfully validated the model against recent experimental observations. Analysis of the model provides predictions of the flux distributions in the pyruvate recycling pathways. Moreover, model simulations provides hypotheses to guide further experimental investigation, and suggest potential drug targets for treatment of type 2 diabetes.

Acknowledgments

The graduate studies for me has been a process of evolution into a completely new personality. My gratitude towards my supervisor Dr. Brian Ingalls is as boundless as the universe, for all the support and guidance he provided to me. He graciously tolerated my slow learning ability and pathetic writing skills. I would also like to thank Prof. Sue Ann Campbell, Prof. Edward R. Vrscay and Prof. Kevin lamb for their support and motivation. I would like say special thanks to my masters degree supervisor Dr. Supratim Sengupta for his invaluable support without which I could not have came this far. I would also like to thank my committee members, Dr. Matthew Scott, Dr. Mohammad Kohandel, Dr. Jamie Joseph, and Dr. Sivabal Sivaloganathan for their support and motivation.

I am indebted to my friends who walked along side me through out the degree program. I would like to say special thanks to my office mate Dr. Matthew Douglas Johnston for keeping up with me all along the year during my degree program. I would like to say special thanks to Vris Yuen-Lam Cheung, Amenda Chow, Leanne Elise Stuive, Alex shum, Chris Morley, Joshua Fletcher, Yasunori Aoki and Dhanaraja Kasinathan for their invaluable contributions which they made in developing my math and teaching skills. I would like to say special thanks to Dr. Abdullah Hamadeh, Dr. Mohamad Alwan, Dr. Hamid Molavian, Dr. Hongtao Zhang, and Dr. Easwar Magesan for their advice's and motivation. I would like to say special thanks to my soccer teammates: Nancy Soontiens, Dr. Marek Stastna, Michael Dunphy, Kristopher Rowe and Wentao Liu. This list will be incomplete if I don't thank Andrew Belatos for being my music guide. I would like to extend my heartiest thanks to all my friends who walked along side me whom I might have missed in this list.

Finally, but not least I would like to acknowledge my family members for their affection and support. My elder brother Parimal Samir has been a exceptional guide and mentor through out my journey of life. I would like to conclude by extending my gratitude towards my parents Uday Shankar Sharma, Sushila Sharma and sister in law Aditi Galoda.

Dedication

This thesis is dedicated to my parents, brother, and my supervisors Dr. Brian Ingalls, and Dr. Supratim Sengupta who always supported and motivated me.

Table of Contents

List of Tables

List of Figures

Chapter 1

Introduction

Type 2 diabetes is characterized by the functional failure of pancreatic β-cells to regulate insulin secretion. β-cells function as glucose sensors; they release the hormone insulin into the blood stream when the glucose level increases above a threshold value. Insulin promotes glucose uptake in peripheral tissue and suppresses the release of stored lipids from adipose tissue. In type 2 diabetes, patients develop insulin resistance. That is, the release of insulin does not activate any cellular response. Another symptom is the failure of β-cells to synchronize insulin release with changing levels of glucose; insulin release by β-cells becomes irregular. In the later stages of the disease, both impaired insulin release and insulin resistance are typically observed. This leads to partial loss of β-cell mass, making the disease chronic. Type 2 diabetes is predominant in adults, especially those who are obese and exhibit sedentary behavior. The prevalence of the disease has lead to a major thrust for the development of drugs to treat type 2 diabetes. An in depth understanding of the complexity of insulin signaling would be helpful in identifying the candidate drug

targets.

The functional failure of β-cells in type 2 diabetes affects these cells ability to properly regulate insulin secretion when the glucose level is elevated in the blood stream. This glucose-derived signaling, which is the primary regulator of insulin secretion by β-cells, is called glucose-stimulated insulin-secretion (GSIS). Any related molecules that are downstream products of glucose metabolism are defined as glucose-derived potentiators of insulin secretion.

The mechanisms by which elevated glucose levels trigger the release of insulin have not been fully characterized. It has been observed that GSIS is bi-phasic. The initial release phase involves a sequence of processes known as the K_{ATP}-dependent pathway: increased glucose metabolism increases the ratio of cytosolic adenosine triphosphate (ATP) to adenosine diphosphate (ADP) causing closure of ATP-dependent potassium (KATP) channels; depolarization of the cell membrane follows, causing an influx of Ca^{2+}, which triggers insulin vesicle exocytosis [81, 82]. This first phase of insulin release, known as the triggering signal, occurs within ten minutes following glucose stimulation [37, 76]. The second release phase follows after the first, and is more sustained. It is prompted by the *K_{ATP}-independent pathway*, also known as the *amplifying pathway* [37, 80]. The initial discovery that the two pathways are independent [37] prompted a search for non-ATP-related metabolic responses to increased glucose availability. A full understanding of glucose-stimulated insulin-secretion will require characterization of the metabolic signaling mechanisms responsible for both release phases.

Initial studies of the amplifying pathway focused on the metabolism of pyruvate in the mitochondria. In most cell types, pyruvate feeds the tricarboxylic acid (TCA) cycle via the enzyme pyruvate dehydrogenase (PDH), which generates acetyl-CoA. β-cells are one of the few cell-types that express significant quantities of the enzyme pyruvate carboxylase (PC), which provides an alternative route from pyruvate to the TCA cycle (producing mitochondrial oxaloacetate (OAA) from pyruvate, see Figure 1.1). In β-cells, pyruvate flows into mitochondrial pathways through these enzymes in approximately equal proportion [63, 99, 56, 64, 7, 11, 45]. Pyruvate that enters the TCA cycle via pyruvate carboxylase can readily be recycled back to pyruvate, either directly from OAA (via PC) or after further metabolism of OAA in the TCA cycle, possibly involving both metabolic and cytosolic enzyme activity [65]. The experiments of Lu *et al.* [63] revealed that GSIS is related to PC-catalyzed pyruvate recycling, while PDH-catalyzed conversion of pyruvate to acetyl-coA does not play a significant role in GSIS. PC-based pyruvate recycling involves regeneration of pyruvate from TCA cycle intermediates via three distinct pathways (Figure 1.1): the pyruvate/malate cycle, the pyruvate/citrate cycle, and the pyruvate/isocitrate cycle [66]. Each cycle begins with the conversion of mitochondrial pyruvate to mitochondrial oxaloactetate and ends with the conversion of malate to pyruvate by malic enzyme. (Malic enzyme is active in both the mitochondria and the cytosol; in β-cells, the cytosolic form carries the vast majority of the pyruvate recycling flux.)

The pyruvate/malate cycle involves conversion of mitochondrial OAA to malate, via mitochondrial malate dehydrogenase. Mitochondrial malate then follows one of two routes: it can be directly converted to pyruvate by mitochondrial malic enzyme (MEm), or it can

be transported to the cytosol via the dicarboxylate carrier (DIC) and then converted back to pyruvate by cytosolic malic enzyme (MEc).

The pyruvate/citrate cycle also begins with OAA following its normal route through the TCA cycle: it combines with Acetyl-CoA to form citrate (via citrate synthase (CS)). This mitochondrial citrate can then be converted to isocitrate by mitochondrial aconitase (ACOm). Mitochondrial citrate and isocitrate are transported into the cytosol by the citrate-isocitrate carrier (CIC). The cytosolic form of aconitase (ACOc) can then convert isocitrate to citrate. Cytosolic citrate lyase (CLc) converts citrate to oxaloacetate (releasing Acetyl-CoA). This cytosolic OAA can then be converted to malate by the cytosolic form of malate dehydrogenase (MDHc). Finally malate is converted to pyruvate by malic enzyme, thus completing the cycle. (This last step is shared with the pyruvate/malate cycle.)

Like the pyruvate/citrate cycle, the pyruvate/isocitrate cycle also starts with oxaloacetate being converted to citrate and isocitrate and the subsequent exit of these metabolites from the mitochondria through the citrate/isocitrate carrier (CIC). In the cytosol, citrate is converted to isocitrate by ACOc. Isocitrate is then converted to α-ketoglutarate (α-KG) by cytosolic NADP-dependent isocitrate dehydrogenase enzyme (ICDc). α-KG is then transported back into the mitochondria by the oxoglutarate carrier (OGC). Once in the mitochondria, α-KG follows the normal TCA reaction chain to be converted to malate, which can then be converted back to pyruvate by malic enzyme. (Again, this last step is shared with the other cycles.)

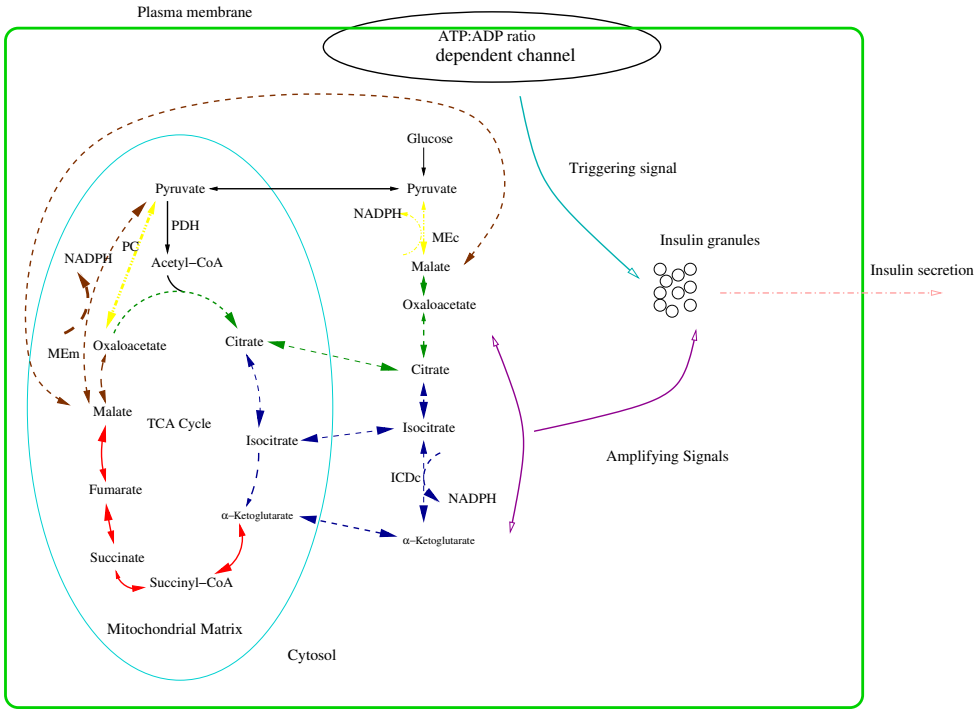

Figure 1.1: Pyruvate recycling pathways and the and amplifying signal for insulin release. The yellow arrows in the metabolic pathway indicate pyruvate carboxylase and malic enzyme, which are shared by all the three pyruvate recycle pathway. The brown arrows are for pyruvate-malate cycle, green arrows are for pyruvate-citrate cycle, and blue arrows are for pyruvate-isocitrate cycle. The red arrows shows the alternative possibility of completing the pyruvate-isocitrate cycle.

In recent years, studies have focused on the identification of metabolic coupling factors (MCF) which may act as signals in the amplifying pathway. These studies, provide growing evidence that the pyruvate-recycling pathways generate a metabolic factor that couples increased glucose consumption to insulin release [49, 88, 50, 58, 87]. A number of MCFs have been proposed, including NADPH, α-ketoglutarate (or its derivatives), and guanosine-5'-triphosphate (GTP) (generated by the succinylCoA dehydrogenase (SCS) [66, 76]. Recent observations suggest that NADPH is a key signaling molecule [88, 65]. NADPH is a byprod-

uct of all of the pyruvate recycling pathways [64]; it is generated by malic enzyme (a step shared by all three cycles), and, in the pyruvate/isocitrate pathway, by isocitrate dehydrogenase; this enzyme has recently received significant attention because its silencing was found to affect GSIS [88].

When addressing a complex metabolic network like the TCA cycle, it can be difficult to predict the effects of individual genetic or biochemical perturbations on the entire system. Kinetic modeling provides a framework for addressing the network in a systematic and quantitative manner. Furthermore, kinetic modeling provides a mathematical framework for analysis of temporal, genotypic and phenotypic changes associated with the metabolic pathway. Analysis of kinetic models aids in the interpretation of experimental data and can help in designing further experiments to elucidate the underlying biological process.

A number of computational models have been developed to describe aspects of the TCA cycle and GSIS. Westermark *et al.* [110] developed a model of mitochondrial nicotinamide adenine dinucleotide (NADH) shuttling (involving 10 metabolites and 19 enzymatic reactions). They validated the model against the findings of Eto *et al.* [23] which characterize the NADH shuttle in β-cells. The TCA cycle has been the subject of many modeling studies. A detail model of mitochondrial metabolism was recently developed by Yugi and Tomita [116]. Their model describes 58 enzymatic reactions involving 117 metabolites, and incorporates four pathways: the respiratory chain, the TCA cycle, fatty acid β oxidation, and the inner membrane transport system. Jiang *et al* [47] developed a detailed model of GSIS that describes 44 enzymatic reactions and 59 metabolic state variables. Their model

describes five metabolic pathways: glycolysis, the TCA cycle, the respiratory chain, NADH shuttling, and the pyruvate cycle. While these studies involve validation against a range of experimental findings, a systematic corroboration with experimental results on pyruvate recycling has not been attempted.

In this study, we build on these previous efforts by developing a mathematical model of β-cell metabolism that describes pyruvate recycling. Our model describes the TCA cycle, the pyruvate/malate shuttle, the pyruvate/citrate shuttle, and the pyruvate/isocitrate shuttle, as shown in Figure 1.1. The model describes 24 metabolites involved in 30 enzymatic reactions; it draws elements from the models of Yugi and Tomita [116], Westermark *et al.* [110] and Sweet and Matschinsky [108]. The model involves 123 parameters; 89 were taken directly from the literature, 34 were calibrated by fitting to the experimental observations of Ronnebaum *et al.* [88]. We tested the model's accuracy by comparing model predictions to qualitative and quantitative observations of system behavior as reported in the literature on β-cell metabolism [49, 50, 63, 45]. Once we had confirmed the validity of the model, we carried out local and global sensitivity analysis to identify the important control points in the pyruvate recycling pathways. The analysis reveals that the V_{max} values of dicarboxylate carrier (DIC), pyruvate carboxylase (PC), pyruvate dehydrogenase (PDH), cytosolic malic enzyme cytosolic (MEc), pyruvate transporter (PYC) and citrate synthase (CSm) are important control points in the pathway.

Chapter 2

Biology of Pyruvate Recycling Pathways

Chapter Outline In this chapter we describe the basic physiology associated with pancreatic β-cells and experiments related to β-cells metabolism. We first summarize the basic physiology of pancreatic β-cells. Next, we report the findings which lead to the conclusion that insulin is released into the blood stream in a bi-phasic manner, by the triggering and amplifying pathways. Then, we illustrate the ^{13}C-isotopomer-based flux-quantification analysis that established the correlation between glucose stimulated insulin secretion (GSIS) and pyruvate recycling flux. Finally, we will summarize the series of gene knock-down experiments of enzymes associated with pyruvate recycling. Finally, we discuss plausible metabolic coupling factors.

2.1 Introduction to β-Cell Physiology

Pancreatic β-cells Pancreatic β-cells are found in the Islet of Langerhans. Pancreatic β-cells constitutes 75-85% of the Islet of Langerhans. Pancreatic β-cells are the place where insulin is expressed and released into blood stream. The signaling mechanism of insulin release into the blood stream is a well regulated and controlled mechanism which is influenced by many factors. In recent years research has indicated that fuel intermediates stimulate insulin secretion primarily by co-ordination of their metabolism in the mitochondria and cytoplasm of β-cells [76, 82, 66].

Mitochondria Most eukaryotic cells contain many mitochondria, which occupy up to 25 percent of the volume of the cytoplasm. Mitochondria are among the largest organelles, generally exceeded in size only by the nucleus, (and by the plant organelles – vacuoles, and chloroplasts). Mitochondria contain two very different membranes, an outer one and an inner one, separated by the inter-membrane space (Figure 2.1). The outer membrane, composed of about half lipid and half protein, contains proteins that render the membrane permeable to molecules having molecular weights as high as 10,000 a.m.u. The inner membrane, which is much less permeable, is about 20 percent lipid and 80 percent protein. The surface area of the inner membrane is greatly increased by a large number of infoldings, or cristae, that protrude into the matrix, or central space. In eukaryotic cells, the mitochondrion is the place where ATP is generated through the degradation of glucose and fatty acids. Aerobic metabolism of glucose and fatty acids generates ATP and other intermediates that are exchanged with the cytoplasm for various bio-synthetic and secre-

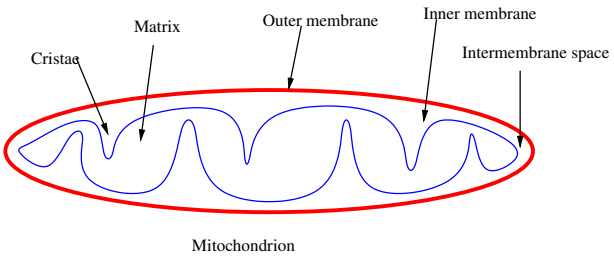

Figure 2.1: Schematic diagram of mitochondria.

tory processes. In the pancreatic β-cell, glucose and its intermediates are channeled to the mitochondria, where signals for the initiation and potentiation of insulin secretion are generated [88, 51]. Normal mitochondrial activity appears to be equally important in the action of insulin on its target tissues [66]. Insulin resistance in the elderly and in relatives of type 2 diabetic patients have also been associated with mitochondrial dysfunction [111].

Insulin Insulin is a peptide hormone and is expressed in pancreatic β-cells (Figure 2.2). The synthesis of insulin begins at the translation of the insulin gene, which resides on chromosome 11. During translation, two introns are spliced out of the mRNA product, which encodes a protein of 110 amino acids in length. This primary translation product is called proinsulin and is inactive. It contains a signal peptide of 24 amino acids in length, which is required for the peptide to cross the cell membrane. After a series of modifications in the endoplasmic reticulum and Golgi apparatus it becomes active insulin.

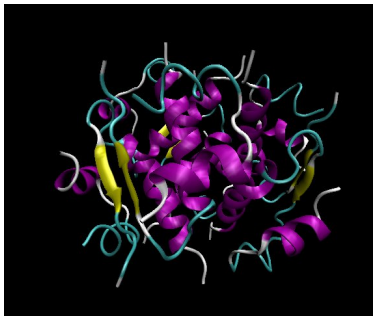

Figure 2.2: Structure of insulin. Figure from `www.rcsb.org`. PDB.ID 1AI0. Figure generated using Jmol `http://jmol.sourceforge.net/`

Exocytosis (the process through which cells release

molecules into the outside environment) of the insulin granules (insulin is stored in β-cells in the form of small clusters, called granules) is triggered by the entry of glucose into the β-cells. The rise in blood glucose following a meal is detected by the pancreatic β-cells, which respond by releasing insulin. The secretion of insulin has a broad impact on metabolism. The effects of insulin are reflected in an increase in gene transcription, and enzyme synthesis during its activity period.

Type 2 Diabetes Diabetes mellitus is the physiological state in which glucose homeostasis in the blood stream malfunctions. In the healthy condition, when the amount of glucose increases in the blood (e.g after a meal), the hormone insulin is released from the pancreas into the blood stream. This initiates a sequence of cellular events: insulin activates muscle and fat cells to remove glucose from the blood, and activates the liver to metabolize glucose, thus regulating glucose homeostasis in the blood.

In diabetic patients, the blood glucose level remains high, due to the failure of glucose homeostasis. One reason for this malfunction is the mis-regulation of insulin secretion into the blood stream. Moreover, there are multiple reasons why insulin might not carry out its action: insulin might not be properly produced in the β-cells, or may not be properly secreted into the blood stream. This situation leads to different types of diabetes classified according to the type of failure. The two most predominant types of diabetes are type 1 diabetes (5% of cases), which is an autoimmune disorder, and type 2 diabetes (95% of cases), which is associated with the failure of the insulin signaling mechanism (and is linked to obesity). Type 1 diabetes mainly affects children. In contrast, type 2 diabetes mostly affects adults. There is a high correlation between the life style of a person (e.g. obesity)

and type 2 diabetes. Other forms of diabetes are uncommon, such as gestational diabetes that occurs during pregnancy, or diabetes caused by a single gene mutation.

There are several factors underlying the malfunction of glucose homeostasis in type 2 diabetes. Two important factors are the body's resistance to insulin (i.e. the failure of cells to respond properly to insulin) and deficient production of insulin by the β-cells. In type 2 diabetes, one can suffer from a combination of deficient secretion and deficient action of insulin. The deficient secretion of insulin might be due to a failure of the glucose stimulated insulin secretion (GSIS) pathway in β-cells.

2.2 Glucose Stimulated Insulin Secretion

Insulin resistance can manifest out of many factors in type 2 diabetes. Studies done in animal models and humans suggest that the initializing factor is β-cell failure, which involves a reduction in β-cell mass and malfunctioning of important β-cell functions such as glucose stimulated insulin secretion (GSIS). β-cells ensure regulation of insulin by responding to multiple factors, including metabolites (glucose and other nutrients), neural signals, hormones, and sometimes pharmacological agents. The study of stimulated insulin secretion led to three important discoveries. First, glucose must be metabolized by β-cells to induce insulin secretion. The supporting evidence for this conclusion was found when glucose metabolism was interfered with in the cells. This led to failure of insulin release, which was restored only by the addition of external metabolized sugars [13, 29]. Second, Ca^{2+} is a significant regulator of insulin secretion. This was established by the fact that in the absence of Ca^{2+}, glucose failed to initiate insulin secretion [28, 72]. Third, β-cells

can be excited electrically [16].

In the present work we focus on the glucose-initiated signal, which is bi-phasic. That is, insulin released in two phases [26, 115]. The first phase is triggered by the so-called triggering pathway and the second, more sustained, phase is initiated by the so-called amplifying pathway. Next, we review the bi-phasic release of insulin secretion in response to increases in glucose concentration.

Before we start our discussion on bi-phasic release of insulin initiated by glucose metabolism, we emphasize that there are many other potentiators of insulin secretion which do not involve glucose mediation (Figure 2.3). Significant among non-glucose potentiators are incretin hormones glucagon-like peptide-1 (GLP1) and gastrointestinal inhibitory polypeptide (GIP), which are released by the enteroendocrine cells of the small and large intestine (L cells) during the process of food digestion [3]. These hormones trigger the activity of adenylate cyclase and cyclic AMP in the β-cell. It is significant to note that GLP1 modulates the activity of the three ion channels in the β-cell: the K_{ATP} channels, the voltage gated Ca^{2+} channels and voltage dependent K^+ (K_v channels). K_v also plays an important role in the triggering pathway of GSIS. Finally, there is evidence in support of the amino acids arginine and leucine as insulin potentiators. Arginine modulates the K^+ channels whereas leucine is known to be an allosteric modifier of important enzymes (like glutamate dehydrogenase) which may have a role in generating potentiators [20, 105]. A schematic figure of this complex insulin signaling network is provided in Figure 2.3.

The Triggering Pathway Glucose metabolism in β-cells contributes to the tight regulation of the Ca^{2+} concentration and voltage-operated Ca^{2+} channels, which have subsequent

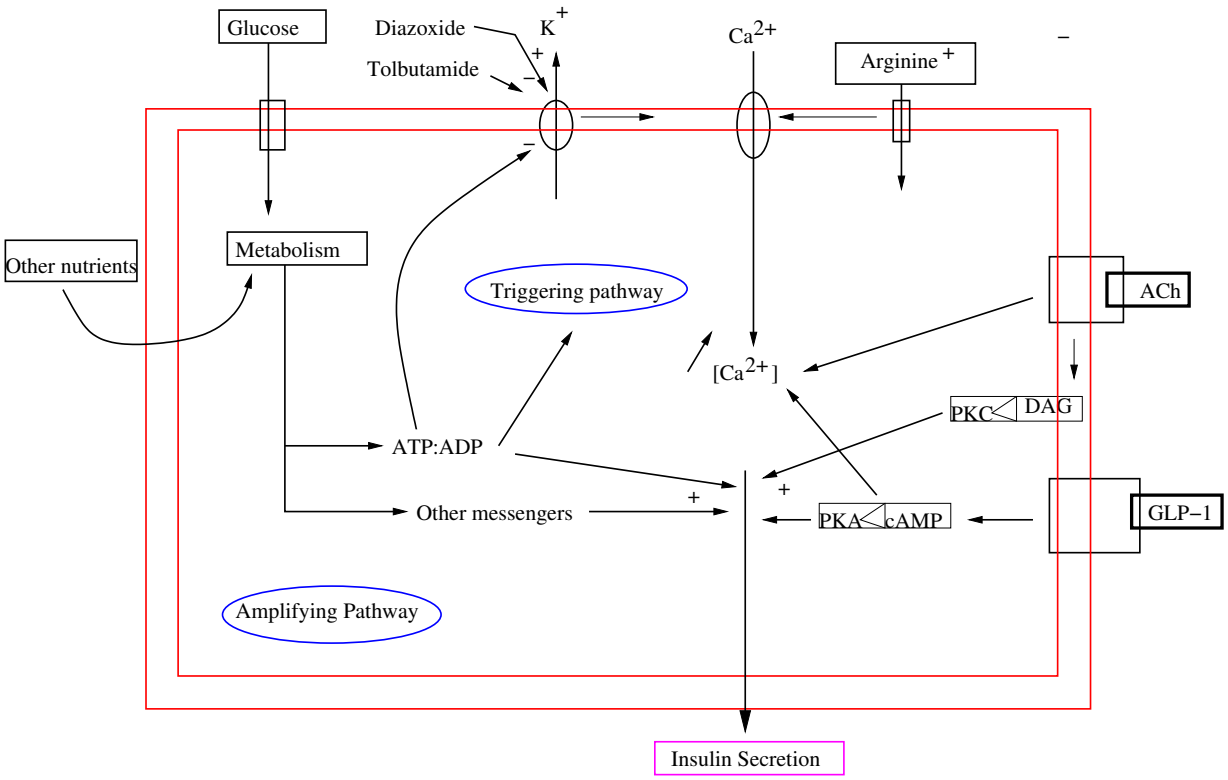

Figure 2.3: Schematic of insulin secretion phases and potentiators.

roles in insulin signaling (Figure 2.4).

As the glucose concentration rises, β-cell metabolism increases, generating more ATP. Consequently, ATP-sensitive K^+ channels (K_{ATP} channels) close, which results in the modulation of the K^+ conductance. This results in membrane depolarization (charge reversal across the plasma membrane). One of the primary physiological regulators of these channels which is derived from glucose is the ATP:ADP ratio, however there may be other regulators. Once a threshold value of membrane depolarization is reached, voltage-operated Ca^{2+} channels are activated. These channels open, allowing an influx of Ca^{2+} into the β-cell (down the electrical gradient). This opening of Ca^{2+} channels occurs at regular

intervals, which oscillate together with membrane potential. This results in oscillation of Ca^{2+}, which in turn triggers insulin secretion.

The significant role of K_{ATP} channels is demonstrated through agents that open or close channels without interfering with glucose metabolism. It has been shown that when mouse islets are stimulated with 15 mmol/g glucose, β-cells display typical electrical activity: Ca^{2+} oscillates and insulin secretion is stimulated. However, the opening of K^+ channels with diazoxide causes membrane re-polarization, which results in lowering of Ca^{2+} and subsequent inhibition of insulin secretion. Moreover, addition of tolbutamide, which closes the channels, restores the depolarization and resumption of electrical activity. This results in rise of Ca^{2+} and increase in insulin secretion [36].

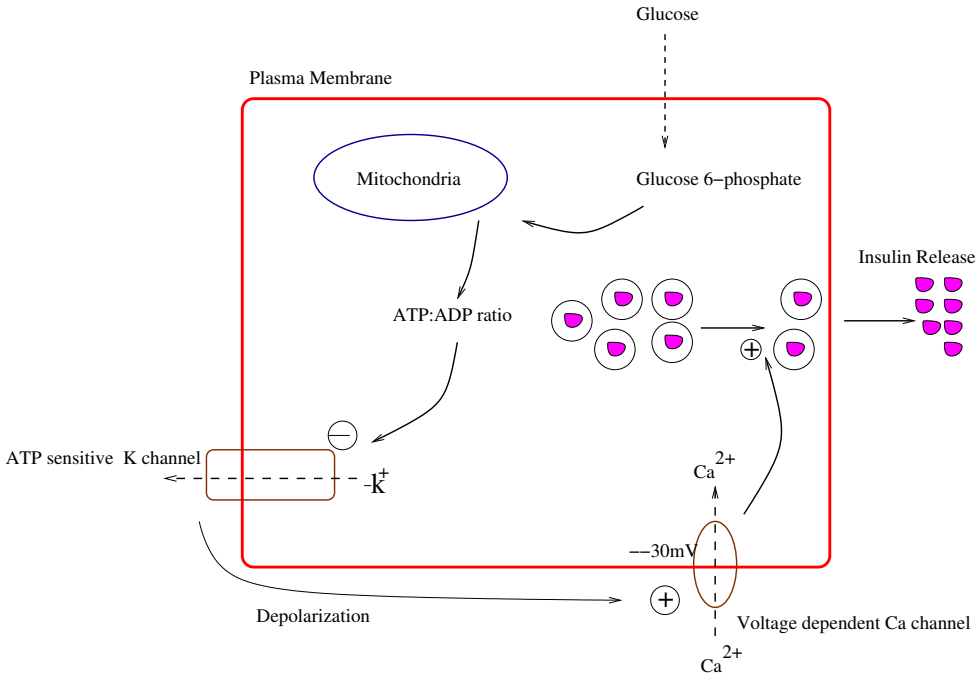

Figure 2.4: Schematic illustration of glucose initiated triggering pathway of insulin secretion.

In summary the GSIS mediated trigger signal follows the following steps:

- Glucose enters the β-cells through facilitated diffusion.
- Glucose is metabolized through oxidative metabolism which increases the ATP:ADP ratio. The increase in this ratio initiates the closure of K^+ channels.
- Voltage operated Ca^{2+} channels are opened.
- Ca^{2+} influx increases.
- As a result plasma membrane depolarization happens and there is subsequent activation of the exocytotic mechanisms.

The Amplifying Pathway Evidence for a second phase of insulin secretion emerged in two independent experiments by Gembal *et al.* and Sato *et al.* [26, 94]. This second phase of activity is initiated by the so-called amplifying pathway.

Glucose stimulated insulin secretion occurs by membrane depolarization mediated by K_{ATP} channels. The activity of K_{ATP} channels can be modulated by diazoxide, which opens the channel without interfering with the insulin secretion process. By adding extra K^+, membrane depolarization can be initiated, which subsequently initiates the insulin secretion. However, when the function of K_{ATP} channels was removed through diazoxide, glucose was still able to increase insulin secretion where the cells depolarized by KCl [26, 94]. Moreover, experiments were carried out using sulfonylureas, which closes the K_{ATP} channels instead of opening. When the activity of K_{ATP} channels is inhibited by sulfonylureas, glucose was still able to increase insulin secretion. Both these results suggest that there

is a mechanism through which glucose potentiates insulin secretion that is independent of K_{ATP} channel regulation. This pathway is termed the *amplifying pathway*. Subsequently, K^+-induced depolarization in the presence of diazoxide was used to show that glucose can increase insulin secretion independently of K_{ATP} channels in rodent islets [55, 25, 48, 10, 70], human islets [107], perfused rat pancreas [1], and insulin secreting cell lines [41].

Hierarchy between the triggering and amplifying pathways Its has been shown that the two pathways trigger insulin secretion in a fixed order: the amplifying pathway follows the triggering pathway. The manipulation of K_{ATP} channels by diazoxide at low concentration of glucose showed that the amplifying pathway tends to amplify the trigger signal [37].

The glucose-derived second messenger that signals the amplifying pathway has not been conclusively identified; it is the subject of current studies. In the subsequent discussion we summarize recent evidence that has emerged about the second messenger.

2.3 NMR Experiments

In this subsection we summarize the rat INS-1 derived cell lines that are used to study the metabolic pathways of β-cells. Then we describe the ^{13}C-isotopomer analysis of these cell lines that showed that pyruvate recycling through the enzyme pyruvate carboxylase enzyme (and not through pyruvate dehydrogenase) is correlated with GSIS.

INS-1 derived cell lines In order to gain better understanding of the biochemical regulation involved in insulin secretion, Hohmeier *et al.* [41] derived robust ATP-sensitive K^+ channel-dependent and independent cell lines from rat INS-1 cell lines, as follows. First, rat INS-1 cell lines were transfected by plasmids containing the human proinsulin gene. Subsequently, three kinds of cell lines were developed based on the glucose-derived insulin-secretion response: responsive cell lines, moderately responsive cell lines, and less responsive cell lines. The analysis of strongly responsive cell lines was carried out. These cell lines showed stable glucose response for longer period of time (approximately 7.5 months) and successful secretion of insulin in response to potentiators like isobutyl-methylxanthine, and oleate/palmitate. Studies of the K_{ATP} channels were carried out using the pharmacological agents diazoxide, to inhibit the insulin secretion, and sulfonylurea, to potentiated glucose-induced insulin secretion. These validating the cell lines against the prevailing hypothesis about the role of the K_{ATP} channels. Next, comparison between the poorly responsive cell lines and the responsive cell lines revealed that the responsive cell lines were able to increase the insulin secretion in the K_{ATP} channel independent manner whereas for poorly responsive cell lines the insulin secretion was almost identical for both dependent and independent cases. This validated the presence of the amplifying pathway.

^{13}C-NMR analysis of INS-1 derived cell lines Lu *et al.* [63] used ^{13}C-NMR istopomer analysis of glutamate to show that pyruvate recycling is correlated with the GSIS. The study was carried out in four clonal cell lines: two highly glucose-responsive cell lines (numbered 832/13 and 834/40), and two less glucose-responsive cell lines (832/1 and 832/4). The response characteristics of these cell lines is robust for long periods of tissue culture

which allowed effective ^{13}C istopomer analysis. Here we summarize the important aspect of the ^{13}C isotopomer model. In all the subsequent discussion the following definition of the pyruvate recycling ratio will be used:

$$\text{Pyruvate Recycling Ratio} = \frac{\text{Pyruvate Carboxylase Flux}}{\text{TCA cycle flux}}$$

The ^{13}C istopomer analysis starts by incubating cell lines in the [U-$^{13}C_6$]glucose, isolation of glutamate and finally analysis of ^{13}C istopomer using ^{13}C-NMR spectroscopy. The spectra was generated for two different models (Figure 2.5): pyruvate dehydrogenase (PDH) catalyzed conversion of [U-$^{13}C_3$]pyruvate to [U-$^{13}C_2$]acetyl-CoA and pyruvate carboxylase catalyzed (PC) conversion of [U-$^{13}C_3$]pyruvate to [1,2,3-$^{13}C_3$]oxaloacetae (conversion of pyruvate to [U-$^{13}C_3$]lactate via lactate dehydrogenase (LDH) is common for both the models). For these two models the glutamate carbon spectra (C2, C4 carbon positions) will show distinct peaks. If [U-$^{13}C_3$]pyruvate is converted only to [U-$^{13}C_2$]acetyl-CoA then the peaks in the spectra of glutamate will show uniformity. However, for the second model there will be different levels of peaks in the (C2, C4 carbon positions) NMR spectra.

The NMR spectra revealed larger peaks in the C4 component glutamate in the responsive cell lines compared to the less responsive cell lines. This is possible only if pyruvate is derived from TCA cycle intermediates. Significantly, acetyl-CoA showed a similar trend of percentage increase in concentration in all the four cell lines as the glucose concentration was raised (approximately ≈40, ≈70, and ≈85% at 3, 6, and 12 mM glucose level). Therefore, it can be concluded that PDH-catalyzed conversion of pyruvate to acetyl-CoA is not significant for the glucose-responsiveness of cell lines. Next, the pyruvate recycling

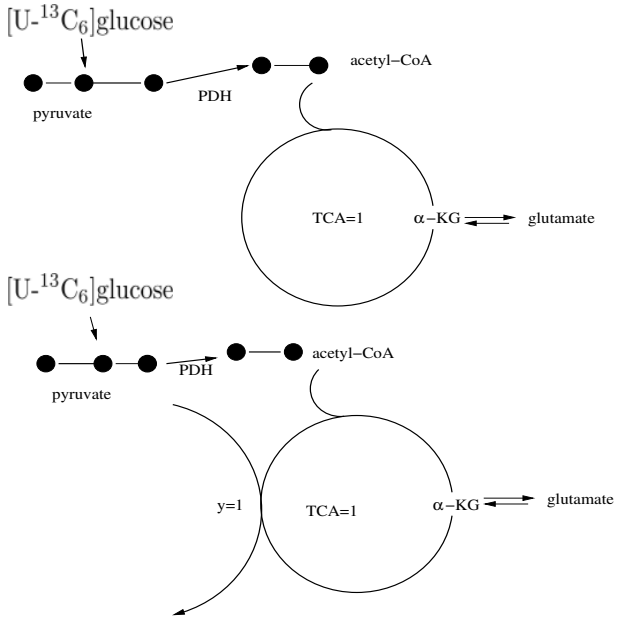

Figure 2.5: Schematic illustration of two models of ^{13}C istopomer analysis of pyruvate recycling rate.

ratio was measured in the two glucose-responsive cell lines and two unresponsive cell lines. The results were consistent with the hypothesis that the ratio was increased significantly in the two responsive cell lines when glucose concentration was increased from 3 to 12 mM concentration. In contrast, less responsive lines did not show any significant rise in the pyruvate recycling ratio when the glucose concentration was increased. The dose response curve of the pyruvate recycling ratio showed a linear relationship with insulin release. This further confirmed the involvement of pyruvate recycling in insulin secretion.

Finally, the activation and inhibition of pyruvate recycling were studied. Glucose-responsive cell lines were treated with DMM, which is an analogue of malate and so is expected to increase the conversion of TCA intermediates to pyruvate. The isotopomer analysis revealed that DMM increased pyruvate recycling by 40%. Further, insulin secretion

nearly doubled at 12mM glucose. This established a further correlation between pyruvate recycling and insulin secretion. Next, these cell lines were treated with PAA, which is an inhibitor of PC. The result was inhibition of insulin secretion at 12mM glucose, confirming that PC is important for GSIS.

Having confirmed that pyruvate recycling is linked to insulin secretion, studies turned to the identification of important target points in the pyruvate recycling pathway and possible metabolic coupling factors (MCF).

2.4 siRNA Gene Knock Down

Recent studies related to β-cell metabolism have focused on identifying control points and MCFs in the recycling pathway using short interfering RNA (siRNA) mediated gene silencing technique. siRNA is a double stranded RNA molecule approximately 20-25 base pairs in length. One of the important roles of siRNA is in RNA interference (RNAi). RNAi is a process of targeted gene silencing at the mRNA level.

The gene silencing mechanism is initiated by the RNAse enzyme called Dicer, which breaks down double stranded RNA (dsRNA) into siRNA. In the next step, these siRNAs are incorporated into a silencing complex called the RNA-induced silencing complex (RISC). RISC functions to identify complementary messenger RNA (mRNA) and subsequently inhibit its expression. The process is illustrated in the Figure 2.6.

siRNAs are easily available and have very high efficiency of delivery inside cells, which makes them ideal for gene knock-down studies.

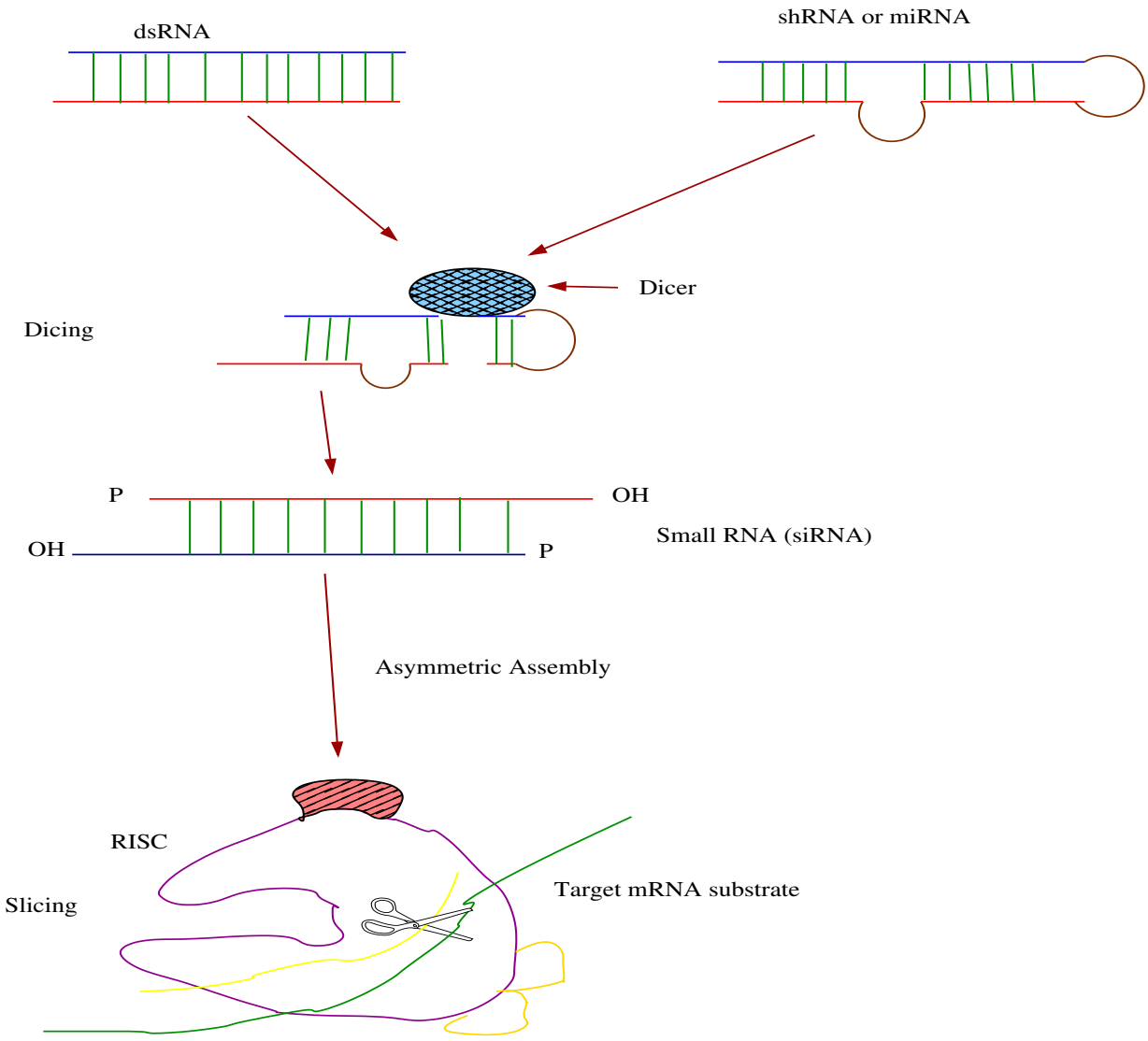

Figure 2.6: Schematic illustration of siRNA mediated gene silencing. In the first step the RNase-III-like enzyme Dicer processes the long dsRNA and miRNA into siRNA/miRNA duplexes. Next, these siRNAs are assembled into a complex called RISC, which carries out RNA cleavage (and possibly other modifications).

2.5 Gene Knockdown of Pyruvate Recycling Pathways

The ^{13}C-NMR based isotopomer analysis revealed the role of pyruvate carboxylase (PC) in pyruvate recycling and established correlation between pyruvate recycling and GSIS. However, these studies do not identify the specific control points in the pathway that contribute to insulin release. To gain this understanding, a series of studies were done using siRNA-mediated gene silencing of enzymes involved in pyruvate recycle. In this section we describe the important insights developed through these knock-down experiments.

A note on the terminology about experiments: all the comparisons considered below are drawn between two cell lines: control cell lines and knock-down cell lines. The control cell lines are transfected with random siRNA and thus there is no genetic manipulation in these cell lines. Therefore these cell lines can be considered as the wild-type case. The experimental cell lines involve transfection with complementary siRNA to silence the corresponding gene; this is the knock-down case.

Isocitrate Dehydrogenase (ICDc) Ronnebaum *et al.* [88] studied the role of ICDc in GSIS using siRNA gene silencing experiments in glucose responsive rat insulinoma (INS-1-derived) cell lines and in primary rat islets. There are three isoforms of ICD which are expressed in pancreatic β cells. First, is the TCA cycle (mitochondrial) β-cells NAD-dependent ICD (EC 1.1.1.41). The other two enzymes are NADP dependent (EC 1.1.1.42) (ICDc). These NADP-dependent enzymes are expressed predominantly in the cytosol

where they participate in pyruvate recycling. The reaction catalysed by ICDc is :

$$\text{ICIT (cytosolic)} + \text{NADP} \rightleftharpoons \alpha\text{-KG (cytosolic)} + \text{NADPH}$$

The injection of complementary siRNA targeting ICDc in the cell lines led to a 39±% decrease in ICDc activity, whereas the mitochondrial isoform was unaffected. To study the ICDc-silencing effect on non-fuel mediated insulin release, cells where stimulated with a membrane depolarizing concentration of K^+. The stimulation resulted in approximately 3-fold increase in insulin secretion (at 2.8mM glucose) in both control cell lines and ICDc-silenced cell lines. This result indicates that ICDc suppression does not affect the fuel-independent release of insulin. However, the knock-down of ICDc caused inhibition in GSIS and reduced glucose-induced pyruvate recycling.

After establishing the validity of silencing the enzyme, its effect on metabolism was studied. The authors showed that when the glucose concentration was increased, there is a corresponding increase in insulin secretion and the NADPH:NADP ratio, thereby establishing a correlation between GSIS and the NADPH:NADP ratio. Furthermore, ICDc suppression affected the NADPH concentration. The experiments showed that the NADPH:NADP ratio increases by approximately 3-fold when glucose is increased from 3mM to 12mM in control cell lines. Significantly this ratio did not show the same increase for the ICDc knock-down case. Next, a small decrease in total concentration NADPH was observed at high glucose compared to low glucose, both in the control and silenced cell lines, but overall less concentration was observed in the ICDc-silenced cell lines. This implies that

the ICDc knock-down affects NADPH at both low glucose and high glucose. Also, the glycolytic rate was unaffected by the ICDc knock-down, but measurement of the pyruvate recycling using ^{13}C-NMR isotopomer analysis revealed a decrease in the pyruvate recycling ratio. Finally, the effect of ICDc silencing on different TCA cycle intermediate was studied. The concentration of seven TCA cycle metabolite (pyruvate, citrate, α-KG, succinate, fumarate, malate, lactate) was measured. Comparisons between the control and silenced cell lines at 3mM and 12mM glucose were carried out. There was no significant variation in the levels of pyruvate, malate, citrate, succinate and fumarate in control and silenced cell lines. However, lactate levels were increased by 2.8 fold at 12mM glucose concentration in silenced cell lines compared to control cell lines, whereas α-KG was decreased. Also, citrate levels were elevated at 3mM glucose in silenced cell lines compared to the control case. Putting all the information together, these experiments suggest that ICDc has a significant role to play in GSIS.

citrate isocitrate carrier (CIC) Joseph *et al.* [51] studied the role of mitochondrial CIC in regulation of GSIS. CIC is a transport enzyme that reversibly transports mitochondrial citrate (or mitochondrial isocitrate) to the cytosol in exchange for cytosolic malate:

$$\text{CIT (cytosolic)} + \text{MAL (mitochondrial)} \rightleftharpoons \text{CIT (mitochondrial)} + \text{MAL (cytosolic)}$$

This study was carried out in the INS-1 derived 832/13 cells and primary rat islets. The inhibition of CIC was carried out by the substrate analogue 1,2,3-benzenetricarboxylate (BTC) and CIC-specific siRNA (Ad-siCIC). Inhibition by BTC in INS-1 derived 832/13

cells and primary rat islets resulted in significant reduction in the both phases (triggering and amplifying) of insulin secretion, thereby establishing the role of CIC in regulation of GSIS. Next, the effect of genetic manipulation using Ad-siCIC was studied. Transfection with Ad-siCIC resulted in 53±8% reduction in CIC protein level. The silencing of CIC did not affected the glycolytic rate nor the nutrient-independent release of insulin. The cytosolic citrate level was reduced by 54±2% in Ad- siCIC treated cells (in comparison to control cells). Also, the total cellular concentration of citrate in the knock-down case was reduced by 37±3%, while the mitochondrial citrate was unaffected (again, compared to the control case). Furthermore, silencing of CIC resulted in a significant decrease in NADPH:NADP ratio compared to control cell lines. CIC is an important participant in the pyruvate recycle pathway, as it is one of the co-transporters of isocitrate, which is a substrate of ICDc enzyme, which is know to have significant role in GSIS. The results confirmed that CIC has an important role to play in GSIS.

citrate lyase (CL) Joseph *et al.* [52] investigated the roles of citrate lyase enzyme (CL) and fatty acid synthase (FAS) in GSIS. Citrate lyase converts cytosolic citrate into cytosolic oxaloacetate with cytosolic acetyl-CoA as a by-product.

$$\text{CIT (cytosolic)}+\text{CoA (cytosolic)} \rightleftharpoons \text{OAA (cytosolic)}+\text{Acetyl-CoA (cytosolic)}$$

FAS catalyzes conversion of acetyl-CoA and malonyl-CoA into long-chain fatty acids with NADPH as one of the co-factors. This series of reaction steps is believed to be one of the potential generators of metabolic coupling factor (MCF) for GSIS. To investigate the

role of these two enzymes siRNA-mediated gene silencing was carried out in INS-1 derived 832/13 cells and primary rat islets.

First we describe the findings reached by silencing CL. Two complementary siRNA were built for CL silencing: Ad-siCL2 and Ad-siCL3. Treatment with Ad-siCL2 resulted in 92±6% reduction in mRNA of CL and resulted in 75±4% reduction in CL protein compared with a control cell lines. Neither of these silencing treatments affected GSIS compared to control cell lines. The CL silencing reduced the cytosolic oxaloacetae by 54±7% , inhibited the glucose incorporation into lipid by 43±4% and reduced malonyl-CoA by 83±4%. All these findings are expected outcomes of CL suppression.

Next, complementary siRNA for FAS Ad-siFAS was generated. The treatment of Ad-siFAS in the cell lines reduced the FAS mRNA by 81±2% . Furthermore glucose incorporation into lipid was reduced by 59±4% with respect to control cell lines. Interestingly this reduction did not affect GSIS. Similarly, treatment of cell lines by Ad-siCL3 and Ad-siFAS reduced the mRNA level of CL by 65±4% and FAS mRNA by 52±3% but did not affect GSIS. Putting the results together it can be concluded that CL and FAS are not required for GSIS.

Malic Enzyme Ronnebaum *et al.* [89] studied the effects of silencing the cytosolic NADP-dependent Malic enzyme (MEc) and the mitochondrial NADH-dependent malic enzyme (MEm), in INS-1 derived 832/13 cell lines and primary rat insulinoma cells. MEc catalyzes the conversion of cytosolic malate to cytosolic pyruvate with NADPH is one of the co-factors, whereas MEm catalyzes the same conversion for mitochondrial species but with

NADH as co-factor. Together these two enzymes are part of pyruvate-malate pathway.

$$\text{MAL (mitochondrial)} + \text{NAD (mitochondrial)} \rightleftharpoons \text{PYR (mitochondrial)} + \text{NADH (mitochondrial)}$$

$$\text{MAL (cytosolic)} + \text{NADP (cytosolic)} \rightleftharpoons \text{PYR (cytosolic)} + \text{NADPH (cytosolic)}$$

First the cells were treated with two siRNA complementary to MEm: Ad-siMEm1 and Ad-siMEm2. The treatment of cells with Ad-siMEm1 lead to reduction of mRNA by 46±5% while Ad-siME2 decreased the mRNA by 87±1%. The control cell lines showed 5.7±1% fold increase in the insulin release when glucose concentration was increased from 2.5mM (basal) to 12mM (stimulatory). However, the AdsiMEm1 and Ad-siMEm2 treated cells exhibited only 3.5±0.7% and 2.6±0.5% fold increases respectively: a significant reduction. This result may be confounded by the fact MEm suppression affects β-cells growth; significant GSIS in INS-1 cell lines requires confluent cell cultures. Furthermore, silencing of MEm in rat insulinoma cell lines had no effect on the GSIS.

Next the knock-down experiments of MEc was studied. The silencing of MEc in 832/13 cell lines lead to 76±7% decrease in MEc mRNA. In control cell lines the insulin release showed 6.1±1.2% fold increase from basal to stimulatory glucose concentration, while in silenced cell lines a 3.3±1% fold increase was observed: a significant decrease. Furthermore in rat insulinoma cell lines MEc silencing lead to 82±3% reduction in MEc mRNA, but did not affect insulin release. Suppression of MEc did not affect the cell growth in 832/13 cell lines nor did it affect the TCA cycle metabolite concentrations. However, silencing did affect the NADPH concentration. Furthermore, MEc silencing did not affect the pyruvate

recycling rate. These results show that the pyruvate-malate cycle might not be playing an important role in GSIS.

Pyruvate Carboxylase (PC) Jensen *et al.* [46] investigated the effect of silencing pyruvate carboxylase (PC) on GSIS. PC catalyzes the conversion of pyruvate to oxaloacetate.

$$\begin{aligned} &\text{PYR (mitochondrial)} + \text{ATP (mitochondrial)} + \text{CO}_2\text{ (mitochondrial)} \rightleftharpoons \\ &\qquad \text{OAA (mitochondrial)} + \text{ADP (mitochondrial)} + \text{Pi (mitochondrial)} \end{aligned}$$

This is an alternative pathway of pyruvate entry into the TCA cycle. The standard pathway involves pyruvate dehydrogenase catalyzing the conversion of pyruvate to acetyl-CoA. PC activity is very high in β-cells compared to other cells; in β-cells PC carries roughly half of the pyruvate flux. It has been shown that the PC-catalyzed reaction is correlated with GSIS, but the PDH-catalyzed reaction is not [63].

The siRNA gene silencing experiments were carried out in INS-1 derived 832/13 cell lines and primary rat islets. A complementary Ad-siPC siRNA was constructed to silence the PC gene. The treatment of the 832/13 cell by Ad-siPC led to an 83% reduction in mRNA and a 64% decrease in PC protein level. Similarly, transfection of primary rat islet led to 56% and 35% reduction in PC mRNA and protein level respectively. The Ad-siPC treatment of the 832/13 cell lines did not affect the glycolytic or glucose oxidation rates. Interestingly the Ad-siPC treatment did not affect the pyruvate levels either at basal (2.5mM) or stimulatory (12mM) glucose levels. However, there was an approximately 60%

increase in the lactate level at 12mM glucose concentration compared to control cell lines. ^{13}C-NMR istopomer analysis revealed that, in Ad-siPC cells, there was no effect on the pyruvate recycling ratio when glucose is raised from basal to stimulatory level. Since, the pyruvate level is unchanged due to Ad-siPC treatment there might be two possibilities: either the activity of the remaining PC enzyme is proportionally increased or PDH activity has gone up. It is known that acetyl-CoA is an allosteric activator of the PC enzyme. To analyze the allosteric effect of acetyl-CoA on PC acetyl carnitine level was measured using quantitative MS/MS technique. acetyl-carnitine is in equilibrium with acetyl-CoA. Interestingly the acetly-carnitine concentration went up in the Ad-siPC treated cell lines. This explains the mechanism through which PC specific activity might increase, since PDH generates acetyl-CoA, while PC does not.

Next the effect on different metabolites was studied in Ad-siPC cells with respect to control cell lines. The silencing of PC did not effect the NADPH:NADP ratio. Furthermore, PC silencing did not effect the glucose oxidation rate, but there was an approximately 36% decrease in the ATP level in Ad-siPC-treated cells. Finally, the effect on the TCA cycle intermediate was studied. Compared to control cell lines, only α-KG was decreased in the knock-down case, when glucose is raised from 2.5mM to 12m. Other TCA cycle intermediates (succinate, fumarate and malate) were unaffected. Therefore, it seems that β-cells are fairly robust to genetic perturbations in PC.

ARNT Pillai *et al.* [85] investigated the role of the transcription factor Aryl hydrocarbon nuclear receptor nuclear translocator (ARNT)/hypoxia-inducible factor(HIF)-1β. To carry out silencing of ARNT/HIF-1β in INS derived 832/13 cell lines, two complementary siRNA

were constructed: siARNT1 and siARNT2. The treatment of 832/13 with siARNT1 resulted in 78±4% reduction in ARNT/HIF-1β mRNA while siARNT2 resulted in 56±5% reduction of mRNA. To measure the effect on insulin release, the comparison between control cell lines (siControl) and cell lines treated with siARNT1 and siARNT2 was done at basal (2mM) and stimulatory (16.7mM) glucose concentration. siARNT1 treated lines showed a 60±10% reduction in insulin release at stimulatory glucose concentration with respect to siControl cells. Similarly, siARNT2 treatment resulted in 52±17% decrease. Glycolytic flux was unaffected at basal glucose level in siARNT1 transfected cells, but showed 31±6% reduction at stimulatory glucose level with respect to siControl. However, there was no significant change in glucose oxidation both at basal and stimulatory glucose concentration. The immediate consequence of this is that a glucose induced change in the ATP:ADP ratio does not occur.

Next, to further investigate the role of ARNT/HIF-1β in GSIS, metabolic profiling of the glycolytic, pentose phosphate, TCA cycle, free fatty acid, and amino acid pathways in both siControl and siARNT1 cell lines were carried out. Here we summarize the effect on glycolytic and TCA cycle pathways, since these pathways are subject of interest in current work. This comparative analysis revealed that glycolytic intermediates were significantly reduced in siARNT1 cell lines. Interestingly, glucose-6-phosphate level was not affected by the knock-down, indicating that the activity of glucokinase is unaffected in siARNT1 treated cells. This observation is consistent with the result that glycolytic flux is unaffected in siARNT1 treated cells. However, other glycolytic intermediates, dihydroxyacetone phosphate, 3-phosphoglycerate, pyruvate, and lactate are significantly reduced both at basal and stimulatory glucose concentration in siARNT1 treated cell lines. The TCA cycle in-

termediates also showed marked decrease in metabolites concentration in siARNT1 cells compared to siControl cells. At stimulatory glucose concentration there was significant reduction in α-ketoglutarate (90$\pm$5%), succinate (68$\pm$2%), fumarate (67$\pm$1%), and malate (65$\pm$2%). Citrate showed less marked reduction of 49$\pm$8%. These metabolites are known to be important participants in pyruvate recycling which is known to be correlated with the amplifying pathway.

To further investigate the effect of ARNT/HIF-1β silencing, gene profiling of several genes involved in diabetes, glucose metabolism and pyruvate recycling was carried out. Here we outline the effect on ARNT/HIF-1β silencing on the pyruvate recycling pathway. Pyruvate carboxylase and pyruvate dehydrogenase were significantly reduced in response to ARNT/HIF-1β silencing. Moreover, the transport proteins DIC and OGC were significantly reduced in siARNT1 treated cells. Other important enzymes involved in pyruvate recycling, MEc and ICDc, were profiled. Out of the two, only MEc expression was reduced in response to ARNT/HIF-1β silencing; ICDc was unaffected. All these components are proposed to be important participants in the amplifying pathway. Putting all the information together we can conclude that ARNT/HIF-1β plays an important role in GSIS.

2.6 Possible Metabolic Coupling Factors

Several metabolic coupling factors (MCFs) have been proposed as potential activators of the second phase of insulin release (the amplifying pathway). Recent studies suggest that NADPH is the most important signaling molecule. Here we review the evidence supporting this hypothesis.

As discussed in the previous section, ^{13}C-isotopmer analysis of INS-1 derived cell lines revealed that recycling of pyruvate across the mitochondrial membrane correlates well with glucose responsiveness. Two enzymes of the pyruvate recycle pathway, ICDc and MEc are producers of NADPH. Evidence emerged from the siRNA studies showing that the NADPH:NADP ratio correlates with insulin secretion [88]. Furthermore, PC activity in β-cells is high (approximately 40-50% of pyruvate enters the TCA cycle through PC), and PC converts pyruvate into oxaloacetae, which can be subsequently converted into malate through reactions catalyzed by malate dehydrogenase (MDH). Malate participates in a number of reactions involved in pyruvate recycle(Figure 2.7). Significant among them is the transport of malate to the cytosol, by the malate-P_i antiporter (DIC), where it can be converted to pyruvate via cytosolic malic enzyme with CO_2 and NADPH as by-products. Pyruvate can then be transported back into the mitochondria via a pyruvate-H^+ symporter (PYC) from which the cycle continues. Furthermore, NADPH reducing equivalents can also be exported from the mitochondria as citrate and isocitrate. Finally, NADPH participates with enzymes outside the pyruvate recycle pathway which are known to be insulin potentiators [82]. For example, nitric oxide synthase, which is known to directly participate in insulin secretion, uses NADPH [77].

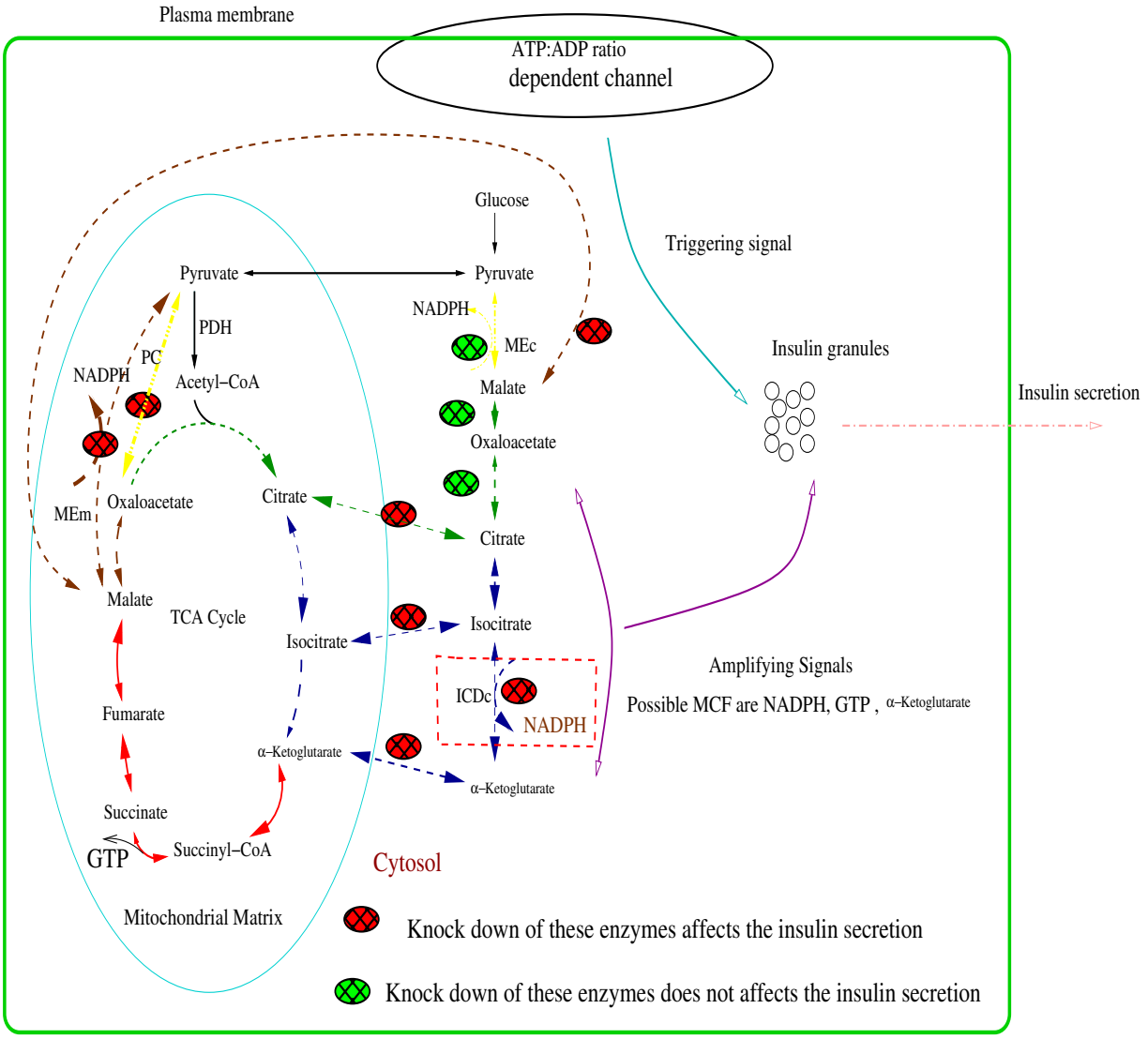

Figure 2.7: Schematic illustration of MCFs generated through the pyruvate recycling pathway. Red crossed ovals show enzymes whose silencing affects glucose stimulated insulin secretion (GSIS); green crossed ovals show enzymes whose silencing had not effect on GSIS. The red boxed region highlights the fact that knock-down of ICDc, which produces NADPH as co-factor, significantly affected GSIS.

Chapter 3

Kinetic Modeling and Model Analysis

Chapter Outline In this chapter we present a brief summary of the procedures used to build kinetic models. Firstly, we describe how to develop kinetic models from available information about metabolic pathways. Second, we introduce stoichiometric analysis, which is relevant for addressing basic properties of kinetic models (and can provide a useful consistency check). Finally, we conclude by presenting methods for local sensitivity analysis (LSA) and global sensitivity analysis (GSA) of kinetic models.

3.1 Development of Kinetic Models

Metabolism is a highly organized and regulated cellular process, involving thousands of enzyme-catalyzed reactions. A series of reactions in which one metabolite is transformed into another is known as a metabolic pathway; for modelers the dynamics of these pathways is of particular interest. Modeling allows the identification of control points in pathways,

and describes the dynamic behavior of pathway metabolites. The development of a kinetic model involves the identification of the metabolic pathway, the determination of the associated enzyme kinetics (including regulation), and the construction of a system of differential equations. These equations can be used to investigate properties of the system using methods such as local sensitivity analysis (LSA) or global sensitivity analysis (GSA).

Every modeling task starts with some assumptions. The first basic assumption we make in kinetic modeling is that each organelles is a different compartment, and each compartment is well mixed. Reaction rates can then be assumed to follow the law of mass action, according to which the "reaction rate is proportional to the probability of collision of reactants, which, in turn, is proportional to the concentration of reactants to the power of their molecularity". We then formulate rate equation as follows,

$$\frac{d[X]}{dt} = \text{Rate of production of } [X] - \text{Rate of consumption of } [X]$$

Here $[X]$ designates any compound involved in either a metabolic pathway or in transcription or translation processes.

Pathway Identification To construct a kinetic model, the first task is to identify the biochemical pathway which will be the subject of investigation. This task is facilitated by a series of well-curated databases, like KEGG [54], Reactome [68, 109], UniPathway [75] and many more. (A comprehensive list of biology-related databases is published every year in Nucleic Acid Research Database issue.) These databases provide detailed descriptions of the biochemical reactions in each pathway, through which we get the details of the

molecular mechanism (e.g., enzyme catalytic cycle). These details include

- The identity of all components of the metabolic pathway.
- The intracellular location and components of each reaction (e.g. all the possible states of the proteins involved).
- The kinetic mechanism of action of each reaction in the pathway.

Once the details of the metabolic network have been identified, the next task is to assign values to the kinetic parameters involved in the pathway reactions. There are curated databases that catalog the kinetic data of enzymes and biochemical reactions. Brenda [95, 98] and EMP database [102] are the two databases which have the most comprehensive enzymological data related to kinetic description of enzymes. SABIO-RK [112, 113] is database that catalogues information about biochemical reactions, their kinetic equations (with parameter values), and the experimental conditions under which these parameters were measured.

Once these details are collected the details of mechanism of action (i.e. rate expressions) of each reaction can be incorporated into the model. We next review the basics of enzyme kinetics, which provide a foundation for describing the rates of metabolic reactions.

3.1.1 Introduction to Enzyme Kinetics

Enzymes are the house-keepers of biological processes. The mechanisms through which they catalyze biochemical reactions demand special mathematical treatment. Enzyme catalysis

involves multiple stages of enzyme-substrate interaction; to formulate the mechanism enzyme catalysis we will make some simplifying assumptions. These assumption enable us to take into account the diversity of dynamic and regulatory properties of different enzymes. The main features of these approaches are described below [17, 14, 30].

In 1902 Adrian Brown [43] proposed that an enzyme-catalyzed reaction is composed of two elementary reactions in which substrate forms a complex with the enzyme, which subsequently decomposes into product and enzyme:

$$[E] + [S] \rightleftharpoons [ES] \rightarrow [P] + [E] \tag{3.1}$$

Here, $[E], [S], [ES], [P]$ symbolize the enzyme, substrate, enzyme substrate complex and products respectively. Let k_1 be the rate of the forward reaction and k_{-1} be the rate of the backward reaction for the first stage (that is, for the reaction $[E] + [S] \rightleftharpoons [ES]$). Let k_2 be the rate of the forward reaction for the second step of the reaction (that is, for reaction $[ES] \rightarrow [P] + [E]$). The time-course of the individual reactant concentrations are expressed by the differential equations,

$$\frac{d[S]}{dt} = -k_1[S][E] + k_{-1}[ES] \tag{3.2}$$

$$\frac{d[E]}{dt} = -k_1[S][E] + (k_-1 + k_2)[ES] \tag{3.3}$$

$$\frac{d[ES]}{dt} = k_1[E][S] - k_{-1}[ES] - k_2[ES] \tag{3.4}$$

$$v = \frac{d[P]}{dt} = k_2[ES], \tag{3.5}$$

where the last equation describes the rate equation for the product formation, also called

the reaction velocity v. This reaction rate is directly proportional to $[ES]$, the concentration of the enzyme substrate complex. In practice, we need to express the reaction rate v in terms of the concentration of $[S]$ because $[ES]$ is not known. We make two simplifying assumptions based on the characteristics of the system dynamics (Figure 3.1).

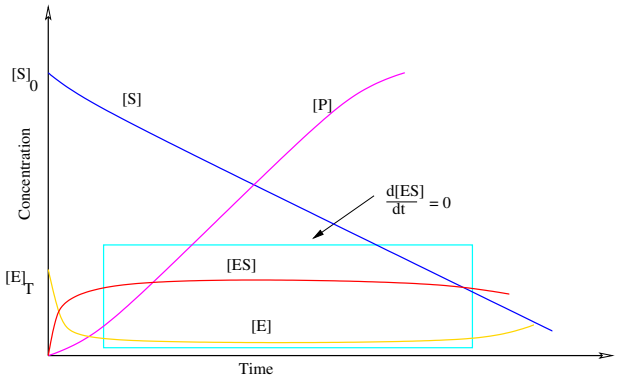

Figure 3.1: Time-course for the components of a simple Michaelis-Menten reaction. After the initial transient, the slopes of [ES] and [E] are essentially zero so long as $[S] \gg [E]_T$ [30] (as represented by the box).

To simplify this system, Lenor Michaelis and Maude Menten, building on the previous work of Victor Henri, proposed in 1913, the idea of using a rapid-equilibrium assumption. They assumed that if $k_1 \gg k_2$, then the first step of the reaction achieves equilibrium quickly, so that,

$$K_S = \frac{k_{-1}}{k_1} = \frac{[E][S]}{[ES]}. \tag{3.6}$$

Here K_S is dissociation constant.

In 1925 G. E. Briggs and J. B. S. Haldane [8] provided an alternative mechanism, called the quasi-steady state assumption, to solve the system. Referring to Figure 3.1 we observe

that for reasonable length of time concentration of $[ES]$ is nearly constant, since formation and consumption of the $[ES]$ complex keeps in balance. So we can assume that,

$$\frac{d[ES]}{dt} = 0 \tag{3.7}$$

Based on the above quasi-steady state assumption we present the derivation of reaction rate v as follows,

$$\text{Conservation equation} \quad [E]_T = [E] + [ES] \tag{3.8}$$

so that

$$[E] = [E]_T - [ES] \tag{3.9}$$

Combining steady state assumption of equation 3.7 and this conservation equation we

substitute for $[E]$ in 3.4. We then get,

$$k_1([E]_T - [ES])[S] = (k_{-1} + k_2)[ES] \tag{3.10}$$

Which on rearrangement becomes (3.11)

$$[ES](k_{-1} + k_2 + k_1[S]) = k_1[E]_T[S] \tag{3.12}$$

Dividing both sides by k_1 gives (3.13)

$$[ES](\frac{k_{-1} + k_2}{k_1} + [S]) = [E]_T[S] \tag{3.14}$$

Rearranging the terms, we have (3.15)

$$[ES] = \frac{[E]_T[S]}{K_M + [S]} \tag{3.16}$$

(3.17)

Here K_M is called the Michaelis constant, defined as

$$K_M = \frac{k_{-1} + k_2}{k_1} \tag{3.18}$$

(3.19)

Now, reaction rate (from equation 2.4), is

$$v = \left(\frac{d[P]}{dt}\right) = k_2[ES] = \frac{k_2[E]_T[S]}{K_M + [S]} \tag{3.20}$$

We now define the limiting rate (maximal velocity) of the reaction as follows. (3.21)

$$V_{max} = k_2[E]_T \tag{3.22}$$

Now the expression for reaction rate becomes

$$v = \frac{V_{max}[S]}{k_M + [S]} \tag{3.23}$$

Referring to Figure 3.2, the Michaelis constant K_m represents the concentration at which the reaction velocity is half maximal. Therefore enzymes with small K_m values will achieve maximum catalytic efficiency at low concentration of substrate. The limiting rate of the reaction, V_{max}, occurs at high substrate concentrations, when enzyme is saturated. The units of the Michaelis constant K_m are concentration; V_{max} has units of concentration per time.

Estimation of kinetic data To estimate the values of parameters V_{max} and K_m for an enzyme, one measures the initial rates for different initial substrate concentrations. Since the rate is non-linear, one has to determine the parameters by non-linear regression. Another approach is to transform to a linear relation between variables and then apply linear regression.

To illustrate the process consider the Lineweaver-Burk plot [62], as follows. The

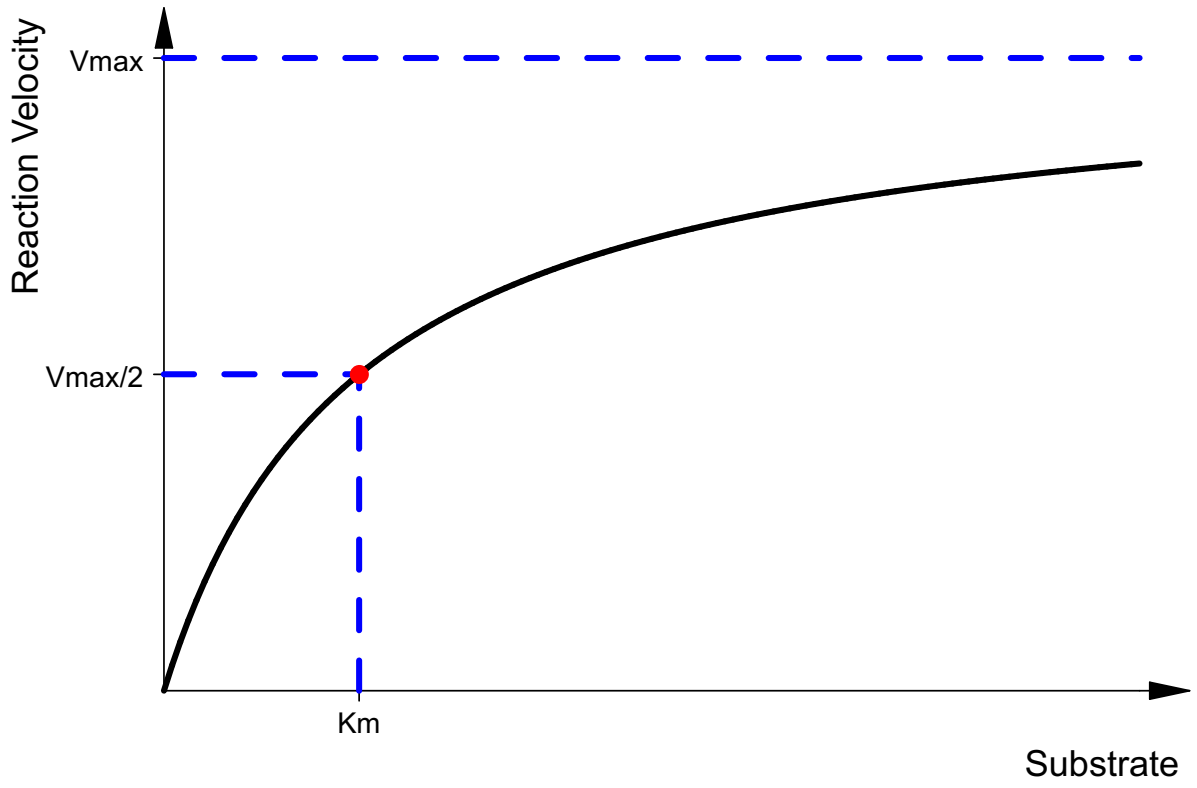

Figure 3.2: Illustrative plot of the turnover rate v_0 of Michaelis-Menten reaction versus the substrate concentration [S].

Michaelis-Menten equation can be rearranged as:

$$\frac{1}{v} = \left(\frac{K_M}{V_{max}}\right)\frac{1}{[S]} - \frac{1}{V_{max}} \tag{3.24}$$

Now, the equation is linear in terms of $\frac{1}{v}$ and $\frac{1}{[S]}$. When we plot $\frac{1}{[S]}$ vs $\frac{1}{v}$, the slope is given by $\frac{K_M}{V_{max}}$, the $\frac{1}{v}$ intercept is $\frac{1}{V_{max}}$, and the $\frac{1}{[S]}$ intercept is $-\frac{1}{K_M}$. A disadvantage with this plot is that most experiment occurs at high substrate concentration so the data tend to clutter in one region, which can cause a large error when fitting the line. Eadie and

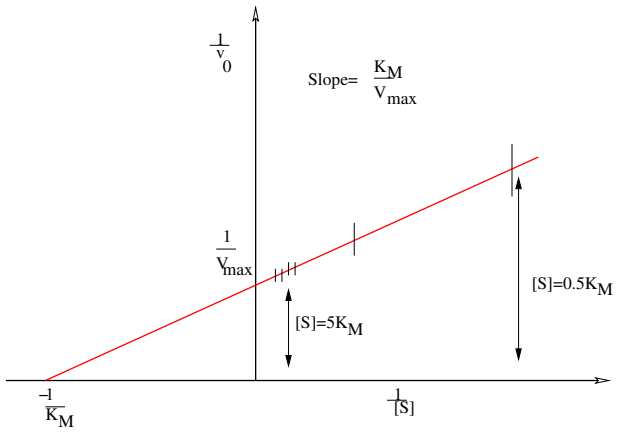

Figure 3.3: A Lineweaver-Burk plot. Note the crowding of points at large [S].

Hofstee [21] and Hanes and Woolf [31] have proposed alternative way of linearizing the rate expression, but they are also not free of limitations. More details can be found in the book by Cornish-Bowden [14]

Derivation of Fumarase Enzyme Kinetics The derivation in the previous section described the idealized case of an irreversible, one-substrate reaction. To illustrate a more complex catalytic mechanism, we next derive the rate expression of the fumarase enzyme. The reaction is assumed to be reversible, with one substrate (fumarate) and one product (malate). The reaction is competitively inhibited by citrate, ATP, ADP, GTP, and GDP. First we will derive the mechanism for single inhibition by ATP and then generalize the formula to include the rest of the inhibitors.

Let K_1 and K_{-1} be the forward and backward reaction for the enzyme (E) binding to fumarate (FUM).

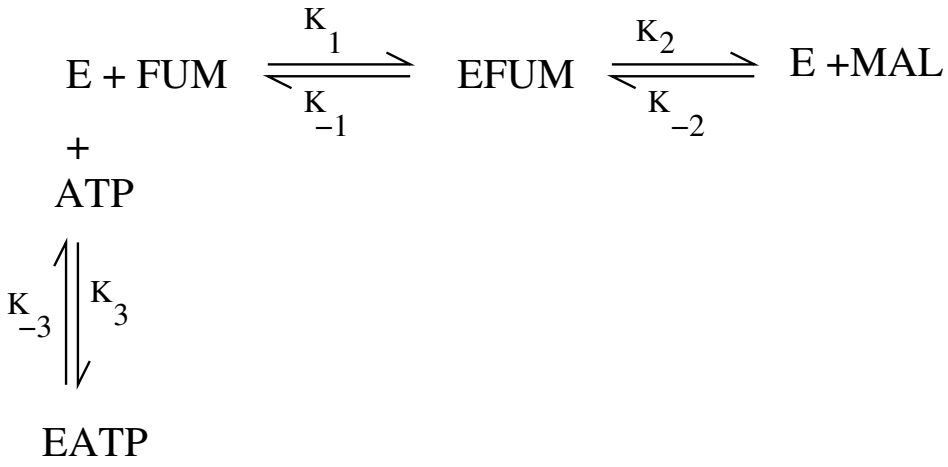

Figure 3.4: Fumarase Mechanism

Similarly let K_2 and K_{-2} be the rates for $EFUM$ dissociating to E and MAL and re-associating, and let K_3 and K_{-3} be the rates of formation/dissociation of the inhibited complex $E - ATP$.

The enzyme and enzyme-substrate concentrations are then described by

$$\frac{d[E]}{dt} = K_{-1}[EFUM] - K_{-2}[E][MAL] + K_{-3}[EATP] - K_1[E][FUM] - K_3[E][ATP]$$
$$\frac{d[EFUM]}{dt} = K_1[E][FUM] + K_{-2}[E][MAL] - K_2[EFUM] - K_{-1}[EFUM]$$

Applying a quasi-equilibrium assumption in the second equation gives the $[E]$ in terms of $[EFUM]$:

$$[E] = \frac{(K_{-1} + K_2)[EFUM]}{K_1[FUM] + K_{-2}[MAL]} \tag{3.25}$$

Using conservation, we have

$$[E] + [EATP] + [EFUM] = [E]_t \tag{3.26}$$

where $[E]_t$ is the total enzyme concentration, presumed fixed. The binding of inhibitor is also assumed to be in equilibrium. The dissociation constant for ATP is given by,

$$K_{iATP} = \frac{[E][ATP]}{[EATP]} = \frac{K_{-3}}{K_3} \tag{3.27}$$

This gives $[EATP]$ as

$$[EATP] = \frac{[E][ATP]}{K_{iATP}} \tag{3.28}$$

Substituting this equation back into the conservation equation we have,

$$[E](1 + \frac{[ATP]}{K_{iATP}}) + [EFUM] = [E]_t \tag{3.29}$$

Now combining the value of $[E]$ from the steady state assumption and the conservation equations, we get the value of $[EFUM]$ as

$$[EFUM] = \frac{[E]_t(K_1[FUM] + K_{-2}[MAL])}{(K_{-1} + K_2)\alpha + K_1[FUM] + K_{-2}[MAL]} \tag{3.30}$$

Let $\alpha = 1 + \frac{[ATP]}{K_{iATP}}$

The reaction rate v is given as

$$v = -\frac{d[FUM]}{dt} = K_1[E][FUM] - K_{-1}[EFUM] \tag{3.31}$$

Substituting the value of $[E]$ and $[EFUM]$ and rearranging, we arrive at

$$v = \frac{[E]_t K_1 K_2 [FUM] - [E]_t K_{-1} K_2 [MAL]}{(K_{-1} + K_2)\alpha + K_1 [FUM] + K_{-2} [MAL]} \tag{3.32}$$

Now let $V_{mf} = K_2 [E]_t$ and $V_{mr} = K_{-1} [E]_t$.

Then,

$$v = \frac{K_1 V_{mf} [FUM] - V_{mr} K_{-2} [MAL]}{(K_{-1} + K_2)\alpha + K_1 [FUM] + K_{-2} [MAL]} \tag{3.33}$$

Now define $K_{mFUM} = \frac{K_{-1}+K_2}{K_1}$ and $K_{mMAL} = \frac{K_{-1}+K_2}{K_{-2}}$.

Multiplying and dividing by $K_{-1} + K_2$ we get

$$v = \frac{\frac{V_{mf}[FUM]}{K_{mFUM}} - \frac{V_{mr}[MAL]}{K_{mMAL}}}{\alpha + \frac{[FUM]}{K_{mFUM}} + \frac{[MAL]}{K_{mMAL}}} \tag{3.34}$$

Discussion This equation 3.34 describes the turnover rate of fumarase. It can be observed that when $\alpha = 1$, equation 3.34 reduces to the case of un-inhibited reversible Michaelis-Menten kinetics. As α increases (Figure 3.6) it affects the K_M value, but does not affect the V_{max}. In other words, the larger the value of α, the greater the substrate concentration needed to approach V_{max}. If there are multiple inhibitors, then only α changes; the rest of the constants remains the same [14]. If we assume equilibrium binding for all

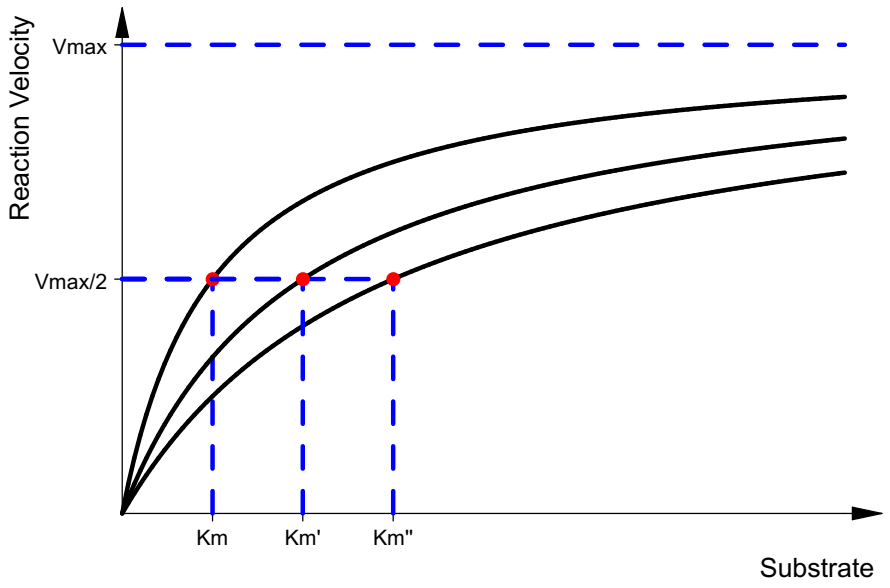

Figure 3.5: Illustration of effect of inhibition coefficient α on Km. $\alpha = 1$; Km, $\alpha = 2$; Km', $\alpha = 3$; Km''

inhibitors of fumarase, the dissociation constants are defined as,

$$K_{iADP} = \frac{[E][ADP]}{[EADP]}$$
$$K_{iGDP} = \frac{[E][GDP]}{[EGDP]}$$
$$K_{iGTP} = \frac{[E][GTP]}{[EGTP]}$$
$$K_{iCIT} = \frac{[E][CIT]}{[CIT]}$$

In this case α is given as:

$$\alpha = 1 + \frac{[ATP]}{K_{iATP}} + \frac{[ADP]}{K_{iADP}} + \frac{[GTP]}{K_{iGTP}} + \frac{[GDP]}{K_{iGDP}} + \frac{[CIT]}{K_{iCIT}} \tag{3.35}$$

3.1.2 Cooperativity

Many proteins, including enzymes, have multiple binding sites where a molecule, generically called a ligand, can bind; these binding processes may cause interactions between the binding sites themselves. Consider the simple case where one ligand molecule (S) binds to a protein (E) with one binding site:

$$[E] + [S] \rightleftharpoons [ES]$$

The binding constant K_B is defined as:

$$K_B = \frac{[ES]}{[E] \cdot [S]} \tag{3.36}$$

The dissociation constant K_D is defined as the reciprocal of K_B. The total number of binding sites that have bound ligands, divided by the total number of sites is called the fractional saturation, Y, given by:

$$Y = \frac{[ES]}{[E]_{total}} = \frac{[ES]}{[ES] + [E]} = \frac{K_B \cdot [S]}{K_B \cdot [S] + 1} \tag{3.37}$$

Given that $[E]_{total} = [ES] + [E]$ and using equation 3.36 $[E] = \frac{[ES]}{K_B \cdot [S]}$. The plot of Y vs S is hyperbola (Figure 3.6). Now, if the the protein has several binding sites, then interaction between these sites may occur: the affinity to further ligands may change after binding of one or more ligands. This phenomena is called *cooperativity*. Positive cooperativity increases the affinity of ligand to bind to the site whereas negative cooperativity decreases

the affinity of further ligands to bind on the sites.

Next we derive the expression for a dimeric protein with two identical binding sites exhibiting cooperativity. We start with the assumption that binding of the first ligand increases the binding of the second ligand:

$$[E_2] + [S] \xrightarrow{\text{slow}} [E_2][S] \tag{3.38}$$
$$[E_2][S] + [S] \xrightarrow{\text{fast}} [E_2][S]_2$$

where $[E]$ is a monomer and $[E_2]$ is dimer. The fractional saturation Y is defined as:

$$Y = \frac{[E_2][S] + 2[E_2][S_2]}{2[E_{2,total}]} = \frac{[E_2][S] + [E_2][S_2]}{2[E_2] + 2[E_2][S] + 2[E_2][S_2]} \tag{3.39}$$

Let us put further assumption that the affinity to the second ligand is strongly increased by binding to the first ligand, then $[E]_2[S]$ will react with $[S]$ as soon as it is formed, and the concentration of $[E_2][S]$ can be neglected. This assumption of complete cooperativity (i.e every protein is either empty or fully bound) leads to:

$$[E_2] + 2[S] \rightarrow [E_2][S_2] \tag{3.40}$$

Then binding constant is given by:

$$K_B = \frac{[E_2][S_2]}{[E_2] \cdot [S]^2} \tag{3.41}$$

and the fractional saturation Y is:

$$Y = \frac{2[E_2][S_2]}{2[E_{2,total}]} = \frac{[E_2][S_2]}{[E_2] + [E_2][S_2]} = \frac{K_B[S]^2}{1 + K_B[S]^2} \tag{3.42}$$

Under these assumptions, for a protein with n binding sites, one can derive an expression of the form

$$v = V_{max}Y = \frac{V_{max}K_B[S]^n}{1 + K_B[S]^n} \tag{3.43}$$

Where n is referred to as the Hill coefficient. This is referred to as a Hill function [38]. It implies that the binding to a certain ligand influences the affinity of the protein to further ligands. In the current study cooperativity can found in the TCA cycle enzymes

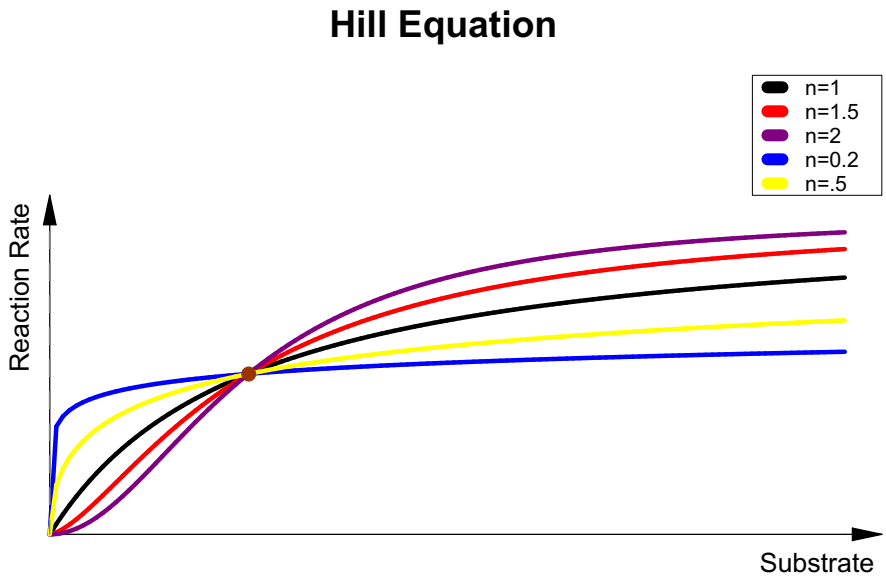

Figure 3.6: Plot of hill kinetics. $n < 0 < 1$ is cooperative inhibition; $n > 1$ is cooperative activation; $n = 1$ is Michaelis-Menten rate.

mitochondrial isocitrate dehydrogenase enzyme and succinyl-CoA dehydrogenase.

3.1.3 Allosteric Enzymes

Allosteric (Greek *allos*, other + *stereos* solid or space) enzymes are the class of enzyme which have extra binding sites other than the active (catalytic site). At these additional sites, small molecules such as metal ions can bind; this binding event has a regulatory effect on the catalytic activity of enzyme. The binding can induce the enzyme to catalyze more efficiently, or can have an inhibitory effect, where the catalytic efficiency of enzyme is reduced (Figure 3.7). Furthermore allosteric enzymes can incorporate cooperative regulation. Therefore, the kinetics of allosteric enzymes requires special treatment, since the complete mechanism cannot be explained just by Michaelis kinetics or the Hill equation.

Here we review the Monod *et al.* [73] model of allosteric regulation. We will not derive the expression but discuss the properties of the rate expression. The Monod model is based on the assumptions that:

- All the n enzyme sites are identical.
- Each sites belongs to a sub-unit. These sub-units have two conformational states: active (R) or inactive (T).
- All the sub-units change their conformations at the same time.
- The equilibrium constant between R and T conformations is called the allosteric constant and defined as follows:

$$L = \frac{T_0}{R_0} \tag{3.44}$$

  The index i for T_i and R_i denotes the number of bound substrate molecules.

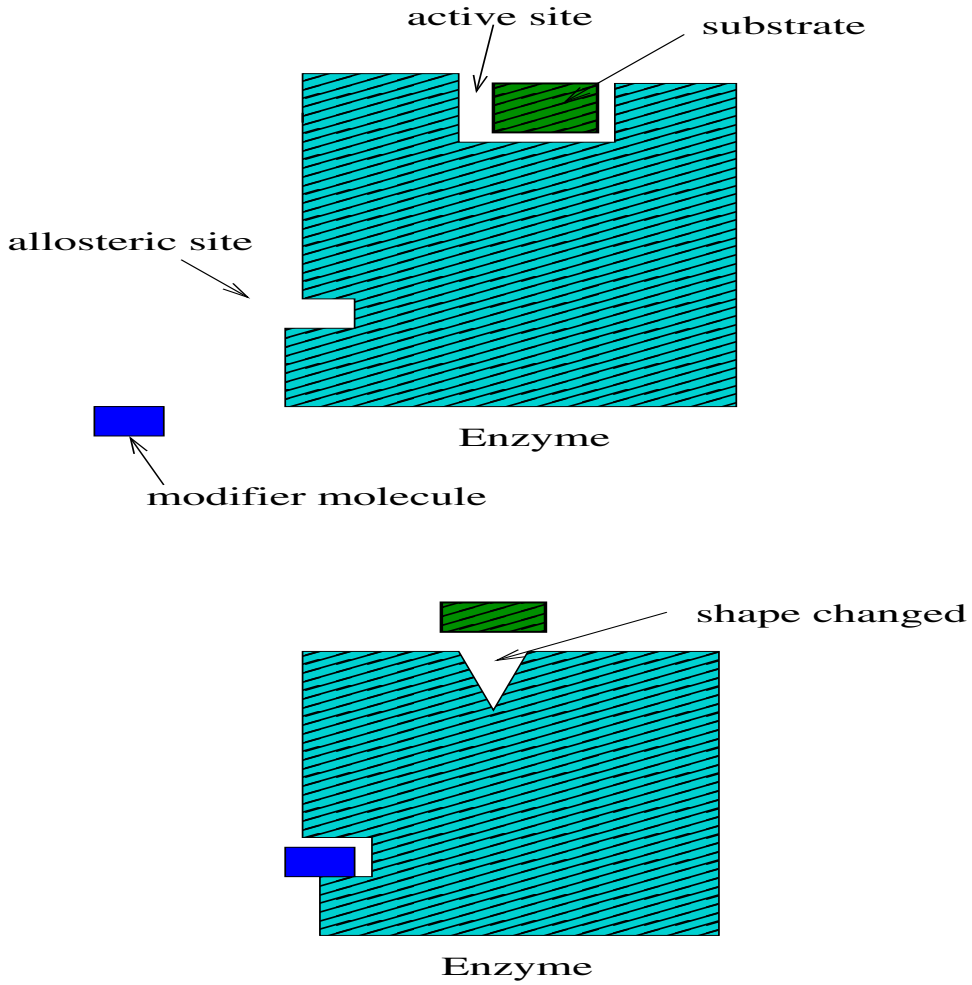

Figure 3.7: Schematic illustrate of allosteric enzymes and effect of allosteric modifier. Binding of the allosteric modifier to the allosteric site modifies the active site making the enzyme inactive. This is allosteric inhibition . Similarly, allosteric activation is possible.

Next, binding constants for the active conformations are given by K_R and for inactive conformation by K_T. Let us assume that substrate molecules can bind only to the active form, implying $K_T = 0$. The rate expression according to Monod *et al.* [73] is defined as:

$$V = \frac{V_{max} K_R[S]}{1 + K_R[S]} \frac{1}{1 + \frac{L}{(1+K_R[S])^n}} \tag{3.45}$$

where the factor $\frac{V_{max}K_R[S]}{1+K_R[S]}$ corresponds to the Michaelis-Menten kinetics, while $\frac{1}{1+\frac{L}{(1+K_R[S])^n}}$ is a allosteric regulatory factor.

For $L = 0$ the plot V vs S is a hyperbola as in Michaelis-Menten kinetics; For $L > 0$ one gets a sigmoid curve shifted to the right.

For the general case where substrate can also bind to the inactive state (that is $K_T \neq 0$) the rate expression is defined as follows:

$$V = \frac{V_{max}K_R[S]}{1+K_R[S]} \quad \frac{K_R + K_T L \left(\frac{1+K_T[S]}{1+K_R[S]}\right)^{n-1}}{1 + L\left(\frac{1+K_T[S]}{1+K_R[S]}\right)^{n}} \tag{3.46}$$

So far we discussed positive regulation involving cooperativity. Now we discuss allosteric activation and inhibition. For that we need to modify the L . Consider the case in which an activator $[A]$ binds only to the active conformation and an inhibitor $[I]$ binds only to the inactive conformation. This will shift the equilibrium to the respective conformation. So our modified allosteric constant is given by:

$$L' = \frac{(1 + K_I[I])^n}{(1 + K_A[A])^n} \tag{3.47}$$

K_I and K_A denote binding constants. An activator molecule decreases the sigmoidity while an inhibitor molecule increases the sigmoidity. The plot of the rate expression for different cases is shown in figure 3.8.

In the current study there are many allosteric enzymes, such as Pyruvate dehydrogenase and Succinyl-CoA dehydrogenase. However, the allosteric effects are primarily due

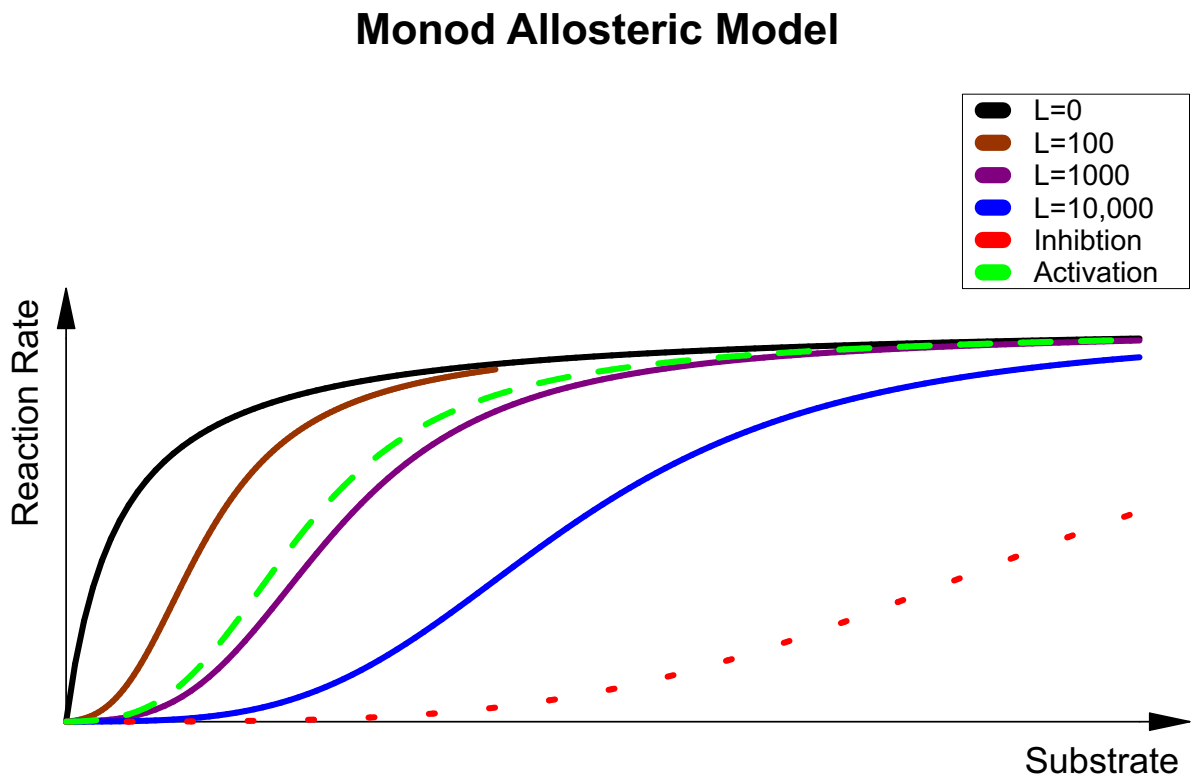

Figure 3.8: The plot of equation 3.45 for different values of L. Parameters are $V_{max} = 1, n = 4, K_R = 2, K_T = 0$. Values of L are shown in legend. We can observe that increasing the value of L causes strong sigmoidity. Also, shown are the effect of activators and inhibitors, with dashed and dotted line respectively. The value of $L = 10^4$ for this case and $K_I[I] = 1$ in equation 3.47 for inhibition and $K_A[A] = 1$ for activation.

to ions (Ca^{2+}) or the ATP:ADP ratio; when these species are treated as constants, the allosteric terms reduce to single parameters. In the model described in Chapter 5, allosteric regulation is only implicitly present in the model (as a parameter rather than a complete rate expression).

3.1.4 Transporters

Transporter proteins are a special class of membrane-embedded enzymes that selectively transport metabolites across the plasma membrane without any chemical modification to the molecule. Transporters are of two types: active and passive. Active transporters require energy to transport the molecule, while passive transporters require no energy expenditure. In the current study only passive transporters are involved. Passive transporters can be modeled in the same way as enzyme-catalyzed reaction, with substrate and product being the same metabolite but in different compartments. For all the four transporters in the model in chapter 5, the pyruvate transporter, citrate-isocitrate carrier, dicarboxylate carrier and the oxaglutarate carrier, the transporter kinetics is described by the rapid equilibrium random-bi-bi enzyme kinetics, as previously modeled in Yugi and Tomita [116]. There are two sub-types of transporters: antiporters, which transport the two metabolites in opposite directions, and symporters, which transport the two metabolites in the same direction (Figure 3.9).

The overall reaction scheme of the rapid equilibrium random-bi-bi enzyme kinetics is shown in figure 3.10. The derivation of rate expression follows the same steps as outlined for the fumarase kinetics. These complex rate expression need not be manually derived ,as there are many software tools available to carry out the derivation automatically such as SBMLsqueezer [18]. The kinetic expression for this mechanism is described in equation 3.48.

$$\frac{\frac{[\mathtt{A}]\cdot[\mathtt{B}]\cdot \mathtt{v_{mf}}}{\alpha\cdot \mathtt{KiA}\cdot \mathtt{KiB}} - \frac{[\mathtt{P}]\cdot[\mathtt{Q}]\cdot \mathtt{v_{mr}}}{\beta\cdot \mathtt{KiP}\cdot \mathtt{KiQ}}}{1 + \frac{[\mathtt{A}]}{\mathtt{KiA}} + \frac{[\mathtt{B}]}{\mathtt{KiB}} + \frac{[\mathtt{P}]}{\mathtt{KiP}} + \frac{[\mathtt{Q}]}{\mathtt{KiQ}} + \frac{[\mathtt{A}]\cdot[\mathtt{B}]}{\alpha\cdot \mathtt{KiA}\cdot \mathtt{KiB}} + \frac{[\mathtt{B}]\cdot[\mathtt{P}]}{\gamma\cdot \mathtt{KiB}\cdot \mathtt{KiP}} + \frac{[\mathtt{Q}]\cdot[\mathtt{B}]}{\delta\cdot \mathtt{KiB}\cdot \mathtt{KiQ}} + \frac{[\mathtt{A}]\cdot[\mathtt{P}]}{\xi\cdot \mathtt{KiA}\cdot \mathtt{KiP}} + \frac{[\mathtt{P}]\cdot[\mathtt{Q}]}{\beta\cdot \mathtt{KiP}\cdot \mathtt{KiQ}}} \tag{3.48}$$

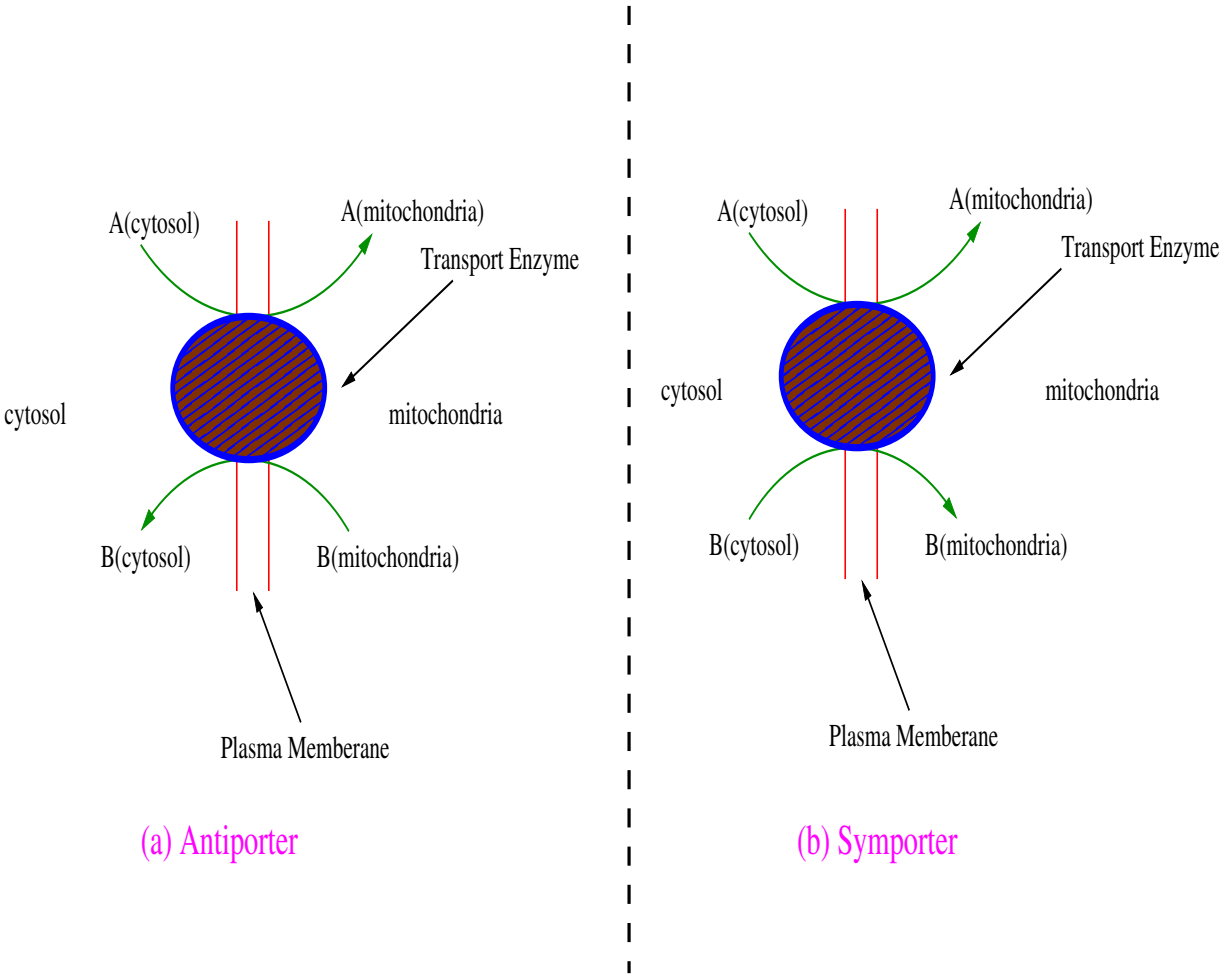

Figure 3.9: Schematic illustration of antiporter and symporter transporters across the plasma membrane

where $\mathtt{v}_{\{\cdot\}}$ are the forward and reverse turnover rates of the enzyme and $\mathtt{K}_{\mathtt{i}\{\cdot\}}$ are the Michaelis constants and $\alpha, \beta, \gamma, \delta, \xi$ are dissociation constant.

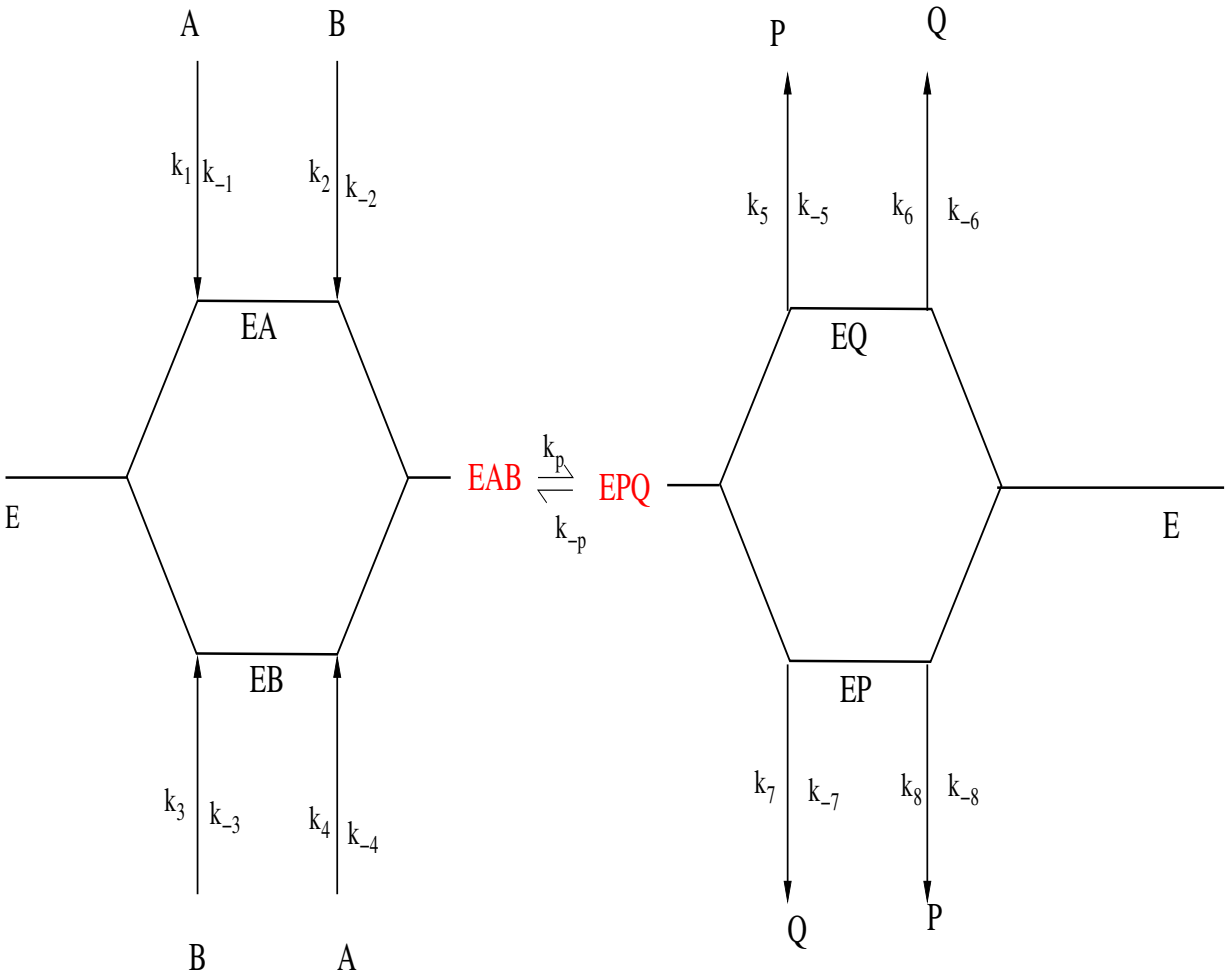

Figure 3.10: The overall reaction scheme for a rapid equilibrium random Bi-Bi kinetic reaction

3.2 Structural Analysis of Metabolic Pathways

We next review some properties of kinetic models that can be understood by analysis of the stoichiometry matrix. These are sometimes known as structural properties of the metabolic pathway. These analyses are valuable as a consistency check of the model, by identifying

metabolite conversation in the pathway. Conservation analysis can lead to simplification of the system of ODEs which can lead to more efficient solution.

Stoichiometry coefficients are defined as the "proportion of substrate and product molecules involved in a reaction". For example, consider the simple reversible reaction $A \rightleftharpoons B$ where A and B are two chemical species. For this reaction, the stoichiometric coefficient of A is -1 and for B is 1. The stoichiometry matrix is constructed from the stoichiometric coefficients of all reactions within a pathway. This matrix is organized in such a way that every column corresponds to a reaction and every row corresponds to a compound. The stoichiometric matrix for above reaction is simply $[1, -1]^T$. It is important to note is that the assignment of the stoichiometric matrix is not unique, since the ordering of the species and reaction can be re-arranged. For a metabolic pathway having m metabolites and r reactions, the stoichiometric matrix is a matrix N of size $m \times r$.

Systems Equations Consider a metabolic pathway consisting of m species and r reactions. The system dynamics is described by:

$$\frac{dS_i}{dt} = \sum_{j=1}^{r} n_{ij} v_j \quad \text{for} \quad i = 1, ...m \tag{3.49}$$

where n_{ij} is the stoichiometric coefficient of metabolite i in reaction j and v_j is the j^{th} reaction rate.

Now, we build a stoichiometric matrix N from stoichiometric coefficients n_{ij} assigned

to the substance S_i and the reactions v_j as:

$$N = n_{ij} \quad \text{for} \quad i = 1, ..., m \quad \text{and} \quad j = 1, ..r \tag{3.50}$$

Here, each column belongs to a reaction and each row to a substance.

Let us define a metabolic pathway with concentration values vector as $S = (S_1, ...S_n)^T$, reaction rates vector $v = (v_1, ...v_r)^T$ and a parameter vector $p = (p_1, ...p_m)^T$ with the stoichiometric matrix N. If the system is in steady state, we can also consider the vector $J = (J_1, J_2, ...J_r)^T$ containing the steady state fluxes. With this notation putting the information together the balanced equations can be represented as:

$$\frac{dS}{dt} = Nv(p) \tag{3.51}$$

Properties of the Stoichiometric Matrix N Analysis of the matrix N can reveal important information about the structural properties of the pathway. Analysis of the stoichiometric matrix can identify which combinations of individual fluxes are attainable in steady state. Moreover, dead-ends and un-branched reaction pathways can easily be calculated from stoichiometric matrix. Furthermore, we can discover the conservation relations in the pathway.

Supposing that equation 3.51 is in steady state, we have:

$$\frac{dS}{dt} = Nv = 0 \tag{3.52}$$

The product Nv is a linear system of equations that constrains the reaction rates v. This equation has nontrivial solutions only for rank $N < r$. Next, we define the kernel matrix K such that

$$NK = 0 \tag{3.53}$$

Equation 3.53 describes linear dependencies among the reaction rates. The kernel matrix K is not unique. Equation 3.53 can be solved using, e.g. Gaussian elimination [86]. Every possible set of steady-state fluxes can be expressed as a linear combination of the columns k_i of K:

$$J = \sum_{i=1}^{r-rank(N)} \alpha_i \cdot k_i \tag{3.54}$$

The coefficients must have appropriate units (M $\cdot$ s^{-1} or mol $\cdot L^{-1} \cdot s^{-1}$). Now we can analyze following properties of the metabolic pathway

1. If the entries in a certain row are zero in all basis vectors, we have found an equilibrium reaction. In any steady state, the net rate of the respective reaction must be zero.

2. If all basis vectors contain the same entries for a set of rows, this indicates an unbranched reaction path. In each steady state, the net rate of all respective reactions is equal.

In the previous analysis all the reactions are considered to be reversible reactions. If a reaction is irreversible then extra constraints are to be put on the kernel matrix K, but the stoichiometric matrix N remains unchanged. Extra conditions can be placed on the set of vectors belonging to K such that some values may not become negative or positive depending upon the way flux direction is defined.

Identification of Conservation Relation from Null Space of N^T Now we explain the derivation of conservation relations in metabolic pathways. If the total concentration of substance remains constant, which can be the case where substance is neither added or removed from the reaction system then the substance is conserved in the reaction system. The conservation will be preserved even if the substance interacts with the other substance and forms a complex.

To identify conservation in metabolic pathway we start by defining a matrix G such that:

$$GN = 0 \tag{3.55}$$

Substituting in equation 3.51, we have

$$G\dot{S} = GNv = 0 \tag{3.56}$$

Integrating this equation we have the conservation relations:

$$GS = const \tag{3.57}$$

where, n is the number of metabolites in the system. Furthermore, the number of linearly independent rows of G is equal to $n - rank(N)$. G^T is the kernel matrix of N^T, having properties similar to kernel matrix K. The matrix G can also be calculated using Gaussian elimination [86]. Matrix G is not unique, since every linear combination of its rows is again a valid solution.

Conservation analysis is very important in the context of kinetic modeling, as identifica-

tion of conservation relations will lead to simpler ODE system. To carry out the reduction first the rows of the stoichiometric matrix N and its concentration vector S are reordered in such a way that all the independent rows are at the top and dependent rows are at the bottom. This way of splitting the matrix into a linearly independent part N^0 and a dependent part N' can be carried out. Therefore, the system of equation can be written as follows:

$$N = (N^o N') = LN^o = (I_{rank}, NL')N^o \tag{3.58}$$

where, L is called the Link matrix

Where, $I_{rank(N)}$ is the identity matrix of size rank(N). The system of differential equation becomes:

$$\dot{S} = (\dot{S}_{indep}\ \dot{S}_{dep}) = (I_{rank(N)L'})N^o v \tag{3.59}$$

and the dependent concentration satisfies

$$\dot{S}_{dep} = L' \cdot \dot{S}_{indep} \tag{3.60}$$

Integration leads to

$$S_{dep} = L' \cdot S_{indep} + const \tag{3.61}$$

This relation holds true for the entire time course. Thus we may replace the original system by a reduced equation system

$$\dot{S}_{indep} = N_o v \tag{3.62}$$

This equation together with the set of algebraic equations describes the complete system dynamics. These elementary stoichiometric analyses are useful to identify conservation if present in the model which might not be implicit in the model structure and to check the system of differential equations.

3.3 Local Sensitivity Analysis

To study the effect of individual parameter perturbation on the model output, the method of local sensitivity analysis is used (LSA). In this section we summarize steady state LSA of kinetic models.

Consider quantity $y(x)$ which depends on another quantity x. The local effect of a change $\triangle x$ on y can expressed in terms of a sensitivity coefficient:

$$C_x^y = \left(\frac{x}{y} \frac{\triangle y}{\triangle x} \right)_{\triangle x \to 0} \tag{3.63}$$

For example, $\triangle x$ might be e.g. a one percent change of x. The normalization factor x/y makes the coefficient independent of units and of the magnitudes of x and y. The advantage of having unit-independent coefficient is that sensitivities can be compared across different reactions. However, normalization is not possible if $y = 0$, which may happen for certain parameter combinations. In the limiting case $\triangle \to 0$ the coefficient can be defined as:

$$C_x^y = \frac{x}{y} \frac{\partial y}{\partial x} \tag{3.64}$$

Which can be restated mathematically as:

$$C_x^y = \left(\frac{\partial \ln(y)}{\partial \ln(x)} \right) \tag{3.65}$$

We next review two interpretations of the LSA coefficient: the flux control coefficients and response coefficients of metabolic control analysis (MCA). For a comprehensive description of MCA, readers are referred to excellent texts by Fell [24], Klipp *et al.* [60], and Heinrich and Schuster [35].

3.3.1 Sensitivity Coefficients

Flux Control Coefficients Before we define the sensitivity coefficients of MCA it is important to emphasize that all this analysis has the strict condition that the metabolic pathway is operating at a stable steady state. Let us consider the steady state concentration $S = S(p)$ and steady state fluxes $J = v(S(p), p)$ of the pathway. In the limit of a very small perturbation of an individual reaction rate by a parameter change $v_k \rightarrow v_k + \triangle v_k$, we drive the system to a new steady state with $J \rightarrow J + \varepsilon_1 J$ and $S \rightarrow S + \varepsilon_2 S$. The flux control coefficient for the control of rate v_k over flux J_j is defined as

$$C_k^j = \frac{v_k}{J_j} \frac{\partial J_j}{\partial v_k} \tag{3.66}$$

whereas the concentration control coefficient of concentration S_i with respect to v_k reads

$$C_k^i = \frac{v_k}{S_i} \frac{\partial S_i}{\partial v_k} \tag{3.67}$$

The control coefficients measure the control that a given reaction v_k applies on the steady state flux J or on the steady state concentration S_i, respectively. It is assumed that the change εv_k is caused by change in a parameter p_k that has a direct effect only on v_k. Thus it holds that

$$\frac{\partial v_k}{\partial p_k} \neq 0 \quad \text{and} \quad \frac{\partial v_l}{\partial p_k} \neq 0 \quad (l \neq k) \tag{3.68}$$

This parameter might be the enzyme concentration, a kinetic constant or the concentration of a specific inhibitor or effector. Hence, we can define the flux control coefficient is:

$$C_k^j = \frac{v_k}{J_j} \frac{\partial J_j / \partial p_k}{\partial v_k / \partial p_k} \tag{3.69}$$

Response Coefficients To understand the effect of generic kinetic parameter p_m other than enzyme concentration (i.e. V_{max}) Kascer and Burns [53] defined the Response Coefficient. They assumed that the parameter influences the behavior of the system, but can be held constant after it has been altered while the system reaches a new steady state. The response coefficients are defined as:

$$R_m^j = \frac{p_m}{J_j} \frac{\partial J_j}{\partial p_m} \quad \text{and} \quad R_m^i = \frac{p_m}{S_i} \frac{\partial S_i}{\partial p_m} \tag{3.70}$$

where the first coefficient expresses the response of the flux to a parameter perturbation while the latter describes the response of a steady state concentration.

3.4 Global Sensitivity Analysis

As more and more experimental data become available, the size of published kinetic models also increases. Often, many parameters are derived from different cell types and exhibit significant experimental error. Furthermore, a subset of these parameters are not fit directly to data, but instead are calibrated to reproduce experimental observations of the system for which the kinetic model is developed. As a consequence, kinetic parameters often have significant uncertainty associated with their values. Furthermore, biochemical regulation is a very complex mechanism, exhibiting multiple ways of regulating biochemical process. Thus, the study of interaction between parameters can lead to important identification of model behavior. In other words, a individual parameter might not have a significant effect on model behavior in isolation, but in combination with certain parameters, could lead to important change in model behavior. Through local sensitivity analysis, we cannot study model behavior that can account for these effects, as local sensitivity is limited to individual parameter perturbations. So, we need new analysis methods through which we can study the associated uncertainty with parameters and interaction effects among parameters. For this purpose, global sensitivity analysis (GSA) is a very effective analysis method.

One definition of GSA, according to Salteli *et al.*, is: "The study of how uncertainty in the output of a model (numerical or otherwise) can be appropriated to different sources of uncertainty in the model input". For model analysis, we made use of the Partial rank correlation coefficient (PRCC), the variance-based GSA method; the extended Fourier amplitude sensitivity test (eFAST), and Sobol's method. The reason for using multiple sensitivity analysis is that the GSA sensitivity measures depend on the method used, and

comparative study of the sensitivity measures of different methods can lead to identification of important model behavior. Details about the mathematical background of the methods is provided in Chapter 4. The computational set-up for GSA for the model is provided in the appendix A.2.3.

Chapter 4

Computational Techniques

Chapter Outline In this chapter we will present the brief overview of mathematical methods used in the project. First, we summarize the dynamic parameter identification using the simplex algorithm and the simulated annealing algorithm (SA). Then we will discuss the steady state calculation using a combination of an ODE solver and nonlinear-equation solvers. Second, we summarize the methods of derivative approximations used during the project. Third, we summarize the methods of global sensitivity analysis (GSA) used in the project. Finally, we conclude with a proposal to use a surrogate modeling frame work for parameter identification in large kinetic models.

4.1 Parameter Identification

In this section we will describe parameter identification procedures for ordinary differential equation (ODE) kinetic models. We used two optimization algorithms: Nelder-Mead [79]

and simulated annealing algorithm (SA) [59] for the purpose of parameter identification. Here, we will summarize the these two algorithms. Next, we describe the MATLAB® ODE15s function algorithm which was used to solve the ODE. Finally, we explain the MATLAB® fsolve function algorithm which was used to achieve a steady state solution.

Objective Function Let us first describe the mathematical frame-work for an ODE based kinetic models. A Kinetic model of a metabolic pathway can be described by the following continuous ordinary differential equations:

$$\begin{aligned} \dot{x} &= f(x(t), u(t), p), \\ x(t_0) &= x_0, \\ y(t) &= g(x(t)) \end{aligned} \tag{4.1}$$

Where $x \in R^n$ is the systems state vector (metabolite) for a metabolic pathway, $p \in R^k$ is the system parameter vector, $u(t) \in R^p$ is the system input, $y \in R^m$ denotes the measured data, and x_0 is the initial state. $f(\cdot)$ is a set of functions describing the dynamical properties of a biological system like rate expressions. Finally, $g(\cdot)$ represents a measurement function such that if all the states are known then $g(\cdot)$ becomes an identity matrix. Otherwise, corresponding rows are deleted from I_n whose experimental values are unknown.

To identify the parameters of the ODE cost function can be stated as follows:

$$OBJ_0 : min_{\hat{p},\hat{x_0}} \sum_{j=0}^{N-1} \sum_{i=1}^{n} w_{ij} ||y_i(t_j) - \hat{y}_i(t_j|\hat{p})||_l, \tag{4.2}$$

$$\text{such that} \begin{cases} \hat{\dot{x}}(t_j) = f(\hat{x}(t_j|\hat{p}), u(t), \hat{p}), \quad x(t_0) = \hat{x}_0, \\ \hat{y}(t_j) = g(\hat{x}(t_j|\hat{p})), \quad j = 1, 2, ...N-1 \\ p_l \leq \hat{p} \leq p_u \end{cases}$$

OBJ_0 measures the fitness of the model with respect to given experimental data, where $\hat{p} \in R^k$ is the set of parameters to be identified, $|| \cdot ||_l$ denotes the l-norm with $l > 0$, $\hat{x_0}$ is the estimated initial condition, $\hat{x} \in R^k$ is the estimated system states $\hat{x}(t_j|\hat{p})$ represents the estimated variable at t_j with parameter $\hat{p}$ and initial condition $\hat{x_0}$, w_{ij} are the weighting coefficients, $\hat{y}$ is the estimated measured data. Finally, p_l and p_u are lower and upper bounds on the parameters and are also referred to as box constraints.

To minimize OBJ_0 a number of optimization algorithms can be used. Special attention needs to be paid to the fact that the derivative of the cost function is not easily available and accuracy is limited since derivatives needs to be evaluated at each iteration. In the concluding section of this chapter we will discuss ideas about solving the problem more efficiently.

The objective function defined in equation 4.2 is the generalized statement of kinetic model parameter estimation. The objective function used to estimate the parameter in the current study is discussed in Appendix A.2.2.

4.1.1 Optimization Algorithm

Here we describe two algorithms which we used to estimate parameters as described Press [86] and implemented in SBTOOLBOX2 [97].

Simplex Algorithm Nelder and Mead [79] in their pioneering work developed a derivative free optimization algorithm for multidimensional unconstrained (box constraints can easily be included) optimization. Since the method does not require derivative information, the method is suitable for problems involving non-smooth functions and parameter estimation problems of ODEs.

We use the notation of the Conn *et al.* [12]. The Nelder-Mead [79] algorithm is designed for classic nonlinear unconstrained minimization of a nonlinear function $f : \mathbb{R}^n \rightarrow \mathbb{R}$. Nelder-Mead [79] is simplex based method where a simplex S in $\mathbb{R}^n$ is defined as the geometrical figure consisting in N dimension of N+1 points and all their interconnecting line segments [86]. For example, in two dimension simplex is a triangle, in three dimension it is tetrahedron, not necessarily a regular tetrahedron. In other words a simplex S in $\mathbb{R}$ is the convex hull of $N+1$ points (vertices's) $y_0, \ldots, y_n \in \mathbb{R}^n$ [12]

A simplex based method begins with a set of $N+1$ points $y_0, \ldots, y_n \in \mathbb{R}^n$ that are considered as the vertices's of a working simplex S, and the corresponding set of function values at the vertices's $f_i = f(y_i) \quad \text{for} \quad i = 0, \ldots, n$ given constrain that working simplex S is non-degenerate that is the points $y_0, \ldots, y_n$ must not lie in the same hyperplane. With in these mathematical constraints the algorithm performs a sequence of transformations of the working simplex S, in order to decrease the function values at its vertices's. At

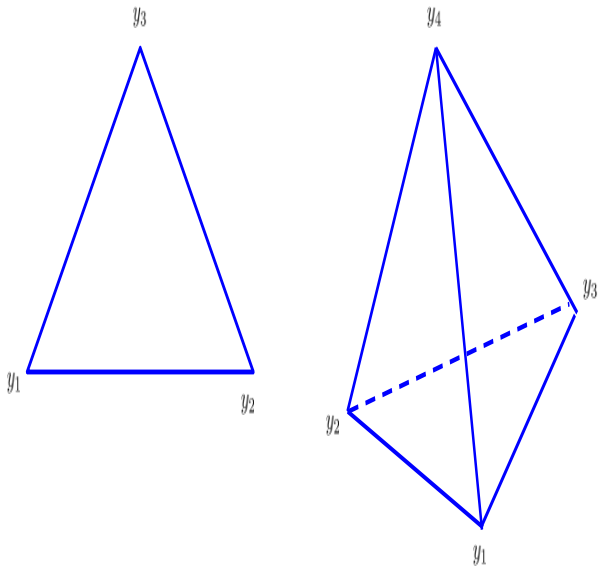

Figure 4.1: Simplex in 2 and 3 dimensions.

each iteration a series of test points are calculated together with function values, and then function values are compared based on which transformation is determined.

Description of Algorithm The initial simplex S is generally constructed by generating $n+1$ points around $y_0, \ldots, y_n$ around a given input point $y_{in} \in \mathbb{R}^n$. Press [86] recommends that this point be chosen to be $y_0 = y_{in}$ since this can allow proper restart of the algorithm. The remaining n points are then constructed based on:

- S is right angled at y_0 based on coordinate axes, or

$$y_i = y_0 + \delta_i e_i, \quad i = 1, \ldots, n \tag{4.3}$$

where δ_i is the step size in the direction of unit vector $e_i \in \mathbb{R}^n$

- S is a regular simplex, where all edges have the same specified length.

Next, the Nelder-Mead method takes series of steps or transformations in order to move the points of the simplex such that function value is lowest among all simplex point. These steps transformations are called reflections and to maintain non-degeneracy they are constructed in such a way to preserve the volume. Under this assumption, the method expands the simplex in one or another directions to take larger steps. Next, depending on the function value the method contracts itself: in the transverse direction if encounters valley or contracts itself in all direction if the function value is decreasing sharply.

Stopping Criteria Termination criteria in any multidimensional minimization routine should be decided with significant care. Two set of criteria usually works best for the optimization. First, optimization can be terminated when the vector distance moved in the current step is fractionally smaller in magnitude than some tolerance tol. Second, we could require that the decrease in function value in the terminating step be fractionally smaller than some tolerance ftol. Press [86] recommended that tol should not usually be smaller than the square root of the machine precision, but it is perfectly appropriate to let ftol be of order the machine precision.

In derivative free methods like the Nelder-Mead stopping criteria can easily return wrong solutions or stop prematurely before reaching actual minima. Nevertheless, the stopping criteria in derivative-free methods are an active area of research. The simplest work around to overcome this problem is to restart a multidimensional minimization routine

at a point where it claims to have found a minimum. Press [86] suggests that for this restart re-initialization can be done through any ancillary input quantities. For example, the downhill simplex method can be reinitialized at any of N of the N+1 vertices's of the simplex again by equation 4.3 y_0 being one of the vertices's of the postulated minimum.

Convergence The convergence analysis of the Nelder-Mead method is a nontrivial problem and is currently actively pursued. The details of the convergence properties of the Nelder-Mead method can be found in the book by Conn [12].

Simulated Annealing (SA) The method of SA is inspired from the thermodynamics process called annealing. In the annealing process, liquids are heated and cooled slowly. In statistical physics the annealing process is modeled using the Boltzmann probability distribution defined as,

$$Prob(E) \sim exp(\frac{-E}{kT}) \tag{4.4}$$

where, k is Boltzmann's constant, E is the energy of the state and T is the temperature. The physical meaning of the Boltzmann equation is that a system in thermal equilibrium at temperature T has its energy probabilistically distributed among all different energy states E. In the transitions the system looks for the minimum energy states or in other words this to minimize its energy. Metropolis *et al.* [71] used these principles to simulate a thermodynamic system such that the system makes transitions from energy E_1 to energy E_2 with probability $p = exp[-\frac{(E_2-E_1)}{kT}]$ with the condition that if $E_2 < E_1$ then $p = 1$ (since in this case probability is greater tha 1). Now, a thermodynamic system makes both high energy transitions and low transitions eventually finding its minimum energy state. This

is called the Metropolis algorithm.

Kirkpatrick *et al.* [59] using same idea introduced a minimization algorithm for non-thermodynamic systems which is known as simulated annealing algorithm (SA). In the Kirkpatrick *et al.* paper this algorithm was used to solve a discrete problem, however the SA can easily be extended to continuous system with the some refinements. Consider, the continuous function $f(x)$ such that $x \in \mathbb{R}^n$. To minimize f we have to reformulate SA as follows:

- The f is the objective function.
- The system state is now x.
- The control parameter T is like a temperature with an annealing schedule by which it is gradually reduced and there must be a generator of random changes in the configuration that is the procedure for taking a random step x to $x+ \triangle x$

Implementation of SA The SA algorithm is implemented as the simplex algorithm with the difference that the next simplex move is decided by the SA algorithm. The algorithm includes the box constraints. Complete details of the computational implementation can be found in Press [86]. The method is implemented in SBTOOLBOX2 [97] with box constrained (that is bounds on x) which was used for parameter estimation in the current study.

It is important to discuss the annealing schedule of SA algorithm, since the success of SA depends significantly on the type of annealing schedule used. Next, we discuss an annealing schedule tried during parameter optimization as recommended in Press [86]:

1. The decrease in T is scheduled in such a way that T reduces by $(1-\epsilon)$T after every m moves, where ϵ/m is determined by heuristics.

2. T is assigned a value using $T = T_0(1-\frac{k}{K})^{\alpha}$ after every m moves, where α is a constant values that can be chosen between 1 and 4, k is the cumulative numbers of moves thus far, K is preassigned total number of temperature reductions. While choosing the value of α it should be considered that a larger value of α implies larger spent time at lower temperature.

3. Finally, schedule T reduction in T after m moves such that T reduces by the factor of $\beta \cdot f_1 - f_b$, where β is constant between 0 and 1, f_1 is the smallest function value of the current simplex, and f_b is the best function so far achieved by the algorithm. Important restriction is that the T should not be reduced more than some fraction γ at a time.

Stopping Criteria and Convergence of SA The stopping criteria of the algorithm in this implementation of SA is the same as discussed for Nelder-Mead algorithm. The convergence results for SA algorithm are not yet available, however some discussion can be found in the book by Laarhoven *et al.* [61].

SA offers many advantages suitable for kinetic model parameter estimation. First the algorithm is not greedy that it is not tricked by the quick payoff achieved by falling into unfavorable minima. Provided that sufficiently general reconfiguration are given, it wanders freely among local minima of depth less than about T. As T is lowered the number of such minima qualifying for frequent visit is gradually reduced. Second, the configuration

decisions tend to proceed in a logical manner. Changes that cause the greatest energy difference are shifted over when the control parameter T is large. These decisions become more permanent as T is lowered and attention then shifts more to smaller refinements in the solution.

4.1.2 Solving the Model for Steady State

ODE solver In this section we discuss the backward differentiation formula (BDF) for solving a stiff set of ordinary differential equation (ODE).

The method can be used to solve an initial value problem of the type,

$$y' = F(t, y) \tag{4.5}$$

on a time interval $[t_0, t_f]$, given initial condition $y(t_0) = y_0$. More broadly these methods can be used to find solutions of the problem:

$$M(t)y' = f(t, y) \tag{4.6}$$

With a mass matrix $M(t)$ that is non singular and sparse. However, our focus is on the solution of equation 4.5

Implicit formulas for stiff systems The BDF are very popular for solving stiff ODE problems. When the step size is a constant h and backward differences are used, the

formula of order k, BDFk, for a step from (t_n, y_n) to (t_{n+1}, y_{n+1}) is

$$\sum_{m=1}^{k} \frac{1}{m} \nabla^m y_{n+1} - hF(t_{n+1}, y_{n+1}) = 0 \tag{4.7}$$

The simplified Newton method (chord) is used to solve the algebraic equation for y_{n+1}. The iteration is started with the predicted value:

$$y_{n+1}^0 = \sum_{m=0}^{k} \nabla^m y_n. \tag{4.8}$$

The truncation error of the BDFk leading term is given by:

$$\frac{1}{k+1} h^{k+1} y^{(k+1)} \approx \frac{1}{k+1} \nabla^{k+1} y_{n+1} \tag{4.9}$$

This is the general formula for BDFs. In MATLAB® ODE15s the above formula is implemented in a slightly modified form. Details about the implementation can be found in Shampine and Reichelt [104]. We used the order 2 that is, $k = 2$, to solve the system of ordinary differential equations, since the order 2 offers maximum stability for the solver. Next, The non-linear equation solver fsolve was used to check for the steady state reached by the ODE solvers. Since, many times the solution returned by the ODE solver was not the actual steady state so this check pointing was necessary for a consistency check of the steady state. We used the "Trust-region-dogleg" method for solving the system of non-linear equations. The details of the solver settings are documented in appendix A.2.1. Since these methods are well established and not the subject of focus in the current work, we will not discuss these methods in detail. The detailed description of the MATLAB®

ODE suite and fsolve algorithm can be found elsewhere in [104, 83].

4.2 Derivative Computation

Numerical approximation of derivatives is required for sensitivity analysis, and for Jacobian estimation for ODE and nonlinear equations simulation algorithms (and for derivative-based optimization routines). In this section we outline three methods for approximation of derivatives: difference approximation, automatic differentiation (AD), and symbolic differentiation. In the current study, difference approximation methods were used to evaluate local sensitivity coefficients, while AD and symbolic differentiation were used for Jacobian estimation for the implicit simulation of the ODE system.

4.2.1 Numerical Approximation of Derivatives

In this subsection we will review numerical approximation of derivatives, using the notation of Elden *et al.* [22]. Let the function f be continuous and differentiable. Suppose function value is known for points $x - h$, x and $x + h$ where h is a small number. Our goal is to approximate the derivative $f'(x)$, that is, the slope of the tangent of the curve $y = f(x)$ at the point x. We can obtain a forward difference, denoted $D_+(h)$, by approximating f by the line through the points $(x, f(x))$ and $((x + h), f(x + h))$ as follows (Figure 4.2),

$$f'(x) \simeq D_+(h) = \frac{f(x+h) - f(x)}{h}. \tag{4.10}$$

Alternatively, we can define the central difference approximation, $D_0(h)$, as the slope of straight line through the points $((x-h), f(x-h))$ and $((x+h), f(x+h))$ (Figure 4.2),

$$f'(x) \simeq D_0(h) = \frac{f(x+h) - f(x-h)}{2h} \tag{4.11}$$

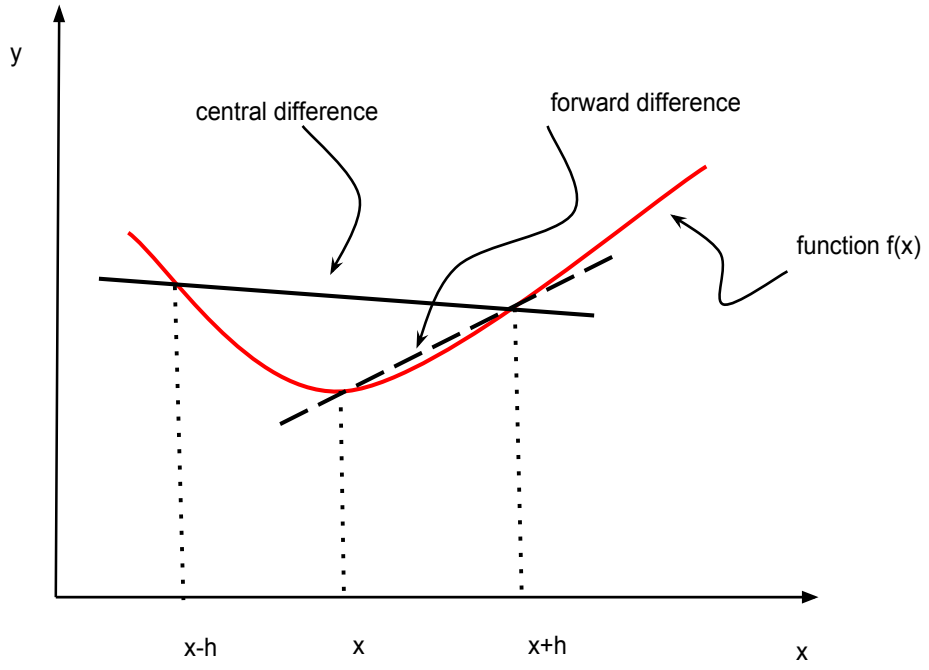

Figure 4.2: Schematic illustration of difference approximations.

Approximation Error Next we present the error analysis of the difference approximation. The difference approximation has truncation error R_T which can be approximated by Taylor series approximation. Let f be a twice continuously differentiable function, whose first derivative is approximated by forward difference. Then:

$$\begin{aligned} R_T = D_+(h) - f'(x) &= \left(\frac{1}{h}(f(x+h) - f(x)\right) - f'(x) \\ &= \frac{1}{h}(f(x) + hf'(x) + \frac{1}{2}h^2 f''(\xi) - f(x)) - f'(x) \\ &= \frac{1}{2}hf''(\xi) \end{aligned} \tag{4.12}$$

where ξ denotes point in the open interval $(x, x+h)$. ξ and $f''(\xi)$ are unknown, but we can observe that the truncation error is $O(h)$ as $h \to 0$. This implies that if $f''(x)$ is constant for values close to x, then R_T will be halved if the value of h is halved.

Let us keep the higher order terms of Taylor expansion then we get:

$$\begin{aligned} R_T = D_+(h) - f'(x) &= \frac{1}{2}f''(x)h + \frac{1}{3!}f^{(3)}(x)h^2 + \frac{1}{4!}f^{(4)}(x)h^3 + ... \\ &= a_1 h + a_2 h^2 + a_3 h^3 + ... \end{aligned} \tag{4.13}$$

Where $a_k = \frac{f^{(k+1)}(x)}{(k+1)!}$. Similarly, for central difference approximation we have:

$$D_0(h) - f'(x) = b_1 h^2 + b_2 h^4 + b_3 h^6 + ... \tag{4.14}$$

We observe given $b_1 \neq 0$ and $\frac{b_k}{b_1}$ is not very large then we have $R_T \simeq b_1 h^2$ provided h is very small. It can be further observed that $D_0(h)$ gives better approximation compared to $D_+(h)$ with exception for the case when $a_1 \ll |b_1|$.

Richardson Extrapolation Since, the difference approximation was used to perform the steady state local sensitivity analysis, we refined the results using the Richardson Extrapolation method. Through this extra evaluation we can check for error in difference approximation due to ODE solver failure and if any discontinuity is present in the result. This practice can increase our faith in the results especially for the large kinetic models.

We explain the Richardson Extrapolation using central difference method 4.11 as described in Elden *et al.* [22]. Consider the central difference approximation

$$F(h) = \frac{f(x+h) - f(x-h)}{2h} \tag{4.15}$$

The idea behind Richardson extrapolation is that if the function F is well behaved as $h \to 0$ and have computed the value of F for two different values of h then a good estimate of $F(0)$ can be computed. From the expression for the truncation error 4.14, it can be generalized that the truncation error between two arguments h and qh is proportional to h^p, given this Richardson extrapolation definition as quoted from Elden *et al.* [22] is:

Definition Richardson Extrapolation: If

$$F(h) = F(0) + ch^p + O(h^r), r < p, \tag{4.16}$$

with a known p and a unknown c, which are independent of h, then

$$F(h) + \frac{1}{q^p - 1}(F(h) - F(qh)) = F(0) + O(h^r) \tag{4.17}$$

Practical Implementation Now we provide the procedure for practical implementation of Richardson extrapolation. The idea is to perform repeated Richardson extrapolation. Consider the expansion:

$$F(h) = F(0) + a_1 h^{p_1} + a_2 h^{p_2} + ... \tag{4.18}$$

Now, let us assume that we know the exponents $p_1, p_2, ...$, but $a_1, a_2, ...$ are unknown. Finally, we assume that F has been computed for arguments $....q^3h, q^2h, qh, h$.

Next, let $F_1(h) = F(h)$, then we have:

$$F_{k+1}(h) = F_k(h) + \frac{1}{q^{p_k} - 1}(F_k(h) - F_k(qh)) \quad k = 1, 2, ... \tag{4.19}$$

Now, eliminate the h^{p_k}-term from the expansion we get.

$$F_{k+1}(h) = F(0) + \tilde{a_{k+1}} h^{pk+1} + \tilde{a_{k+2}} h^{pk+2} + ... \tag{4.20}$$

The above expansion can be arranged in the matrix form as follows:

$$\begin{array}{ccccccc}
F_1(q^3h) & & & & & & \\
F_1(q^2h) & F_2(q^2h) & & & & & \\
F_1(qh) & F_2(qh) & F_3(qh) & & & & \\
F_1(h) & F_2(h) & F_3(h) & F_4(h) & & & \\
\vdots & \dots & \dots & \vdots & \dots & \ddots &
\end{array}$$

Using this arrangement the values of function are calculated row by row and extrapolations

are done till consecutive values in the same column achieves desired accuracy. This rearrangement has advantage that difference between two adjacent values of the same columns provides an upper bound for the truncation error provided h is very small. In practice values of p and q are determined through experiments.

Conclusion Numerical approximations of derivatives are good substitutes for exact derivatives, which may not be available in many cases. We used forward difference approximation to estimate the local sensitivity coefficients which was further checked for accuracy using the Richardson extrapolation method. We used the MATLAB® implementation of Richardson extrapolation provided by Elden *et al.* [22].

4.2.2 Automatic Differentiation (AD)

In AD the function is broken down into the composition of elementary arithmetic operations to which the chain rule (differentiation chain rule) can be applied. AD has two basic modes of operations, the forward mode and the reverse mode. In the forward mode the derivatives are propagated throughout the computation using chain rule. The reverse mode computes the derivatives for all variables backwards (i.e. reverse order) through the computation. The reverse mode requires saving the entire computation trace since the propagation is done backwards through the computation. Hence the reverse mode can be prohibitive for certain problems due to memory requirements.

Jacobian Calculation The $m \times n$ Jacobian matrix of function $f : \mathbb{R}^n \rightarrow \mathbb{R}^m$ can be evaluated in forward mode by n sweeps of forward accumulation, such that each sweep

yields a column vector of the Jacobian matrix. Alternatively, in the reverse mode, m sweeps are needed; each sweep yields a row vector of the Jacobian.

AD and finite difference Next we compare the key difference between automatic differentiation and finite differences. The most significant advantage of AD is that it computes the derivatives exactly up to machine precision whereas finite differences incur truncation errors. Furthermore, the accuracy of finite difference depends on the step-size, which in many problem settings is difficult to best determine. In AD there is no need for selecting step size. It is important to note that if the function computation itself is not accurate (e.g. if the function evaluation incurs round-off errors), then these errors will appear in the AD process as well.

AD is also traditionally faster than finite difference since AD can take advantage of the problem structure. For the discussion on this topic see Griewank [27].

Current Limitations Although, automatic differentiation has proved to be useful technique for calculating accurate derivatives, its application is limited. For example, the evaluation of functions that depends on floating point arithmetic will involve truncation error τ. That is we have $\hat{f}(x) = f(x) + \tau(x)$, where $\hat{f(\cdot)}$ is the computed value of $f(\cdot)$ and $\tau(\cdot)$ is the truncation error. Although, $|\tau(x)|$ is small, its derivative $\tau'(x)$ might not be small quantity, so the error in the computed derivative $\hat{f}'(x)$ might be large. Error can also arise in the way the function evaluation is implemented in the automatic differentiation code. A frequent practice is to have branching in the code to improve the speed or accuracy of function evaluations in certain domains. For further discussion and an approach to

dealing with this issue readers can check into Griewank [27].

We conclude that automatic differentiation is a useful technique and can be used to solve many practical problems. Automatic differentiation facilitates interpretations of the computed optimal solutions, allowing the modeler to extract more information from the results of the computation. However, care should be taken while calculating derivatives as automatic differentiation has certain limitations.

4.2.3 Symbolic Differentiation

Symbolic differentiation involves the technique of computer algebra. In this method, a function f is decomposed into algebraic specification which is then manipulated by symbolic manipulation tools to produce a new algebraic expression for each component of the function gradient. A detailed discussion on the topic is beyond the scope of the present work; for more details, readers are referred to Pavelle *et al.* [84]. There are many packages available for symbolic computation, e.g. Mathematica, Maple, Mupad and many more. We used the MATLAB® symbolic computation tool (Mupad) implemented in SBTOOLBOX2 [97] to calculate the symbolic Jacobian of our ODE system. The use of the symbolic jacobian makes the ODE solver highly efficient, but care should be taken in using the expression since for certain values the expression might lead to a computer arithmetic problem. Especially, in the case of kinetic models, certain flux expressions might lead to NAN for certain initial conditions or parameter combinations.

4.3 Global Sensitivity Analysis (GSA): Introduction to PRCC, eFAST and Sobol's method

As discussed in chapter 3 section 3.4 GSA is an analysis method for exploring the effect of uncertainty in the parameters values. In this section we discuss three GSA methods: PRCC, eFAST method and Sobol's method. The basic assumption is that each input parameter is viewed as a random variable, with an associated probability density function (PDF) and a cumulative density function (CDF). These methods explore the effect of parameter variations on the model output. That is, they determine which parameters produce maximum variance in the output (4.3). The general procedure of the GSA method involves: assignment of a PDF to each input parameter, sample generation through a selected sampling method in the parameter space, evaluation of model output on each sample point, and finally a method to define the sensitivity measure.

4.3.1 Sampling Methods

For illustration let us consider a single output model defined as:

$$y = f(p) \tag{4.21}$$

where $p = (p_1, ...p_N)$ is the input parameter, with each coefficient assumed to lie in interval $p_i \in [\alpha_i, \gamma_i]$. The output function is then evaluated on M samples generated from a selected PDF. The construction of appropriate sample is significant in determining the output's

perceived uncertainty as well as the input's relative importance.

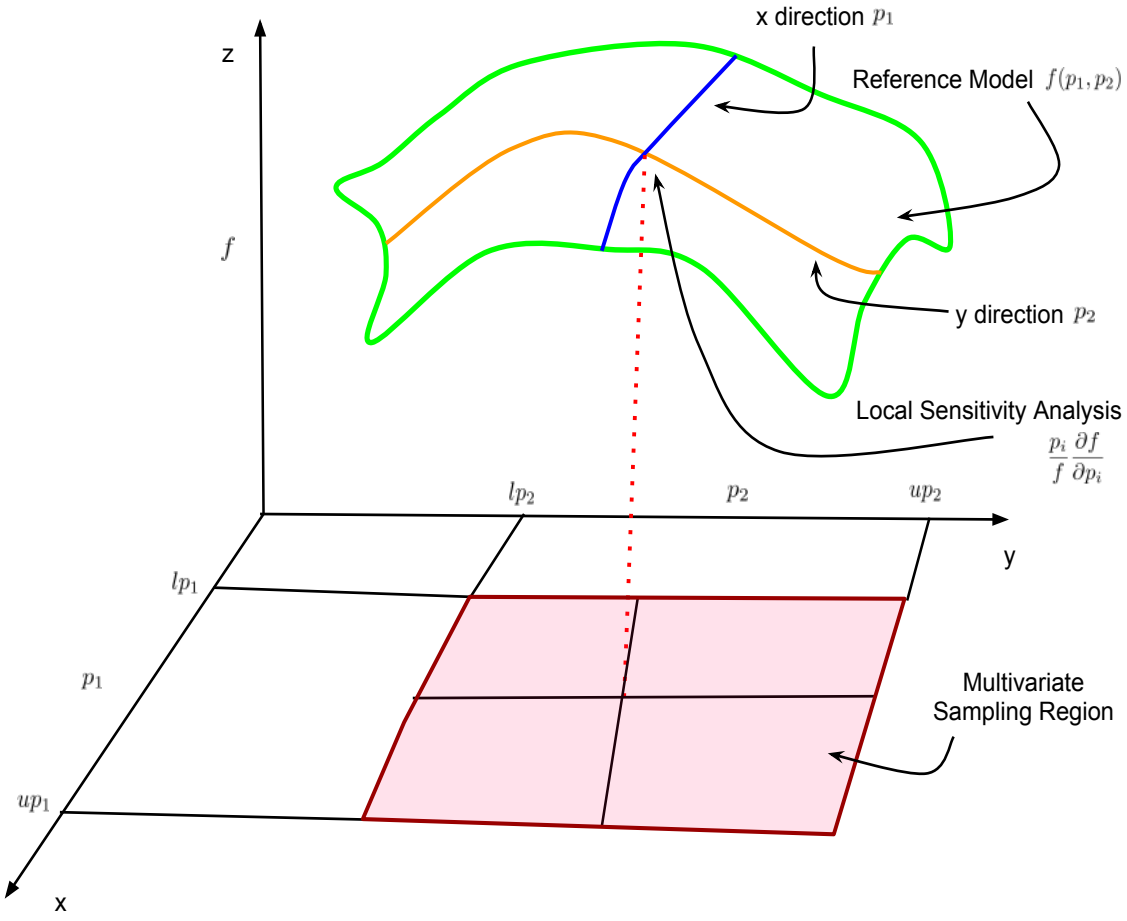

Figure 4.3: Schematic illustration of global sensitivity analysis (GSA). While local sensitivity analysis (LSA) is restricted the point at which analysis is done, a GSA measure scans the entire parameter space.

Random Sampling The most common approach is to select uniform random samples of numbers x in the interval $[0, 1]$. For the chosen number x, we determine the associated

sample value p_i, in the interval $[\alpha_i, \gamma_i]$, by finding the inverse of cumulative density function (CDF) that is $p = CDF^{-1}(x)$. This sampling method has two main advantages: it is easy to implement, and for large samples, it produces unbiased estimates of the mean and variance of output y. However, in the case where the sample interval $[\alpha_i, \gamma_i]$ is subdivided into a large number of equally sized sub-intervals then we need to take large number of samples which might be computationally very intensive.

Stratified Sampling A more elaborate sampling strategy is stratified sampling. In this method first the input parameter interval is divided into sub-intervals. Then, a random sample is chosen from each of the sub-intervals. The idea behind stratified sampling is to ensure that we obtain samples from each particular interval.

Latin Hyper-cube Sampling (LHS) is another commonly used stratified sampling method. LHS sampling can be viewed as a square with M equally divided rows and columns such that in each row and column one and only one cell is occupied. The motivation behind this strategy is to replace the concept of a particular cell being occupied with getting a sample from the particular associated sub-intervals. Further constraints are imposed on the sampling so that the distributions of samples will be evenly distributed from the sample sub-spaces.

Latin hyper-cube sampling is slightly easier to implement compared to other types of stratified sampling like orthogonal sampling. LHS methods return a sample that gives a good representation of variability, as well as reduces the variance in the output's evaluation. The significant advantage of using LHS is that we can can work with smaller samples sizes

without a major subsequent loss of quantification of the output's variance.

4.3.2 Regression based GSA Method

Partial Rank Correlation Coefficient (PRCC) analysis with Latin hyper-cube sampling The method of PRCC is useful for the nonlinear models where the relationship between input and output appears to be monotonic [19]. The input data is ranked in increasing order and the associated output is rearranged accordingly. Next, regression analysis on the ranked data is carried out to calculate the Pearson rank coefficients. Hence, these measures produce a sensitivity measure of how strong a correlation there is in the monotonicity between input and output. It is important to note that the method assumes that the input variables are independent of each other, i.e. the parameters are not correlated. Attention needs to be given to this assumption, otherwise erroneous results will be produced.

For software implementation we used the PRCC implemented in SBTOOLBOX2 [97]. The implementation uses the Pearson correlation coefficient measurement as described by Blower and Dowlatabadi [5]. The LHS sampling method was used as explained in the Mckay *et al.* [69]. The calculated sensitivity measures, which range between $[-1, 1]$, can be compared among different parameters.

4.3.3 Variance-Based GSA method

The limitations of PRCC can be overcome by using model-independent GSA methods. Variance-based GSA method are suitable for model-independent calculation of sensitivity

measures and are well established in the analysis community [93]. Variance based methods are useful for the following model analysis [93]:

- Parameter Prioritization: identifying parameters which will lead to maximum output variation.
- Parameter Fixing: identifying parameter variation range in which output variance will not vary beyond set threshold.
- Variance Cutting: identifying a set of parameters to reduce output variance below a certain threshold.
- Parameter Mapping: identification of parameter range for which desired output can be realized.

We used Sobol's method and eFAST for GSA which we describe next.

Sobol's Method In Sobol's method [42], the model output function $y = f(p)$ is decomposed into a unique sum of orthogonal functions of increasing dimension. The decomposition is as follows

$$D = \int f^2(p)dp - (\int f(p)dp)^2 \tag{4.22}$$

$$= \sum_{i=1}^{m} D_i + \sum_{1 \le i \le j \le m} D_{ij} + \cdots + D_{1,2,\cdots,m} \tag{4.23}$$

where m is the number of parameters, D is the overall variance of the model output, and $D_{i_1 \ldots i_s} (1 \le i_1 \ldots . i_s \le m)$ denotes the partial variance contributed by parameter combination

$\{i_1, i_2....i_s\}$. First order sensitivities are then defined as:

$$S_i = \frac{D_i}{D}$$

and the total sensitivity index (i.e. sensitivity coefficient) as:

$$S_{ti} = \frac{D_i^{tot}}{D}$$

where D_i^{tot} is the total variance due to i^{th} parameter.

For example, consider a single output, two input function:

$$y = f(p_1, p_2)$$

Then this function can be decomposed into orthogonal components:

$$y = F(p_1) + F(p_2) + F(p_1, p_2)$$

Then variance according to Sobol's method can be estimated as:

$$D = D_1 + D_2 + D_{1,2}$$

According to Sobol's method first order sensitivity for p_1, p_2 are then defined as,

$$S_1 = \frac{D_1}{D}, \quad S_2 = \frac{D_2}{D}$$

Next, the total sensitivity index for p_1 is defined as,

$$D_1^{tot} = D_1 + D_{1,2}, \quad S_1^{tot} = \frac{D_1^{tot}}{D}$$

Similarly, the total sensitivity index for p_2 is defined as,

$$D_2^{tot} = D_2 + D_{1,2}, \quad S_2^{tot} = \frac{D_2^{tot}}{D}$$

The significant computational challenge in Sobol's method is estimating the integral in 4.22, which Sobol [42] suggested to be estimated by Monte Carlo integration of the output functions on the random sampling basis. Sensitivity measure are then defined based upon the fraction of related partial variances in the overall variances. First order sensitivity measure indicates the impact of individual parameters on the model output, whereas the total effect sensitivity measure describes the effect of parameter interactions on the model output.

Interpreting Sobol's Sensitivity Index Let S_i be first order index and S_{ti} be total sensitivity index.

- S_i indicates by how much one could reduce, on average, the output variance if input parameter p_i could be fixed. Hence it is a measure of main effect of the parameter.
- $S_{i_1 \ldots i_s}$ indicates how much the output variance could be reduced, on average, if one could fix $p_{i_1}.....p_{i_s}$. $S_{ti} \geq S_i$ if parameter p_i is not involved in any other interactions.

- $S_{ti} - S_i$ is a measure of how much parameter p_i is involved in interactions with other input parameters. $S_{ti} \simeq 0$ implies p_i is non influential. $1 - \sum_i S_i$ is an indicator of the presence of interactions in the model.

eFAST The eFAST method developed by Saltelli *et al.* [92], which is an extension of the Fourier Amplitude Sensitivity Test (FAST) [15], has the advantage that it is possible to calculate total sensitivity measures in addition to first order sensitivity measure. In the eFAST method each uncertain input parameter $\hat{p}_i$ is sampled along curves defined by transformation 4.24 in the normalized unit m-dimensional parameter space, where m is the total number of parameters.

$$\hat{p}_i = \frac{1}{2} + \frac{1}{\pi} \arcsin(\sin(\omega_i s + \varphi_i)) \tag{4.24}$$

where each parameter varies periodically at an angular frequency ω_i and random phase shift φ_i, with a scalar variable $s \in (-\pi, \pi)$. Using this transformation 4.24, the model output function is expressed as a Fourier series with respect to s. Then, the properties of Fourier expansion can be applied, by which the overall variance of the output function D is decomposed into the square of Fourier series coefficients. Finally, using Monte Carlo integration on the sampled parameter space, these Fourier series coefficients are estimated, based on which the eFAST sensitivity measures are defined. A detailed discussion on the implementation method of eFAST can be found in Saltelli *et al.* [93]. The interpretations of the measure are the same as discussed previously for Sobol's method.

Interpreting Sensitivity Measure The interpretations of variance based sensitivity measure is same as illustrated in the example 4.3.3. Only the method of estimating the first order and total effect sensitivity measure differs between Sobol's method and eFAST. The PRCC sensitivity measure can be considered equivalent to total effect sensitivity measure of variance based method [93] provided the assumptions of PRCC holds for the model output (monotonicity relationship between input and output).

Implementation of the Variance Methods Both Sobol's method and the eFAST method are implemented in the SBTOOLBOX2 [97]. The toolbox implementation is based on the discussion of Zhang and Rundell [118]. For our model analysis, we calculated both the first order sensitivity measures and total effect measures. Details of our GSA analysis are documented in the appendix A.2.3. The sensitivity measures are analyzed in chapter 5.

Implementation of the Variance Methods Both the variance based methods are implemented in the SBTOOLBOX2 [97] and toolbox implementation is based on the discussion of Zhang and Rundell [118]. We calculated both the first order sensitivity measure and total effect measure. The details of GSA simulation is documented in appendix A.2.3 and the sensitivity measures are analyzed in chapter 5.

4.4 Dynamic Numerical Optimization using Surrogate Models

Parameter identification in large scale kinetic models is not trivial. The standard optimization procedure of parameter identification (described in Section 4.1) does not return, in many cases, the required solution. These optimization processes are influenced by many factors apart from quality of data, such as the choice of parameters and stability of ODE solvers. In addition, while the choice of parameters to be fit is often identified through sensitivity analysis, their degree of influence might vary during the optimization process, potentially causing the optimization algorithm to fall into the wrong local minimum. Furthermore, many times the system is undetermined, especially if parameter identification is based solely on steady state data. These shortcomings led us to explore alternative methods for parameter identification of the kinetic models.

In engineering there is a frequent practice to use a surrogate modeling framework to optimize functions whose evaluation is computationally expensive. In this surrogate modeling framework we look for a surrogate function $sm(x)$ of true function $f(x)$, such that $sm(x)$ is simpler to evaluate but reproduces the behavior of the true function $f(x)$. Next, we optimize over $sm(x)$ instead of $f(x)$ with the constraint that $sm(x)$ is able to faithfully reproduce the behavior of $f(x)$ throughout the optimization process. Consider the cost

function:

$$\begin{aligned} &\text{minimize} \quad f(x), \\ &\text{subject to} \quad x \in B \equiv \{x | a \leq x \leq b\}, \end{aligned}$$

If the cost function shows any of these behaviors: evaluation of $f(x)$ is very expensive, evaluation of derivative is impossible or costly, evaluation of $f(x)$ is not possible by the x returned by optimization algorithm (like in case where, to evaluate $f(x)$ ODE needs to be solved), or evaluation of $f(x)$ returns few correct digits, then in any of these cases surrogate modeling framework can prove useful for optimization of cost function [6].

Surrogate models are of two types: physical surrogate models and functional surrogate models. Physical surrogate models are built from physical or numerical simplification of the true functions. Physical surrogate models are based on some knowledge of the physical system or phenomena being modeled. So, physical surrogate models are problem-dependent. However, there are some rigorous methods that have been developed to build physical surrogate models, such as the space mapping [4] method, which uses the gradient information of the true function $f(x)$ to build a simplified surrogate model.

Since all the kinetic models follow from a fixed set of physical laws, building a physical surrogate model holds significant potential. We are exploring the options of space mapping method for building surrogate models.

Functional Surrogate model Functional surrogate models are algebraic representations of the true problem functions. In general, functional models are based on the follow-

ing components: a class of basis functions, a procedure for sampling the true functions, a regression or fitting criteria, and some deterministic or mathematical technique to combine them all. It is important to note that functional surrogate models are mathematical in nature different from true, original functions. However, the coefficients of the functional model are tuned to reproduce the behavior of the true function $f(x)$. This has the significant advantage that functional surrogate models are generic and empirical and not restricted to certain classes of problems as physical surrogate models are. Functional surrogate models are strongly dependent on samples of the true function.

Among many available methods for building functional surrogate models: radial basis functions and Kriging models [91] are popular choices. We have used the DACE toolbox [106] to build functional surrogate models based on the Kriging approximation. For a detail discussion on surrogate models readers are directed to the book by Conn *et al.* [12].

In this section we briefly discussed the possible problems in parameter identification of the kinetic model and possible solutions. We are actively pursuing the idea to build a rigorous surrogate modeling framework for the parameter identification problem for kinetic models.

Chapter 5

Model of Pyruvate Recycling Pathways

In this chapter we describe our model of pyruvate recycling in β-cells, and use the model to draw insights into system behaviour.

5.1 Model Description

The ordinary differential equation (ODE)-based model describes the kinetics of 30 enzyme-catalyzed reactions in β-cell metabolism (Figure 5.1). The model state variables are the dynamically independent concentrations of 24 metabolite species in two compartments—mitochondrial matrix and the cytosol (the mitochondrial inter-membrane space is neglected). One additional species concentration is determined through conservation. The concentrations of seventeen additional species are held constant as model parameters. Details of the model kinetics and parameter values are included in the Appendix A.1.

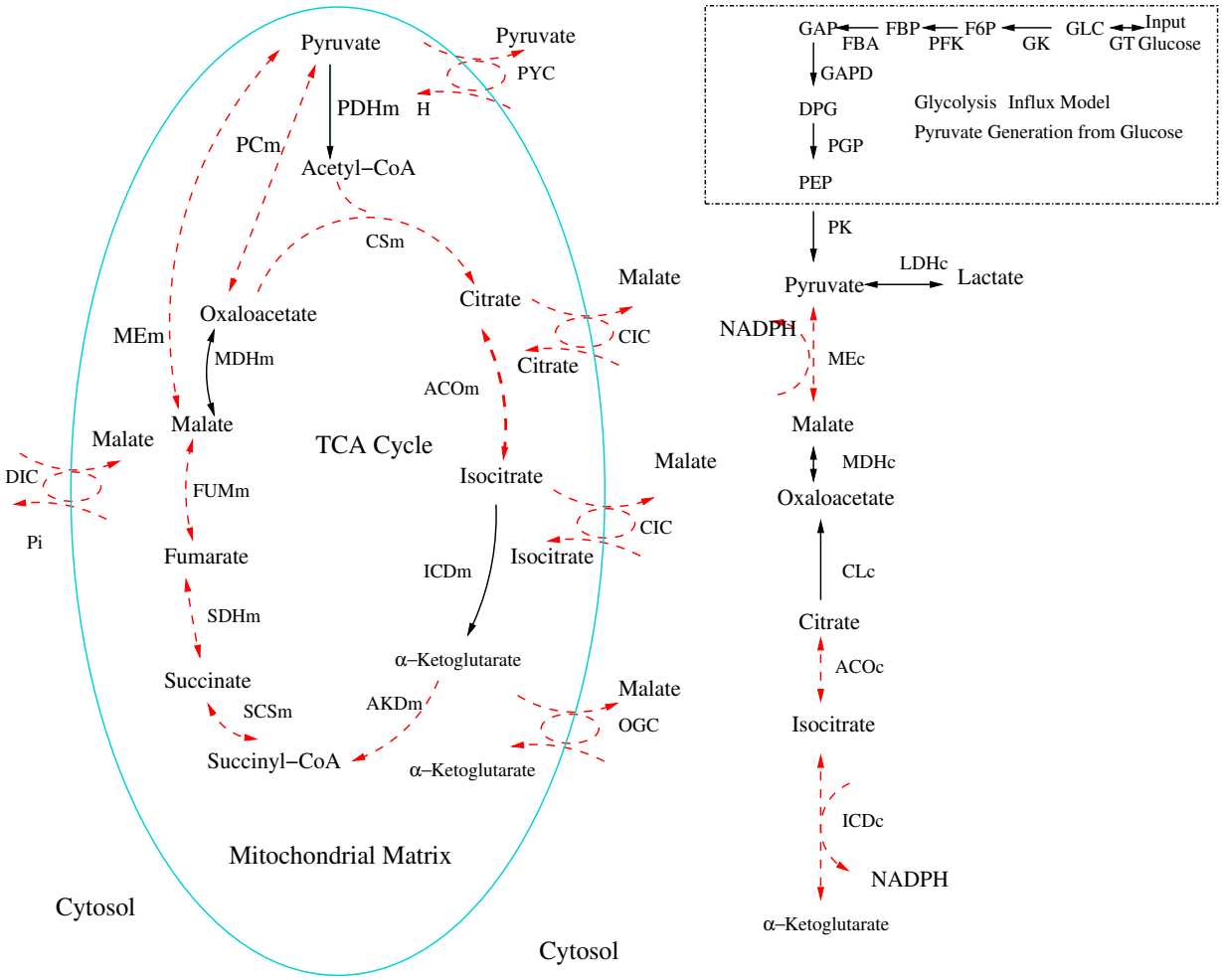

Figure 5.1: **Pyruvate recycling in β-cells**. Pyruvate is converted to oxaloacetate by PCm. Oxaloacetate is converted to citrate and isocitrate, both of which are transported between the cytosol and the mitochondrial matrix. Citrate is converted into isocitrate by ACOc. Isocitrate can be converted to α-ketoglutarate (αKG) via ICDc. Isocitrate is then converted into αKG through ICDc then αKG may enter the mitochondria for conversion to malate by TCA cycle enzymes, and subsequent conversion to pyruvate by MEm or MEc, thus completing the pyruvate cycle. Abbreviations. Influx model: GLC:Glucose, F6P:Fructose-6-phosphate, FBP:Fructose-1,6-bisphosphate, GAP:Glyceraldehyde 3-phosphate, DPG:1,3-bisphospho-D-glycerate, PEP:Phosphenol Pyruvate, GT:Glucose Transporter, GK:Glucokinase, PFK:6-phosphofructokinase, FBA:fructose-bisphosphate aldolase, GAPD:glyceraldehyde 3-phosphate dehydrogenase, PGP: bisphosphoglycerate phosphatase, PK:Pyruvate kinase, LDHc:Lactate dehydrogenase, ACOm:Aconitase Mitochondrial, ACOc:Aconitase Cytosolic, CIC:Citrate Carrier, DIC:Dicarboxyrate Carrier, CLc:Citrate Lyase Cytosolic, CSm:Citrate Synthase, FMm:Fumarase, IDHm:Isocitrate Dehydrogenase Mitochondrial, IDHc:Isocitrate Dehydrogenase (NADP+) Cytosolic, MDHm: Malate Dehydrogenase Mitochondrial MDHc: Malate Dehydrogenase Cytosolic, OGC:Oxoglutarate Carrier, PCm:Pyruvate Carboxylase PDCm:Pyruvate Dehydrogenase Complex, PYC:Pyruvate Carrier, AKDm:α-Ketoglutarate Dehydrogenase, SCS:Succinyl-CoA synthetase, SDHm:Succinate Dehydrogenase, MEm:Malic Enzyme Mitochondrial, MEc:Malic Enzyme Cytosolic.

The network input is extra-cellular glucose, which enters the cytosol via the high-capacity, low-affinity glucose transporter-2 (GLUT2). This transport step is modeled as previously reported by Sweet and Matschinsky [108]. Glucose is converted to pyruvate by the six-step glycolysis pathway [47]. The kinetics of all glycolytic reactions were drawn from the SABIO-RK database [112], with some adjustments (details in the Appendix A.1). The glycolytic pathway is treated as a fixed influx module, and is not included in the subsequent model analysis (Section 5.3). The end-product of glycolysis, cytosolic pyruvate, is either converted to lactate (by lactate dehydrogenase (LDH)) or transported into the mitochondrial matrix. (The former process carries much less flux than the latter; LDH activity is weak in β-cells [110].) The TCA cycle operates within the mitochondrial matrix. All components of the three pyruvate recycling processes—the pyruvate/malate cycle, the pyruvate/citrate cycle, and the pyruvate/isocitrate cycle—are included in the model.

Simulation Method The system was simulated using mass conservation laws for each of the dynamically independent species. The reaction kinetics and model equations are included in the Appendix A.1.4. Simulations were carried out in MATLAB (function ode15s). Models steady-state concentrations is confirmed by the application of Trust-region-dogleg method to the long-time simulation outputs (MATLAB function fsolve). The details of simulations are provided in Appendix A.2.1.

Parameterization Approach The reaction kinetics, as well as the bulk of the parameters, were derived from the previous models of Yugi and Tomita [116] and Westermark *et al.* [110]. After formulating the model, we performed a preliminary global sensitivity

analysis to identify parameters that could be adjusted to provide better fits to recent data. We selected parameters whose values are not well-characterized and that had a significant contribution to the overall sensitivity, but did not impact the crucial measures of (i) the ratio of metabolic to cytosolic malice enzyme activity, and (ii) the ratio of pyruvate dehydrogenase to pyruvate carboxylase activity. We arrived at a set of 34 model parameters to be fit. Fixing the values of the other 89 parameters as found in the literature, we calibrated the values of the 34 adjustable parameters by fitting to the experimental observations of Ronnebaum *et al.* [88]. That paper provided 32 steady state metabolite concentration measurements (8 species in 4 conditions) against which to fit the model. This data will be referred to as the training set. Parameter values were estimated using the simplexSB and simannealSB algorithm provided by SBTOOLBOX2 software package [97]. The parameters values were identified by minimizing least-squares error, weighted by variability in the data. Details of the calibration routine, including the bounds used for the parameter search, are presented in the Appendix A.2.2.

Having found a best-fit to the training set, we then verified the model by comparing model predictions against a range of experimental results on β-cells metabolism [49, 50, 63, 45], as described in the next section. None of this test set data was used for fitting.

5.2 Model Validation

5.2.1 Model Training

The model was parameterized against a training set provided by the experiments (gene knock-down via short interfering RNA (siRNA)) in Ronnebaum *et.al.* [88], in which siRNAs specific for the mRNA of the ICDc enzyme were used to reduce the activity of ICDc. To simulate the effect of the siRNA treatment, we reduced the V_{max} parameter of ICDc by the measured decrease in enzyme activity (39.1%). Ronnebaum *et al.* collected steady-state metabolite measurements of eight metabolites in each of four cases: control and knock-down at low glucose (3mM) and high glucose (12mM). Simulating these cases to steady state, we calibrated the model by minimizing a least-squares measure of error. The best-fit model behavior is shown in Figure 5.2. The best-fit model parameters are reported in the Appendix A.3, along with the values of the 89 parameters that were taken directly from the literature.

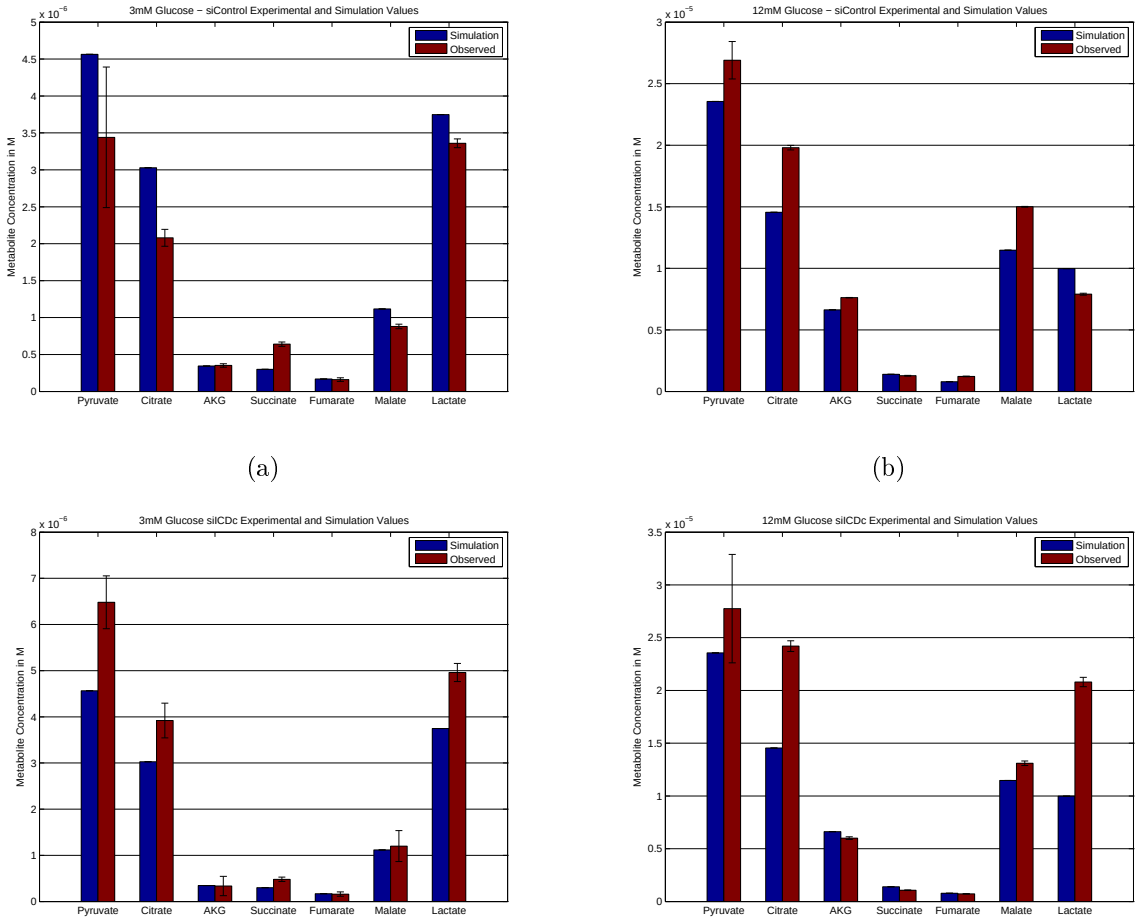

Figure 5.2: Best-fit model fitting to data from Ronnebaum *et.al.* experiments. Panel A. Low glucose, control. Panel B. High glucose, control. Panel C. Low glucose, ICDc knock-down. Panel D. High glucose, ICDc knockdown.

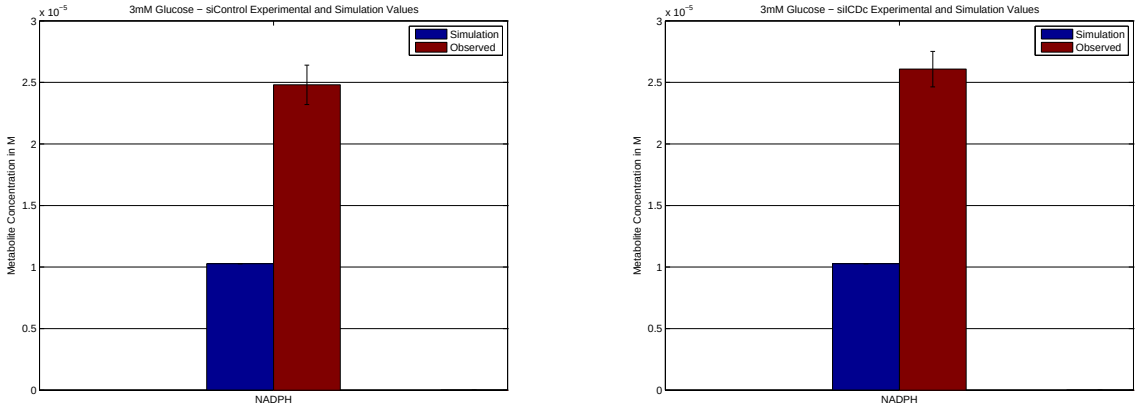

(a)

(b)

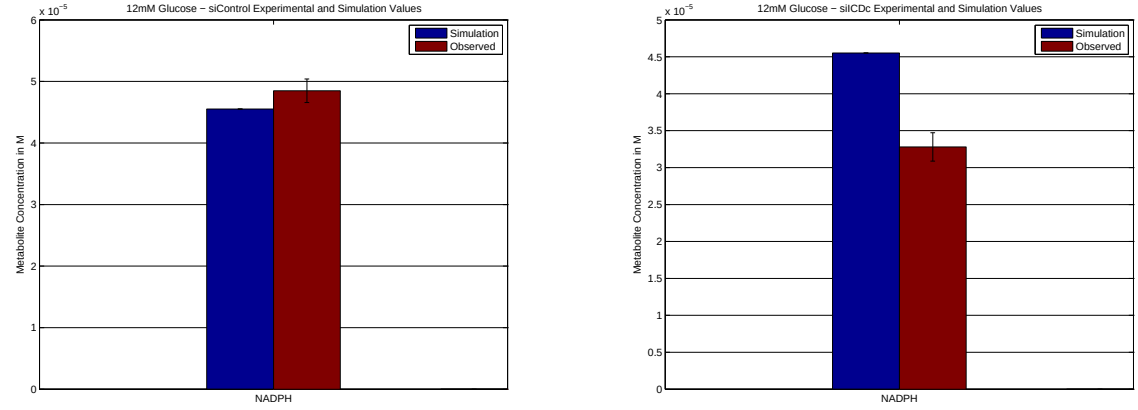

(c)

(d)

Figure 5.3: Simulation Comparison with Observed values for NADPH Ronnebaum *et.al.* data. 5.3a 3mM glucose input control case. 5.3b 3mM glucose input knock down case. 5.3c 12mM glucose input control case. 5.3d 12mM glucose input Knock down case.

5.2.2 Model Testing

To validate the model we compared model predictions against a test data set gathered from the literature. (None of this test-set data was used in parameter fitting.)

Lactate Dehydrogenase Activity We found that the model corroborates the experimental observation by Sekine *et al.* [101] that, in comparison with other cell types, β-cells exhibit significantly reduced lactate dehydrogenase (LDH) activity. In the model network, glucose-derived pyruvate is either converted to lactate by LDH or is transported into the mitochondria by the pyruvate transporter (PYC). We compared the flux through these reactions over a wide range of glucose levels (2.5mM to 22mM) and found that LDH exhibits between 2-4% of the PYC flux.

Malic Enzyme Activity It has been shown that in β-cells, the cytosolic form of malic enzyme (MEc) contributes approximately 90% of the total malic enzyme activity in the cell, at glucose concentrations ranging from 3mM to 20mM [32]. Simulations of the model predict that roughly 95% of malic enzyme flux is carried by MEc, for glucose levels ranging between 2.5mM and 22mM.

Pyruvate Carboxylase Activity Radio-isotopic experiments have revealed that in β-cells approximately 40% of glucose-derived pyruvate enters the TCA cycle via PC-catalyzed conversion to OAA, with the remainder metabolized to acetyl-CoA via pyruvate dehydrogenase (PDH) [57, 100, 67, 65]. The model predicts that over the range of 12-20mM glucose, approximately 40% of pyruvate enters the TCA cycle through pyruvate carboxylase. This percentage increases to above 50% at low glucose (3mM).

Pyruvate Recycling Using a ^{13}C NMR isotopomer method, Lu *et al.* [63] measured the rate of pyruvate recycling, which they defined as the ratio of PC flux to the overall

TCA cycle flux. This study was carried out in a set of clonal cell lines derived from rat insulinoma INS-1 cell lines; these cells exhibit a broad range of GSIS sensitivity and are thus useful for investigating the amplifying pathway response. They found that the anapleurotic flux catalyzed by PCm is correlated with GSIS, while pyruvate dehydrogenase (PDHm)-mediated entry of pyruvate into the TCA cycle is not significantly affected by changes in glucose abundance. Their results are shown in figure 5.4a, along with the model predictions. While the model underestimates the recycling rate, it correctly captures the increase in recycling rate with glucose availability. The experiments of Lu *et al.* revealed that the acetyl-CoA does not increase linearly with glucose availability, but saturates by about 13.5mM glucose concentration. Figure 5.4b shows our model predictions of this saturation trend.

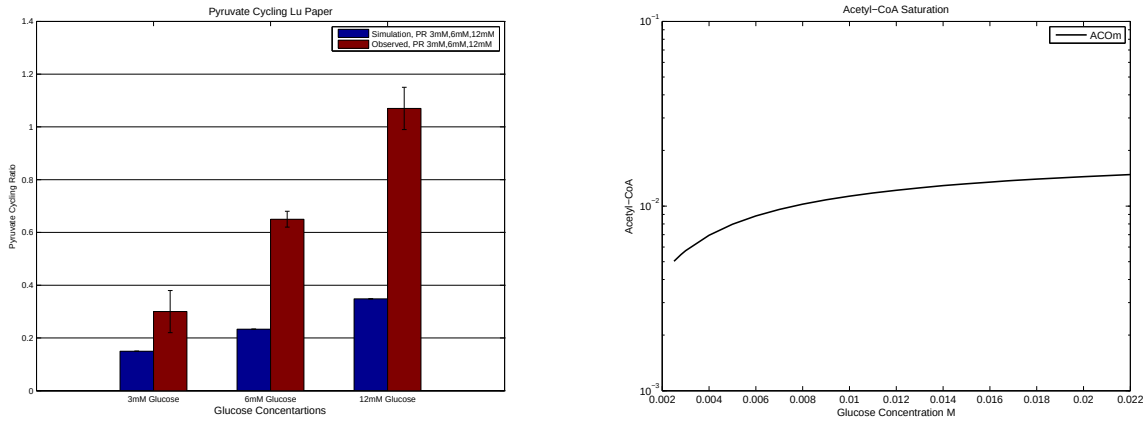

(a) (b)

Figure 5.4: 5.4a Simulation result of pyruvate recycling at different glucose level. The comparison is done against glucose responsive cell lines 5.4b Percentage increase in Acetyl-CoA as glucose concentration is increased showing saturation.

Ronnebaum *et al.* made measurements of the pyruvate recycling rate in wild-type and ICDc knock-down strains. We calculated the pyruvate recycling ratio from model simulation. We found that at 3mM glucose for the control case the ratio is .3483 while for ICDc knock down it is .1498 (at 12mM glucose simulation there is little variation in the ratio; control case is .3485 and ICDc knock down is .1499). This data shows the effect of the ICDc knock-down on pyruvate recycling.

ATP Citrate Lyase Knockdown Joseph *et al.* [52] conducted siRNA-mediated suppression of citrate lyase (CL). They estimated that CL activity was reduced by 75±4%; this resulted in a $52 \pm 7\%$ reduction in cytosolic oxaloacetate, and no significant impact on the NADP:NADPH ratio (steady state, at 16.7mM glucose). We simulated this experiment by reducing the V_{max} value for CL by 75%. At steady state, for 16.7mM glucose, the resulting change in the NADP:NADPH ratio is .01%; the cytosolic oxaloacetate concentration drops by 62.8%. (The model predicts a more modest drop in OAA_C at lower glucose levels, e.g. 54.4% at 3mM).

Pyruvate Carboxylase Knock Down Jensen *et al.* [46] conducted an siRNA-mediated knock-down of pyruvate carboxylase. In their knock-down strain, PC activity was reduced by 65%, but there was a minimal effect on the glucose-dependence of the NADPH:NADP ratio (Figure 5.5c). The model predictions confirm that a 65% decrease in PC activity (i.e. in the corresponding V_{max} parameter) has a negligible effect on this glucose-dependence.

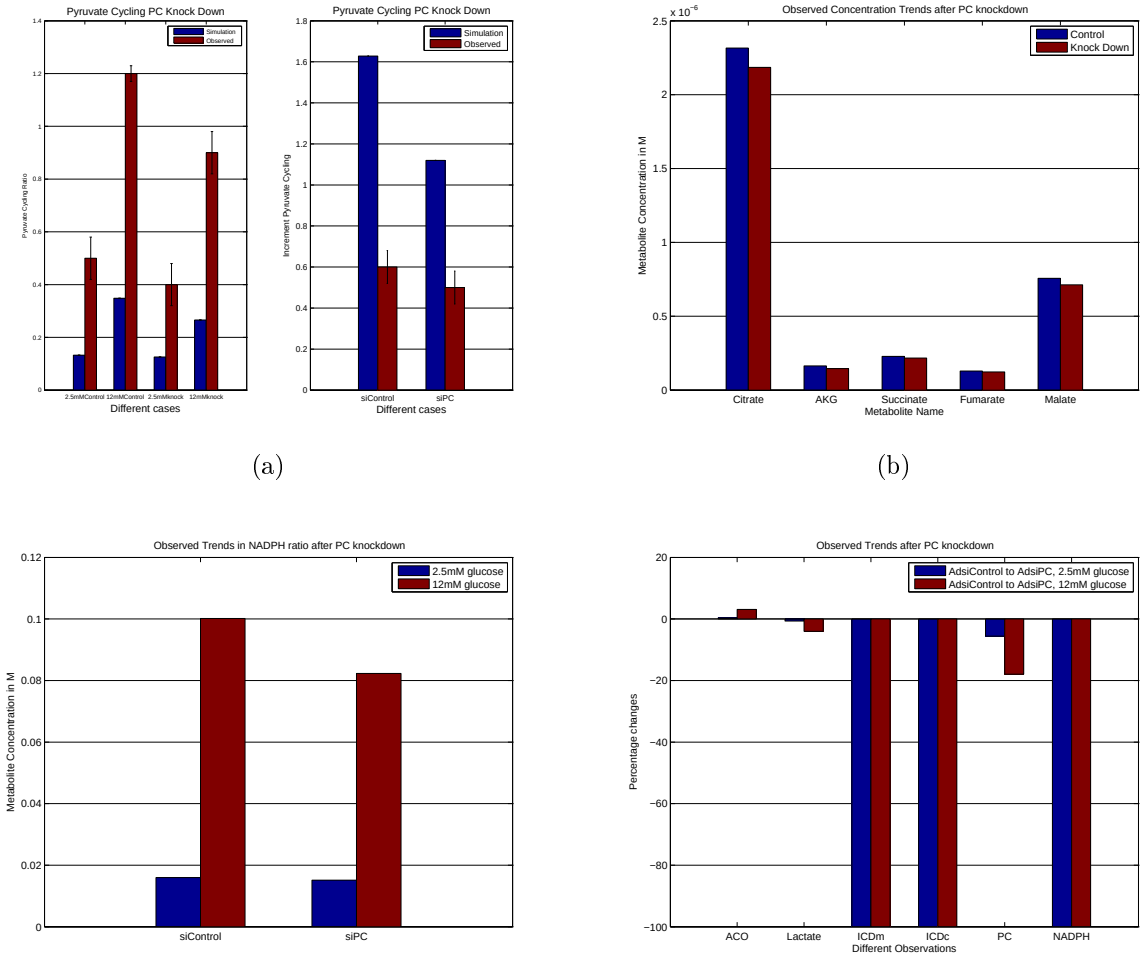

Figure 5.5: Low Glucose 2.5mM, High Glucose 12mM 5.5a Comparison of Pyruvate Recycling for the case of PC knock down. 5.5b Concentration trends of metabolites for PC knock down. 5.5c No effect on NADPH:NADP ratio due to PC knock down. 5.5d Comparison between simulation and effect of PC knock down on metabolites and fluxes.

Jensen *et al.* also analyzed the effect of their PC knockdown on the concentrations of TCA cycle intermediates. In the control case, they found that the concentrations of succinate, malate, α-KG and citrate increased 2-30 fold when glucose was increased from

2.5mM to 12mM (Figure 5.5b). When PC activity was suppressed no changes were observed in the glucose-response of succinate, fumarate and malate; however, the glucose-response of α-KG was significantly reduced (Figure 5.5b). The model successfully predicts these effects (Figure 5.5b, 5.5d). Figure 5.5d shows that the model captures the effect of PC suppression on acetyl-CoA and lactate that is increment in there concentration when PC is suppressed compared to control case.

Malic Enzyme Cytosolic Knock Down To investigate the role of the pyruvate/malate cycle, Ronnebaum *et al.* [89] conducted siRNA-mediate knock-down experiment of cytosolic and mitochondrial malic enzyme. They found that knock-downs of either enzymes by 75% had no effect on the pyruvate recycling rate at either 2.5mM or 12mM glucose. Figure5.6a shows the data along with model prediction for cytosolic malic enzyme, the result for mitochondrial malic enzyme is similar. Actually there is nothing to compare relevant to model and all the study is done using MEc knock down. However, their experiments showed that the NADPH concentration was reduced by the MEc knock-down . We simulated these experiments by reducing the V_{max} of MEc by 75%. The simulation results are shown in Figure 5.6.

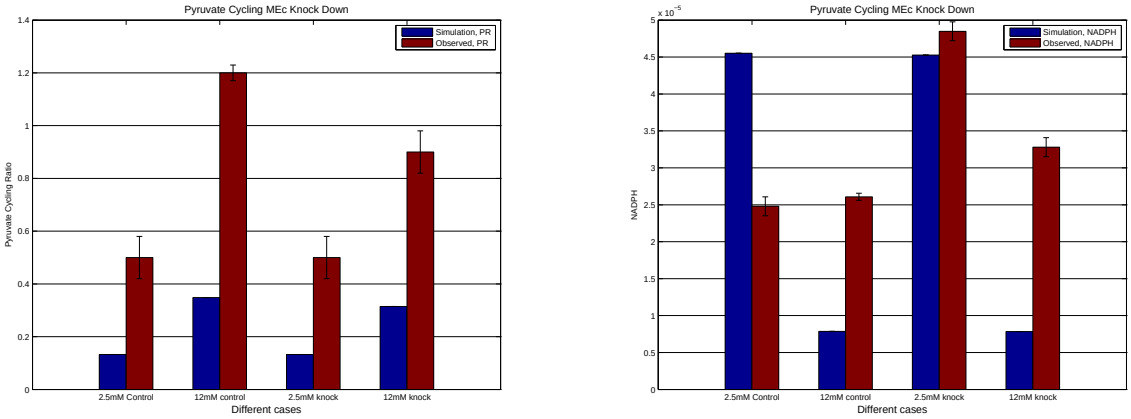

(a) (b)

Figure 5.6: Low Glucose 2.5mM, High Glucose 12 mM. 5.6a Effect of MEc knock down on Pyruvate Recycling. 5.6b Effect of MEc knock down on NADPH concentration.

Aryl Hydrocarbon Knock Down Pillai *et al.* [85] investigated the metabolic effect of an siRNA-mediated knock-down of the transcription factor aryl hydrocarbon receptor nuclear translocator (ARNT)/hypoxia-inducible factor (HIF)-1β, which regulates expression of ICDc, MEc, CL, PC, AKD, CIC, and DIC. In their experiments, they found that a knock-down of ARNT down-regulates glycolysis, anaplerosis and glucose-induced fatty acid production, all of which are known to be important events in GSIS. Pillai *et al.* measured the steady-state concentrations of several TCA intermediates at both low and high glucose levels, in the control and knock-down cases (Figure 5.7). The control cases are directly comparable with the control cases from our training data (from Ronnebaum *et al.* [88]).

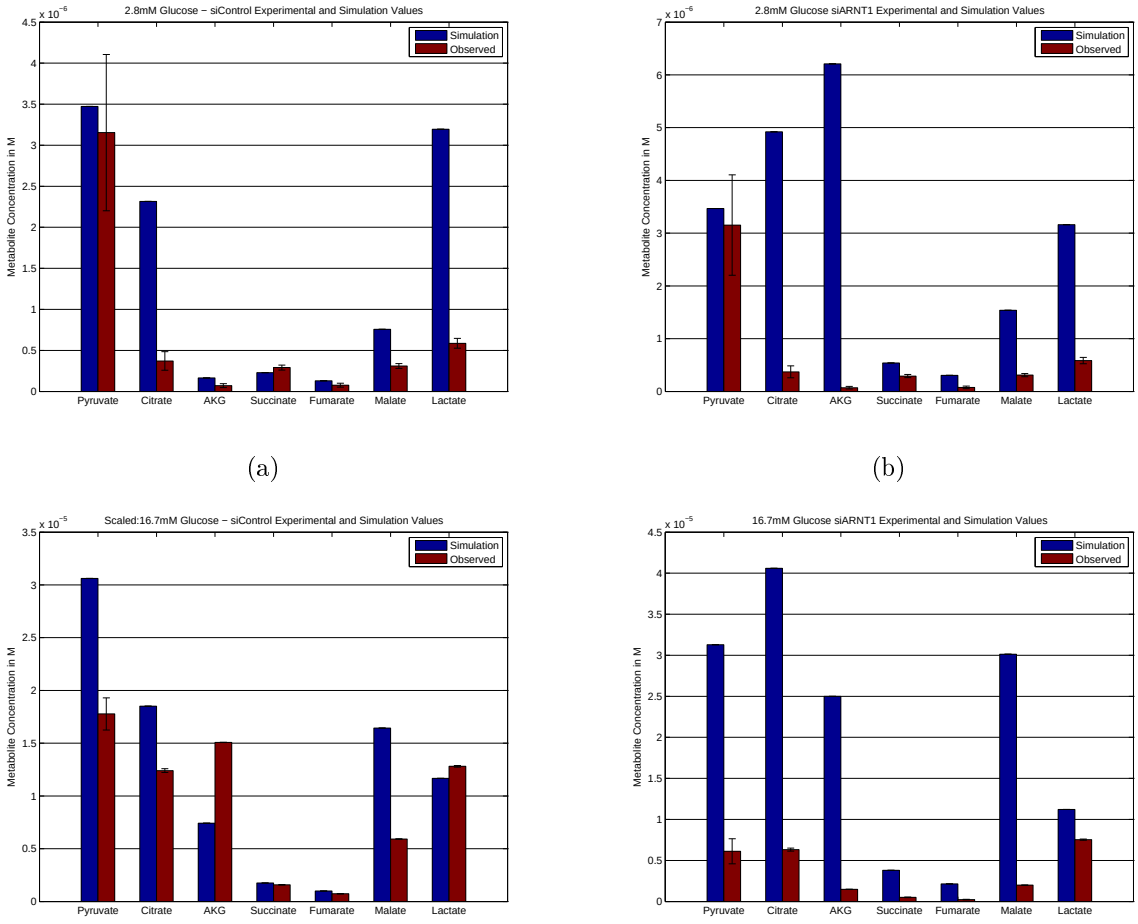

Figure 5.7: Simulation Comparison with Observed values for Pillai *et.al.* data (*not scaled*). 5.7a The model simulation is compared to 2.8mM glucose input with the Pillai *et.al.* data for the control case. 5.7b The model simulation is compared to 16.7mM glucose input with the Pillai *et.al.* data for the control case. 5.7c The model simulation is compared to 2.8mM glucose input with the Ronnebaum *et.al.* data for ARNT1 Knock down case. 5.7d The model simulation is compared to 16.7mM glucose input with the Pillai *et.al.* data for ARNT1 Knock down case.

However, because these experiments were carried out in different conditions, the quantitative measurements are not entirely consistent. In order to arrive at a prediction that is

consistent with the training set, we introduced a set of scaling factors. The scaling factor is decided by scaling the Pillai *et al.* [85] low glucose control data to that of Ronnebaum *et al.* [88] low glucose control data. We added a correction factor by measuring the fold increase of metabolite in model simulation when glucose is raised from 2.8mM to 3mM and for high glucose 12mM to 16.7mM since the Pillai *et al.* [85] experiments are done at this glucose concentration. Pillai *et al.* Pillai *et al.* report that their siRNA results in the following decreases in enzyme activity: ICDc: 89.29%, MEc:54.76%, CLc:54.17%, PCm:46.43%, AKDm:63.10%, CIC:94.05% and DIC:60.71%. Simulation of the model with the corresponding decreases in V_{max} values are compared with the experimental findings in Figure 5.7.

Model Trends of NADPH concentration profile In addition to the measurements of NADPH concentration reproduced in figure 5.3, Ronnebaum *et al.* [88] also made measurements of the NADPH/NADP ratio at a range of glucose concentrations. The model accurately predicts these findings, as follows. Ronnebaum *et al.* found that the NADPH/NADP ratio increases by 33.33% when the glucose concentration is increased from 3mM to 4mM; the model simulation shows an increase of 49.00%. The experiments showed that the ratio increased 35.71% when glucose was increased from 4mM to 6mM; simulation predicts a 64.25% increase. Finally, Ronnebaum *et al.* report a 50% increase in the NADPH/NADP ratio when glucose was increased from 6mM to 12mM; simulation of this comparison predicts a 95.12% increase in the ratio. When compared to siICDc knock down we found that NADPH/NADP ratio decreases by approximately 42% at 3mM while simulation shows decrease of .0013%, similarly at 12mM glucose observed decrease is 17.11% while simulation

is .00032% (Figure 5.8a).

Table 5.1: NADPH percentage increase in concentration when glucose concentration is raised

Glucose increment (mM)	Observed	Simulation
3 to 4	3.33e+01	4.90e+01
4 to 6	3.57e+01	6.42e+01
6 to 12	5.00e+01	9.51e+01
3 to 12	1.25e+02	5.80e+02

Sener *et.al.* [103] hypothesized that the NADPH:NADP ratio can be inferred from the pyruvate:malate ratio or the citrate:α-KG ratio. Our model prediction of this result, which is consistent with this prediction, is shown in figure 5.8a.

Finally, Hedeskov *et.al.* [33] found that the NADPH/NADP ratio increases 125% when glucose is increased from 3mM to 20mM. The model predicts an increase of 71.461%.

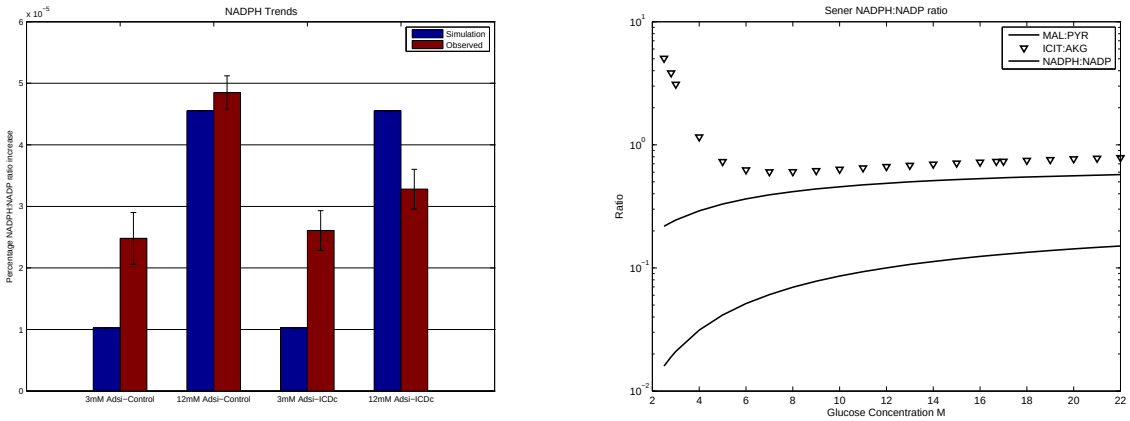

(a) (b)

Figure 5.8: 5.8a Comparison between simulation and observed percentage increase in NADPH:NADP ratio. 5.8b Comparison of NADPH:NADP ratio with PYR: MAL and ICIT:AKG ratio

5.3 Model Analysis

To identify important control points in the pathway we performed local sensitivity and global sensitivity analysis. These analyses were carried out as described in sections 3.3, 3.4, 4.3.

Properties of Sensitivity Measure Variance-based GSA methods allow us to calculate both first-order and total-effect sensitivity rankings. First-order sensitivity reflects the effect of variations in single parameters on the model output, whereas total-effect sensitivity describes the dependence of the model output on the parameters in combination. Comparisons between the first-order and total-effect sensitivity predictions can provide insight into interactions among parameters.

For Sobol's method we only report the total effect measure, since the first order effect measures have many negative values. The design of Sobol's method allows to have negative values but comparison with eFAST is not possible as eFAST method design allows only positive values. The complete discussion on this topic can be found elsewhere [93]. Therefore, all the comparison between eFAST and Sobol's method will be done for total effect measure. To identify the interaction among parameters, eFAST rankings of first order effect and total effect measure will be used.

As a generic model output, we consider overall output as the sum of the squared deviation in all metabolite levels (See appendix for details A.2.3). Parameters that show the largest sensitivity rankings with respect to this over all measure (by either the first-order or total-effect approach) are the most influential in setting model behavior. The

overall sensitivity rankings provided by for Sobol's method and the eFAST method were found to be consistent (A.4.1).

5.3.1 Sensitivity Results

GSA Measure with respect to steady state cytosolic pyruvate and NADPH Figures 5.9 and 5.10 show the ranked sensitivities with respect to two model outputs: the steady-state concentration of cytosolic pyruvate and the steady-state NADPH concentration.

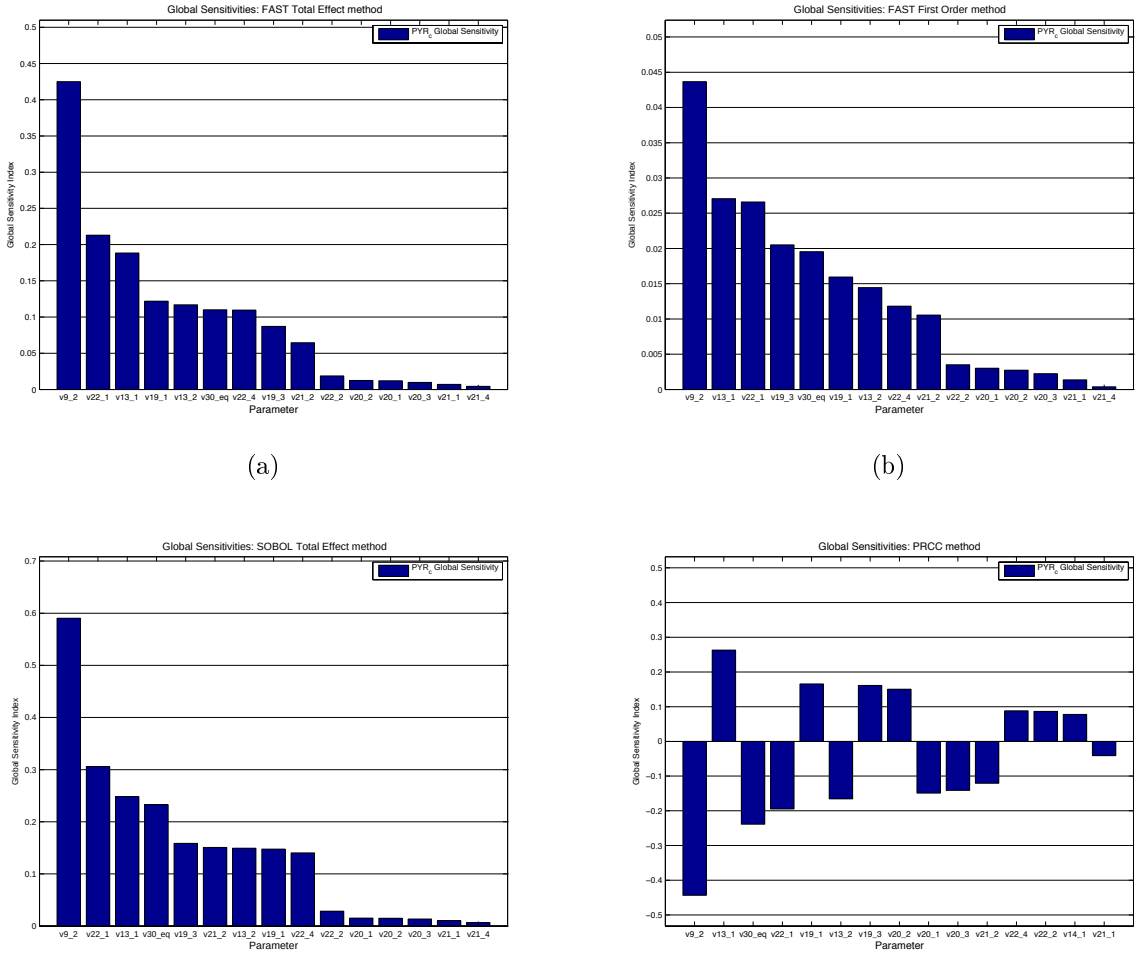

Figure 5.9: Global sensitivity ranking with respect to cytosolic pyruvate. Panel A eFAST total effect, Panel B eFAST first order, Panel C Sobol's total effect and Panel D PRCC. For parameters description refer to Tables A.8,A.7 and A.6

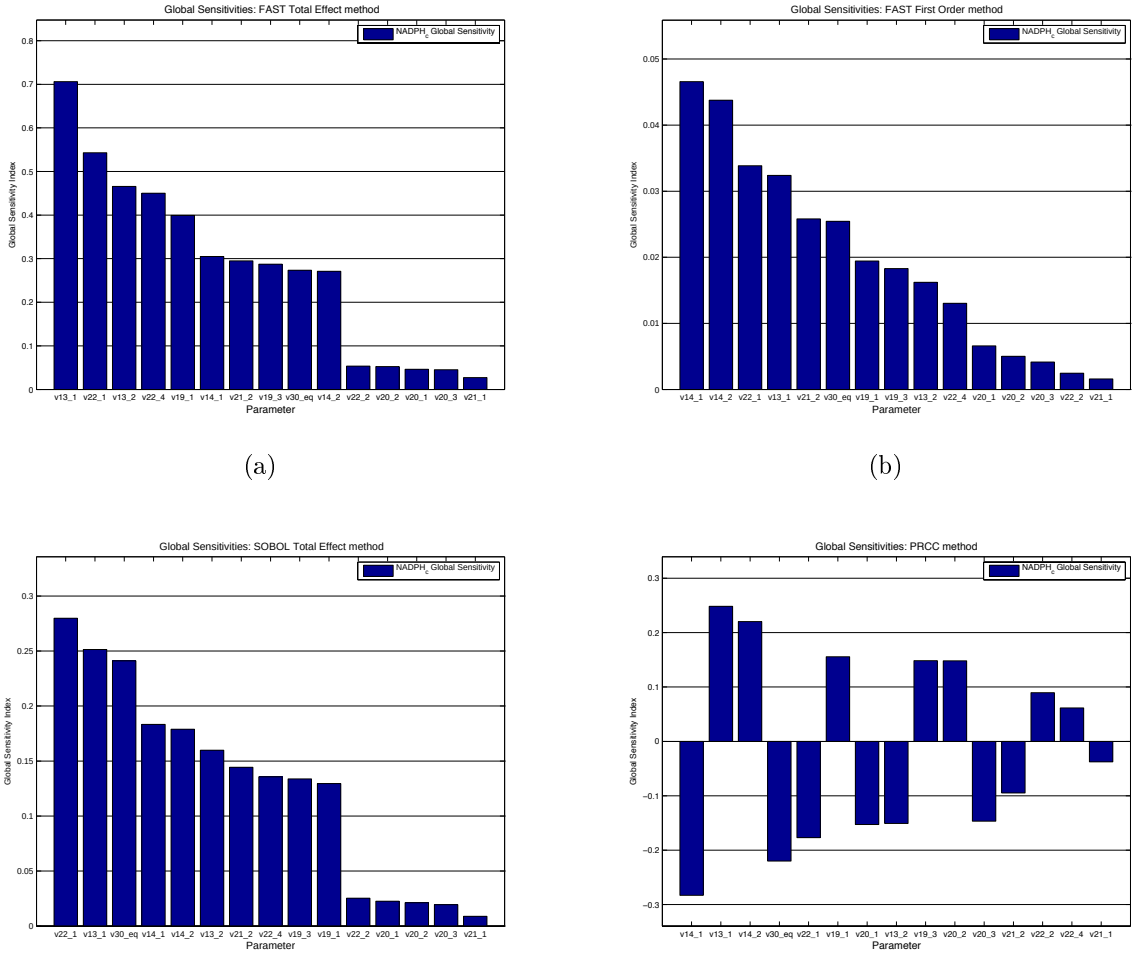

Figure 5.10: Global sensitivity ranking with respect to NADPH. Panel A eFAST total effect, Panel B eFAST first order, Panel C Sobol's total effect and Panel D PRCC. For parameters description refer to Tables A.8,A.7 and A.6

Local Sensitivity of cytosolic Pyruvate and NADPH The top ten sensitivity coefficients for cytosolic pyruvate and NADPH are shown in figure 5.11.

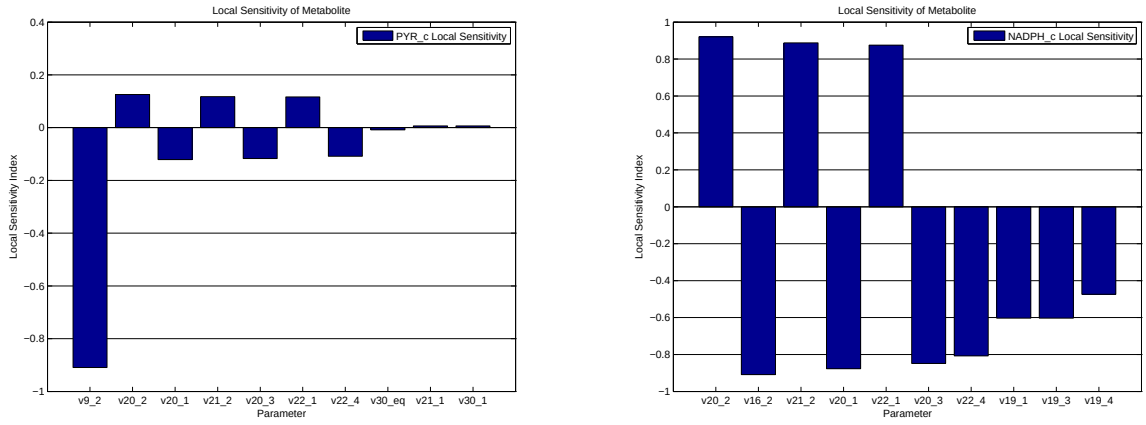

(a) (b)

Figure 5.11: Local sensitivity parameter ranking with respect to cytosolic pyruvate and NADPH. Panel A cytosolic pyruvate and Panel B NADPH. For parameters description refer to Tables A.8,A.7 and A.6

Effect of Pyruvate Carboxylase In order to understand the effect of perturbations in the concentration of pyruvate carboxylase (PC) on the pyruvate recycle pathways; the sensitivity measures have been reformulated such that ranking of fluxes are done based on the effect caused by the perturbation in PC. Figure 5.12 shows the degree of effect of PC V_{max} on different fluxes of the pathway. The ranking shows the five most affected fluxes and the five least affected fluxes.

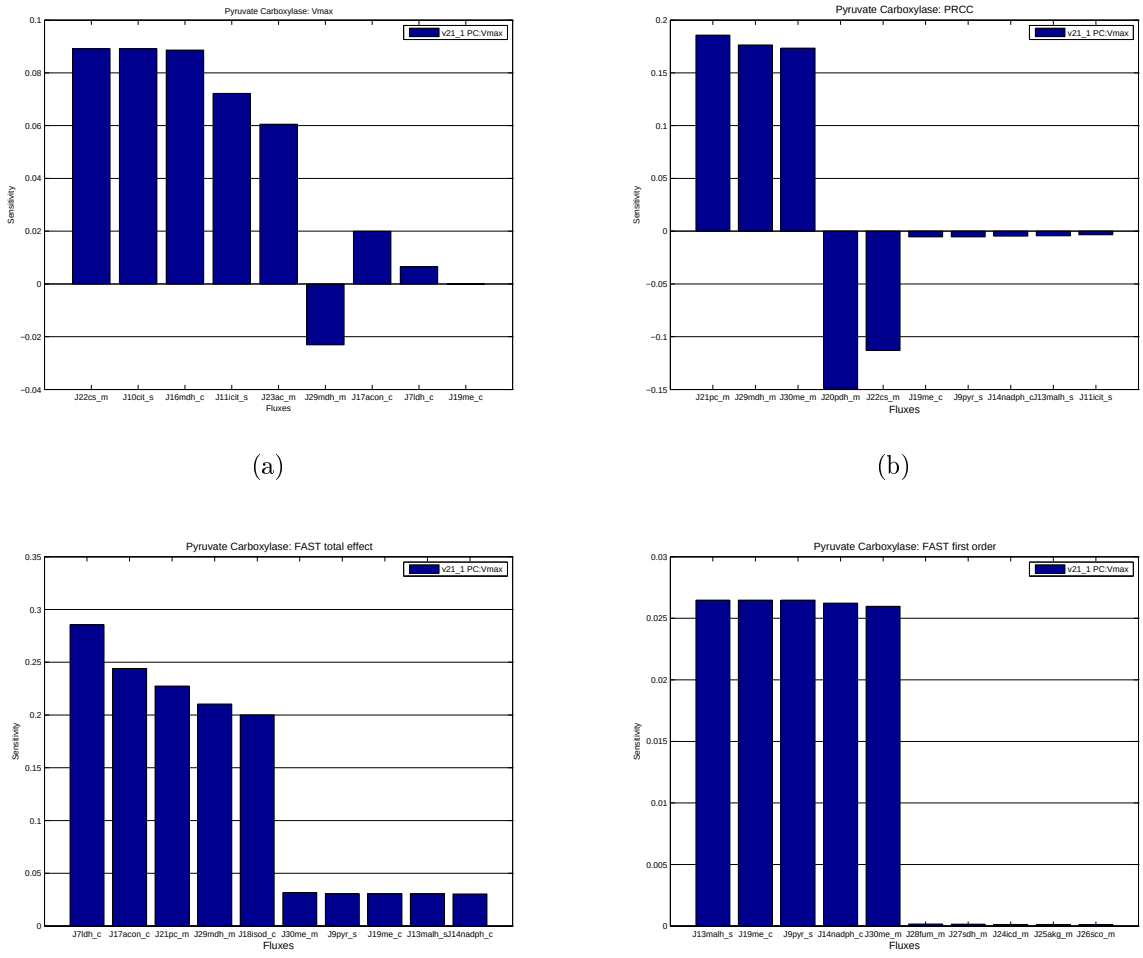

Figure 5.12: Effect of perturbation of PC, V_{max} on fluxes. Five most sensitive fluxes and five least sensitive fluxes are plotted . Panel A: local sensitivity. Panel B: PRCC ranking, Panel c: eFAST total effect and Panel D: eFAST first order. Sobol's total effect ranking is same as that of eFAST total effect ranking. For flux description refer to Tables A.8,A.7 and A.6

5.3.2 Analysis of Pathway Properties

Given the highly non-linear nature of the model, it is valuable to compare results of different sensitivity analyses in order to gain insight of model behavior. By comparing different GSA rankings and local sensitivity coefficients, we can identify important regulatory properties of the metabolic pathway.

Analyzing the first-order and second-order overall sensitivity rankings reveals that the V_{max} of LDH is the most influential parameter in the model. However, comparison between the first and second order rankings reveals that the V_{max}'s of fumarase, DIC and MDHm are the most significant in terms of interactions among all model parameters. These three enzymes are known to be important participants in pyruvate recycling pathways.

Next we consider the GSA sensitivity index for the model output of steady state cytosolic PYR concentration. The analysis of sensitivity of PYR reveals that the V_{max}'s of pyruvate transporter (PYC) and citrate synthase (CSm) are the most influential parameter (in terms of both first-order and total-effect). This implies that PYC and CSm has a dominant effect on the PYR concentration, regardless of perturbations to the rest of pathway. However, the comparison between first-order and total-effect sensitivities reflects important variance in ranking for other model parameters.

Considering the sensitivities with respect to both PYR and steady-state ICDc flux A.4.2 (the latter of which is the main produced of NADPH), we find that, consistent with the result that the V_{max} of CIC, DIC, PC and MEc have the most influence over parameter interactions, their first-order rankings are low, while the total effect rankings are high. These parameters are thus involved in parameter interactions that influence PYR and

ICDc flux.

We next consider the sensitivities with respect to the steady state NADPH level. First order sensitivity rankings indicate that the NADPH consumption rate (characterized by $v14\_1$ and $v14\_2$) is the most influential reaction; this is consistent with the model structure. Total sensitivity index ranks the V_{max} of CIC, DIC, PCm and MEc as, again, the most influential parameters.

It is interesting to note that the sensitivity rankings by local sensitivity analysis and GSA differ. These differences reveal the extent to which interactions among the parameters influence the model. For example, the V_{max} of ICDc enzyme ranked lower in the local analysis than in the global analysis (with respect to the ICDc flux). This implies that influence of the enzyme on ICDc flux is sensitive to the action of other parameters. However, in the local domain of parameter variation the V_{max} of ICDc enzyme is robust to external perturbations.

Comparison between overall measure sensitivity ranking of total-effect and first-order analyses reveals the highly interacting parameters. We found that the V_{max} of LDH, MDHc, MDHm and fumarase are the most highly interacting parameters of the model. These parameters are fairly non-influential individually but combined with other parameters exert significant influence on the model output.

Comparison of the local sensitivity rankings (5.12) of PC V_{max} perturbation with the respective global sensitivity rankings reveals that MEc and ICDc are robust to perturbations to PC, at least locally. This is consistent with the observation that the PC knockdown did not affected the NADPH:NADP ratio nor the pyruvate recycling ratio (section 2.5).

However, the global sensitivity results show active interactions. The PRCC ranking is different from eFAST total effect, implying loss of monotonicity of the input-output relations. Significantly, the difference in ranking of eFAST first-order effect and total-effect ranking imply strong impact of PC on the pyruvate fluxes due to interactions in the pathway. The impact on lactate dehydrogenase flux is maximum in the total effect ranking, providing a reason why lactate concentration goes high in the case of PC knock down (section 2.5). Comparison in these two rankings reveals that MEc, PYC, and DIC are robust to PC perturbation, providing a plausible reason why perturbations to PC do not impact the pyruvate recycling rate. Finally, we note that ICDc flux is not significantly impacted by the PC perturbation, explaining why NADPH concentrations are not sensitive to perturbations in PC level.

Based on our comparative analysis, sensitivity ranking of the model predicts that the V_{max}s of the pyruvate transporter (PYC) and citrate synthase (CSm) have the most significant impact on the pyruvate recycling rate. However, V_{max}s of PYC and CSm don't show interaction with other parameters in the pathway. Therefore, perturbations in V_{max}s of PYC and CSm might lead to loss of robustness of the pyruvate recycling rate. In contrast, the V_{max}s of transport enzymes citrate isocitrate carrier (CIC) and dicarboxylate carrier (DIC) exhibit maximum interaction among the remaining parameters of the model. This interaction can compensate perturbations in the other parameters. Knock-down of CIC and DIC has been shown to inhibit the glucose stimulated insulin secretion [51] (Section 2.5).

Taking these results together, the model predicts that combined perturbations (e.g, of both PYC and CIC, or CSm and DIC) can have the double-effect of a significant and

robust impact. The model suggest that these combined perturbations show the greatest promise as drug targets for modulation of the pyruvate recycling rate and NADPH:NADP ratio (and hence insulin secretion). This proposal could be addresses by experiments that address knock-downs of CSm, PYC, and combinations of PYC or CSm with CIC or DIC.

Chapter 6

Conclusion

In the current work we developed a detail model of pyruvate recycling and validated the model against known results regarding pyruvate recycling components. As described, the model confirms a number of relevant experimental findings. We successfully trained the model to the data from Ronnebaum *et al.* [88]. Next we successfully tested the model against observations of β-cells metabolism. Our model reproduces most of the properties of the GSIS investigation done by ^{13}C istopomer analysis and siRNA mediated knock down studies.

We performed the local and global sensitivity analysis to identify the important control points in the pathway. The analysis reveals that the pyruvate level is most influenced by the V_{max} of PYC and is robust to external perturbation. From within the pyruvate recycling pathways, the V_{max} of DIC, MEc and PCm have the most significant influence over the pyruvate level, indicating that these are important control points in the TCA

cycle anaplerosis. Similarly NADPH is influenced most by these parameters, establishing a further correlation between pyruvate recycling and GSIS.

The current model can serve as a template model for future addition of extra pathways and an integrated study of triggering signals and the amplifying pathway. By conducting global sensitivity analysis and local sensitivity analysis we identified the important control points in the pathway. The model predicts that study of combine gene knock down experiments of pyruvate transport, and citrate isocitrate carrier (CIC) or citrate synthase (CSm) and dicarboxylate carrier (DIC) can modulate the behavior of pyruvate recycling rate and hence will have significant impact on glucose induced insulin secretion.

We propose that any future extension of the model should be trained with additional data sets or produce better data fit than current model. The possible extensions of the model are discussed in next section.

6.1 Future Work

Biological modeling offers a powerful approach to decipher the complex regulatory mechanisms underlying basic biological processes. At the same time it raises interesting mathematical challenges for solving these problems.

Model Extensions In principle, the the β-cells action is very simple to explain: they sense the glucose levels in the blood and secrete insulin into the bloodstream to maintain glucose homeostasis. However, to carry out this simple task β-cells use complex regulatory mechanisms involving multiple levels of regulation. The experimental data for the

metabolism in the β-cells show distinct mechanisms of regulation. The model presented in this study is the first pyruvate recycling model to be corroborated against the experimental data in β-cells. However, the model was focused solely on the pyruvate recycling pathway. The immediate extension of the current model would be to incorporate the dynamics of ATP, ADP, and Ca^{2+} molecules and the regulatory effect on the enzymes. These molecules are known to be allosteric modifiers of many enzymes in the insulin pathway. This will allow the analysis of coupling between the ATP:ADP ratio and the NADPH:NADP ratio, and thus provide an avenue for addressing the correlation between the triggering and amplifying signals. Another valuable extension would be integration of detailed models of glycolysis, pyruvate recycle, and TCA cycle pathways. This will allow the study of citrate feedback on the glycolytic enzyme phosphofructokinase (PFK) (citrate is an inhibitor of PFK). Moreover, in the current model we did not consider the role of GTP as a potential metabolic coupling factor. In a future extension of the model, enzymes involved in GTP generation could be included.

Computational Challenges in Developing Large Scale Kinetic Models One of the challenges in developing large scale kinetic models is that simulation of the systems of differential equations and parameter identification are not trivial. Often ODE solvers fails to return solution for certain sets of parameters; similarly, optimization algorithms can fail to return satisfactory solutions. Recent mathematical developments might prove useful in addressing some of these challenges [9, 78, 44, 90, 74].

Solving kinetic model involves the use of ODE solvers. Most kinetic models are very stiff, with significant variations in the eigenvalues of the Jacobian matrix. This puts restric-

tion on the stability and efficiency of the stiff ODE solvers. Frequently, approximation of the Jacobian approximated via finite difference introduces truncation errors. Improvements in the accuracy of Jacobian approximation can thus lead to a significant improvement in the performance of ODE solvers. Symbolic differentiation is either not always available, or, due to the complexity of the rate expression, the expression returned through symbolic tools might have singularities. These limitations can be easily be improved by using automatic differentiation (AD) [9]. AD is underused in the kinetic modeling community. It holds significant potential for improvements in finding the solutions of ODE. Furthermore, AD can significantly improve the efficiency of the ODE solver in the Newton iterations (many stiff solvers involve Newton iteration which relies on finite difference approximation).

Recent improvements in interval arithmetic have led to a new class of ODE solvers which use interval arithmetic to solve the ODE [90, 74]. The advantage of using these solvers is that the uniqueness of solution is guaranteed [78, 44]. Testing interval arithmetic solvers in large scale kinetic model has yet to be done and holds significant potential.

One of the major challenges in developing large kinetic model is that all the kinetic data is not readily available. As a result parameters are empirically identified in order to successfully reproduce the experimental results. Since this scenario is unavoidable for large scale kinetic model, developing rigorous surrogate optimization frameworks will lead to a significant improvement in the identification process [6]. Attempts have been made to build simplified representations of ODE systems using spline approximation [117]. Using surrogate models to replace expensive function evaluations has been found to be a powerful approach for solving engineering problems, [4, 2, 6], but this approach has yet to be implemented for fitting kinetic models. Building a rigorous framework for kinetic model

parameter identification can lead to a better parameter estimation in the large scale kinetic models. Furthermore, kinetic models are built on specific physical laws. Therefore, finding a surrogate model based on these physical laws can guide the optimization algorithm in the correct direction to find unique global minima of objective function. Such, functional surrogate model will improve the parameter identification significantly. Following this procedure will ensure better prediction by the large kinetic models and will increase the accuracy of the modeling.

APPENDICES

Appendix A

Supplementary Material

A.1 Kinetic Mechanism Details

A.1.1 Abbreviation

Subscript c and m on state variables or on flux expression denotes cytoplasmic and mitochondrial compartments respectively.

Table A.1: Abbreviations for metabolites/Enzymes

Abbreviation	Substance name	Compound/EC number
GT	Glucose Transporter	
GK	Glucokinase	E.C.2.7.1.2
PFK	6-phosphofructokinase	E.C.2.7.1.11
FBA	fructose-bisphosphate aldolase	E.C.4.1.2.13
GAPD	glyceraldehyde 3-phosphate dehydrogenase	E.C.1.2.1.12
PGP	bisphosphoglycerate phosphatase	E.C.5.4.2.1/E.C.5.4.2.4
PK	Pyruvate kinase	E.C.2.7.1.40
LDH	Lactate dehydrogenase	E.C.1.1.1.27
ACO	Aconitase	EC4.2.1.3
CIC	Citrate Carrier	
DIC	Dicarboxylate Carrier	
CS	Citrate Synthase	EC4.1.3.7
FM	Fumarase	EC4.2.1.2
IDHm	Isocitrate Dehydrogenase Mitochondrial	EC1.1.1.41
IDHc	Isocitrate Dehydrogenase (NADP+) Cytosolic	EC1.1.1.42
MDH	Malate Dehydrogenase	EC1.1.1.37
OGC	Oxoglutarate Carrier	
PC	Pyruvate Carboxylase	EC6.4.1.1
PDC	Pyruvate Dehydrogenase Complex	EC1.2.4.1
PYC	Pyruvate Carrier	
AKD	α-Ketoglutarate Dehydrogenase	EC1.2.4.2 etc.
SCS	Succinyl-CoA synthetase	EC6.2.1.4
SDH	Succinate Dehydrogenase	EC1.3.5.1
MEm	Malic Enzyme Mitochondrial	EC1.1.1.39
MEc	Malic Enzyme Cytosolic	EC1.1.1.40
Pi	Phosphate	C00009
Q	Ubiquinone	C00399
QH2	Ubiquinol	C00390

Table A.2: Abbreviations for metabolites/Enzymes

Abbreviation	Substance name	Compound/EC number
GLC_c	Glucose	C00267
F6P_c	Fructose-6-phosphate	C00085
FBP_c	Fructose-1,6-bisphosphate	C00354
GAP_c	Glyceraldehyde 3-phosphate	C00118
DPG_c	1,3-bisphospho-D-glycerate	C00236
PEP_c	Phosphenol Pyruvate	C00074
LAC_c	Lactate	C00186
PYR_c	Pyruvate	C00022
MAL_c	Malate	C00149
CIT_c	Citrate	C00158
ICIT_c	Isocitrate	C00311
AKG_c	$\alpha-$keto-Glutarate	C00026
OAA_c	Oxaloacetate	C000036
NADPH_c	Nicotinamide Adenine Dinucleotide Phosphate	C00005
NADP_c	Nicotinamide Adenine Dinucleotide Phosphate (Oxidized)	C00006
PYR_m	Pyruvate	C00022
ACOA_m	Acetyl-CoA	C00024
CIT_m	Citrate	C00158
ICIT_m	Isocitrate	C00311
AKG_m	$\alpha-$keto-Glutarate	C00026
SCOA_m	Succinyl-CoA	C00091
SUC_m	Succinate	C00042
FUM_m	Fumarate	C00122
MAL_m	Malate	C00149
OAA_m	Oxaloacetate	C000036
CO2	Carbon Dioxide	C00011
ATP	Adenosine Triphosphate	C00002
ADP	Adenosine Diphosphate	C00008
NAD+	Nicotinamide Adenine Dinucleotides (Oxidized)	C00003
NADH	Nicotinamide Adenine Dinucleotides	C00004
CoA	Coenzyme A	C00010

A.1.2 Model Reactions

Table A.3: Model Reactions

Flux	Enzyme	Reaction
J0entry_s	GT	$\mathtt{InputGlucose} \rightleftharpoons \mathtt{GLC\_c}$
J1gk_c	GK	$\mathtt{GLC\_c} + \mathtt{ATP} \rightarrow \mathtt{F6P\_c} + \mathtt{ADP}$
J2pfk_c	PFK	$\mathtt{F6P} + \mathtt{ATP} \rightarrow \mathtt{FBP} + \mathtt{ADP}$
J3fba_c	FBA	$\mathtt{FBP} \rightleftharpoons \mathtt{2GAP}$
J4gapd_c	GAPD	$\mathtt{GAP} + \mathtt{NAD} \rightarrow \mathtt{DPG} + \mathtt{NADH}$
J5pgp_c	PGP	$\mathtt{DPG} + \mathtt{ADP} \rightleftharpoons \mathtt{PEP} + \mathtt{ATP}$
J6pk_c	PK	$\mathtt{PEP} + \mathtt{ADP} \rightarrow \mathtt{PYR} + \mathtt{ATP}$
J9pyr_s	PYC	$\mathtt{PYR\_c} + \mathtt{H\_m} \rightleftharpoons \mathtt{PYR\_m} + \mathtt{H\_c}$
J10cit_s	CIC	$\mathtt{CIT\_c} + \mathtt{MAL\_m} \rightleftharpoons \mathtt{CIT\_m} + \mathtt{MAL\_c}$
J11icit_s	CIC	$\mathtt{ICIT\_c} + \mathtt{MAL\_m} \rightleftharpoons \mathtt{ICIT\_m} + \mathtt{MAL\_c}$
J12akg_s	OGC	$\mathtt{AKG\_c} + \mathtt{MAL\_m} \rightleftharpoons \mathtt{AKG\_m} + \mathtt{MAL\_c}$
J13malh_s	DIC	$\mathtt{MAL\_c} + \mathtt{Pi\_m} \rightleftharpoons \mathtt{MAL\_m} + \mathtt{Pi\_c}$
J7ldh_c	LDH	$\mathtt{PYR\_c} \rightleftharpoons \mathtt{LAC\_c}$
J14nad_c		$\mathtt{NADPH\_c} \rightarrow \phi$
J15citl_c	CITL	$\mathtt{CIT\_c} \rightarrow \mathtt{OXA\_c}$
J16mdh_c	MDH	$\mathtt{MAL\_c} + \mathtt{NAD} \rightleftharpoons \mathtt{OXA\_c} + \mathtt{NADH}$
J17acon_c	ACO	$\mathtt{CIT\_c} \rightleftharpoons \mathtt{ICIT\_c}$
J18isod_c	IDHb	$\mathtt{ICIT\_c} + \mathtt{NADP} \rightleftharpoons \mathtt{AKG\_c} + \mathtt{NADPH}$
J19me_c	MEb	$\mathtt{MAL\_c} + \mathtt{NADP} \rightleftharpoons \mathtt{PYR\_c} + \mathtt{NADPH}$
J20pdh_m	PDC	$\mathtt{PYR\_m} + \mathtt{NAD} + \mathtt{CoA} \rightarrow \mathtt{ACO\_m} + \mathtt{NADH} + \mathtt{CO_2}$
J21pc_m	PC	$\mathtt{PYR\_m} + \mathtt{ATP\_m} + \mathtt{CO_2} \rightleftharpoons \mathtt{OXA} + \mathtt{ADP} + \mathtt{Pi}$
J22cs_m	CS	$\mathtt{OXA\_m} + \mathtt{ACOA\_m} \rightarrow \mathtt{CIT\_m} + \mathtt{CoA}$
J23ac_m	ACO	$\mathtt{CIT\_m} \rightleftharpoons \mathtt{ICIT\_m}$
J24icd_m	IDHa	$\mathtt{ICIT\_m} + \mathtt{NAD} \rightarrow \mathtt{AKG\_m} + \mathtt{NADH}$
J25akg_m	OGDC	$\mathtt{AKG\_m} + \mathtt{NAD} + \mathtt{CoA} \rightarrow \mathtt{SCOA\_m} + \mathtt{NADH} + \mathtt{CO2}$
J26sco_m	SCS	$\mathtt{SCOA\_m} + \mathtt{GDP} + \mathtt{Pi} \rightleftharpoons \mathtt{SUC\_m} + \mathtt{CoA} + \mathtt{GTP}$
J27sdh_m	SDH	$\mathtt{SUC\_m} + \mathtt{Q} \rightleftharpoons \mathtt{FUM\_m} + \mathtt{QH_2}$
J28fum_m	FM	$\mathtt{FUM\_m} \rightleftharpoons \mathtt{MAL\_m}$
J29mdh_m	MDH	$\mathtt{MAL\_m} + \mathtt{NAD} \rightleftharpoons \mathtt{OXA\_m} + \mathtt{NADH}$
J30me_m	MEa	$\mathtt{MAL\_m} + \mathtt{NAD} \rightleftharpoons \mathtt{PYR\_m} + \mathtt{NADH}$

A.1.3 Species which are held at constant concentration

Table A.4: Species concentration which are held at constant value and constant Parameters

Species	Constant value
COA_m	3.0×10^{-3} M [114]
Q_m	9.5×10^{-4} M [114]
QH2_m	$4.1 \times 10{-}4$ M [114]
CO_2	3.0×10^{-6} M [114]
pH	8.0 [88]
NAD_m	2.0×10^{-4} M [110]
NADH_m	1.0×10^{-4} M [110]
NAD_c	5.0×10^{-5} M [34]
NADH_c	2.0×10^{-7} M [34]
ATP_c	5.0×10^{-3} M [114]
ADP_c	5.0×10^{-5} M [108]
Pi_c	1.0×10^{-3} M [108]
ATP_m	1.0×10^{-2} M [114]
ADP_m	5.0×10^{-3} M [114]
Pi_m	1.010^{-3} M [114]
inglc Input Glucose	varies from 2.5mM to 22mM
Vr	20.0 [110]
NADPtot	5.0×10^{-4} M [88]

A.1.4 Rate Expressions

Kinetic Expression Simplification The model is divided into two sub parts: (i) the glycolysis model, and (ii) TCA cycle model, including pyruvate recycling. The glycolysis model is treated as influx model for pyruvate recycling and is not included in the model analysis. The glycolysis model is built as six step pathway generating pyruvate as described

earlier in Jiang *et.al.* [47]. The kinetic mechanism and parameters are taken from SABIO-RK [112] Details are provided in Table A.5.

The TCA cycle model and pyruvate recycle enzyme kinetics (Tables A.6, A.7 and A.8) are adapted from Yugi and Tomita [116] and Westermark *et.al.* [110], with the exceptions of lactate dehydrogenase (adapted from Hoefnagel *et.al.* [40]), malic enzyme (mitochondrial and cytosolic), and pyruvate dehydrogenase for both of which we developed our own kinetics. Parameters for these kinetics were taken from Brenda database [96]. Furthermore, we refined the cytosolic isocitrate dehydrogenase kinetics by removing CO_2 from the kinetics and taking new parameters from the Brenda database [96].

Since the goal of the model was to understand the role of pyruvate recycling we held the concentrations of ions and some metabolites constant, thus simplifying some kinetic expressions. As an example of this procedure, consider the pyruvate transport rate expression of Yugi and Tomita [116]. The original model includes transport of hydrogen (as an antiporter); in our model the hydrogen concentration in both compartments is held fixed, so we reduced the expression by combining the constant concentration with the kinetic parameters of original expression, as follows. The original expression is

$$\frac{\texttt{[PYR\_c]}\cdot\texttt{[H\_m]}\cdot\texttt{v9\_mf}-\texttt{[H\_c]}\cdot\texttt{[PYR\_m]}\cdot\texttt{v9\_mr}}{1+\frac{\texttt{[PYR\_c]}}{\texttt{v9\_KiA}}+\frac{\texttt{[PYR\_m]}}{\texttt{v9\_KiB}}+\frac{\texttt{[H\_c]}}{\texttt{v9\_KiP}}+\frac{\texttt{[H\_m]}}{\texttt{v9\_KiQ}}+\frac{\texttt{[PYR\_c]}\cdot\texttt{[H\_m]}}{\texttt{v9\_KiA}\cdot\texttt{v9\_KiQ}}+\frac{\texttt{[PYR\_m]}\cdot\texttt{[H\_c]}}{\texttt{v9\_KiB}\cdot\texttt{v9\_KiP}}+\frac{\texttt{[PYR\_m]}\cdot\texttt{[H\_m]}}{\texttt{v9\_KiB}\cdot\texttt{v9\_KiQ}}+\frac{\texttt{[PYR\_c]}\cdot\texttt{[H\_c]}}{\texttt{v9\_KiA}\cdot\texttt{v9\_KiP}}}$$

Since [H_c] and [H_m] are constant we can combine the concentration values with kinetic parameters to give

$$[\mathtt{H\_m}] \cdot \mathtt{v9\_mf} = \mathtt{v9\_1}$$

$$[\mathtt{H\_c}] \cdot \mathtt{v9\_mr} = \mathtt{v9\_2}$$

similarly for the denominator we have

$\frac{[\mathtt{H\_c}]}{\mathtt{v9\_KiP}}$ $\frac{[\mathtt{H\_m}]}{\mathtt{v9\_KiQ}}$ are constant terms say this terms are temp0 and temp1 respectively.

Now we have terms like this $\frac{[\mathtt{PYR\_c}]\cdot[\mathtt{H\_m}]}{\mathtt{v9\_KiA}\cdot\mathtt{v9\_KiQ}}$ in which the hydrogen concentration has been fixed. These can be combined to give

$$\frac{[\mathtt{H\_m}]}{\mathtt{v9\_KiA}\cdot\mathtt{v9\_KiQ}} = temp2$$

Carrying out similar reduction for other similar terms we have the denominator as

$$\frac{[\mathtt{PYR\_c}]}{\mathtt{v9\_KiA}} + \frac{[\mathtt{PYR\_m}]}{\mathtt{v9\_KiB}} + [\mathtt{PYR\_c}] \cdot temp2 + [\mathtt{PYR\_m}] \cdot temp3 + temp0 + temp1 + 1$$

Combining all the pyruvate terms and factoring out the constant term from the denominator we have the reduced expression

$$\frac{\mathtt{v9\_1}\cdot[\mathtt{PYR\_m}]-\mathtt{v9\_2}\cdot[\mathtt{PYR\_c}]}{1+\mathtt{v9\_3}\cdot[\mathtt{PYR\_m}]+\mathtt{v9\_4}\cdot[\mathtt{PYR\_c}]}$$

Similar reductions were carried out for the other rate expressions.

Table A.5: Glycolysis kinetics. Glycolysis is modeled as a six-step reaction pathway generating pyruvate. These reactions are treated as influx to the pyruvate recycling pathways.

Reaction	Flux expression	Reference
J0entry_s	$\frac{\mathtt{v0\_1}\cdot(inglc-[\mathtt{GLC\_c}])}{1+\mathtt{v0\_2}\cdot(inglc+[\mathtt{glc\_c}])+inglc\cdot[\mathtt{glc\_c}]}$	Sweet and Matschinsky [108]
J1gk_c	$\frac{\mathtt{v1\_1}\cdot[\mathtt{glc\_c}]^{\mathtt{v1\_2}}}{\mathtt{v1\_3}^{\mathtt{v1\_2}}+[\mathtt{glc\_c}]^{\mathtt{v1\_2}}}$	SABIO-RK [112, 113] SABIO Reaction ID 793.
J2pfk_c	$\frac{\mathtt{v2\_1}\cdot[\mathtt{F6P\_c}]^{\mathtt{v2\_2}}}{\mathtt{v2\_3}^{\mathtt{v2\_2}}+[\mathtt{F6P\_c}]^{\mathtt{v2\_2}}}$	SABIO-RK [112, 113] SABIO Reaction ID 24.
J3fba_c	$\frac{\mathtt{v3\_1}\cdot[\mathtt{FBP\_c}]}{\mathtt{v3\_2}+[\mathtt{FBP\_c}]}$	SABIO-RK [112, 113] SABIO Reaction ID 1338.
J4gapd_c	$\frac{\mathtt{v4\_1}\cdot[\mathtt{GAP\_c}]^{\mathtt{v4\_2}}}{\mathtt{v4\_3}^{\mathtt{v4\_2}}+[\mathtt{GAP\_c}]^{\mathtt{v4\_2}}}$	SABIO-RK [112, 113] SABIO Reaction ID 7844.
J5pgp_c	$\frac{\mathtt{v5\_1}\cdot[\mathtt{DPG\_c}]}{\mathtt{v5\_2}+[\mathtt{DPG\_c}]}$	SABIO-RK [112, 113] SABIO Reaction ID 8953.
J6pk_c	$\frac{\mathtt{v6\_1}\cdot[\mathtt{PEP\_c}]^{\mathtt{v6\_2}}}{\mathtt{v6\_3}^{\mathtt{v6\_2}}+[\mathtt{PEP\_c}]^{\mathtt{v6\_2}}}$	SABIO-RK [112, 113] SABIO Reaction ID 10478.

Table A.6: Transporter rates. All the kinetics are described by **Rapid Equilibrium Random Bi Bi** kinetics

Reaction	Flux expression	Reference
J9pyr_s	$\frac{v9\_1\cdot[PYR\_m]-v9\_2\cdot[PYR\_c]}{1+v9\_3\cdot[PYR\_m]+v9\_4\cdot[PYR\_c]}$	Yugi and Tomita [116]
J10cit_s	$\frac{[CIT\_c]\cdot[MAL\_m]\cdot v10\_1-[MAL\_c]\cdot[CIT\_m]\cdot v10\_2}{denom}$ $denom = 1+\frac{[CIT\_c]}{v10\_3}+\frac{[MAL\_m]}{v10\_4}+\frac{[MAL\_c]}{v10\_5}+\frac{[CIT\_m]}{v10\_6}+\frac{[CIT\_c]\cdot[MAL\_m]}{v10\_3\cdot v10\_4}+\frac{[MAL\_c]\cdot[CIT\_m]}{v10\_5\cdot v10\_6}+\frac{[MAL\_m]\cdot[CIT\_m]}{v10\_4\cdot v10\_6}+\frac{[CIT\_c]\cdot[MAL\_c]}{v10\_3\cdot v10\_5}$	Yugi and Tomita [116]
J11icit_s	$\frac{[ICIT\_c]\cdot[MAL\_m]\cdot v11\_1-[MAL\_c]\cdot[ICIT\_m]\cdot v10\_2}{denom}$ $denom = 1+\frac{[ICIT\_c]}{v10\_3}+\frac{[MAL\_m]}{v10\_4}+\frac{[MAL\_c]}{v10\_5}+\frac{[ICIT\_m]}{v10\_6}+\frac{[ICIT\_c]\cdot[MAL\_m]}{v10\_3\cdot v10\_4}+\frac{[MAL\_c]\cdot[ICIT\_m]}{v10\_5\cdot v10\_6}+\frac{[MAL\_m]\cdot[ICIT\_m]}{v10\_4\cdot v10\_6}+\frac{[ICIT\_c]\cdot[MAL\_c]}{v10\_3\cdot v10\_5}$	Yugi and Tomita [116]
J12akg_s	$\frac{[AKG\_m]\cdot[MAL\_c]\cdot v12\_1-[MAL\_m]\cdot[AKG\_c]\cdot v12\_2}{denom}$ $denom = 1+\frac{[AKG\_m]}{v12\_3}+\frac{[MAL\_c]}{v12\_4}+\frac{[MAL\_m]}{v12\_5}+\frac{[AKG\_c]}{v12\_6}+\frac{[AKG\_m]\cdot[MAL\_c]}{v12\_3\cdot v12\_4}+\frac{[MAL\_m]\cdot[AKG\_c]}{v12\_5\cdot v12\_6}+\frac{[MAL\_c]\cdot[AKG\_c]}{v12\_4\cdot v12\_6}+\frac{[AKG\_m]\cdot[MAL\_m]}{v12\_3\cdot v12\_5}$	Yugi and Tomita [116]
J13malh_s	$\frac{v13\_1\cdot[MAL\_m]-v13\_2\cdot[MAL\_c]}{1+v13\_3\cdot[MAL\_m]+v13\_4\cdot[MAL\_c]}$	Yugi and Tomita [116]

Table A.7: Cytosolic Fluxes

Reaction	Flux expression	Reference
J7ldh_c	$\frac{\mathtt{v7\_1}\cdot([\mathtt{PYR_c\_m}]-\frac{[\mathtt{LAC\_c}]}{\mathtt{v7\_eq}})}{1+\mathtt{v7\_2}\cdot[\mathtt{PYR\_c}]+\mathtt{v7\_3}\cdot[\mathtt{LAC\_c}]}$	Modeled as reversible Michaelis Menten Kinetics all parameters from Hoefnagel *et.al.* [40]
J14nad_c	$\frac{\mathtt{v14\_1}\cdot[\mathtt{NADPH\_c}]}{\mathtt{v14\_2}+[\mathtt{NADPH\_c}]}$	Phenomenological model
J15citl_c	$\frac{\mathtt{v15\_1}\cdot([\mathtt{CIT\_c}]-\mathtt{v15\_2}\cdot[\mathtt{OAA\_c}])}{1+\mathtt{v15\_3}\cdot[\mathtt{CIT\_c}]+\mathtt{v15\_4}\cdot[\mathtt{OAA\_c}]}$	Westermark *et.al.* [110]
J16mdh_c	$\frac{\mathtt{v16\_1}\cdot([\mathtt{MAL\_c}]-\mathtt{v16\_2}\cdot[\mathtt{OAA\_c}])}{1+\mathtt{v16\_3}\cdot[\mathtt{MAL\_c}]+\mathtt{v16\_4}\cdot[\mathtt{OAA\_c}]}$	Yugi and Tomita [116]
J17acon_c	$\frac{\mathtt{v17\_1}\cdot[\mathtt{CIT\_c}]-\mathtt{v17\_2}\cdot[\mathtt{ICIT\_c}]}{\mathtt{v17\_3}\cdot[\mathtt{ICIT\_c}]+\mathtt{v17\_4}\cdot[\mathtt{CIT\_c}]+1}$	Yugi and Tomita [116]
J18isod_c	$\mathtt{v18\_1}\cdot\left(\frac{[\mathtt{ICIT\_c}]\cdot[\mathtt{NADP\_c}]}{\mathtt{v18\_3}\cdot[\mathtt{ICIT\_c}]\cdot[\mathtt{NADP\_c}]+\mathtt{v18\_4}\cdot[\mathtt{NADP\_c}]+\mathtt{v18\_5}\cdot[\mathtt{ICIT\_c}]+1}\right) - \mathtt{v18\_2}\cdot\left(\frac{[\mathtt{AKG\_c}]\cdot[\mathtt{NADPH\_c}]}{\mathtt{v18\_6}\cdot[\mathtt{AKG\_c}]\cdot[\mathtt{NADPH\_c}]+\mathtt{v18\_7}\cdot[\mathtt{NADPH\_c}]+\mathtt{v18\_8}\cdot[\mathtt{AKG\_c}]+1}\right)$	Yugi and Tomita [116]
J19me_c	$\frac{\mathtt{v19\_1}\cdot[\mathtt{NADP\_c}][\mathtt{MAL\_c}]\cdot-\frac{[\mathtt{PYR\_c}]\cdot[\mathtt{NADPH\_c}]}{\mathtt{v19\_eq}})}{denom}$ $denom = 1+\frac{[\mathtt{MAL\_c}]}{\mathtt{v19\_2}}+\frac{[\mathtt{NADP\_c}]}{\mathtt{v19\_3}}+\frac{[\mathtt{PYR\_c}]}{\mathtt{v19\_4}}+\frac{[\mathtt{NADPH\_c}]}{\mathtt{v19\_5}}+\frac{[\mathtt{MAL\_c}]\cdot[\mathtt{NADP\_c}]}{\mathtt{v19\_2}\cdot\mathtt{v12\_3}}+\frac{[\mathtt{PYR\_c}]\cdot[\mathtt{NADPH\_c}]}{\mathtt{v19\_4}\cdot\mathtt{v19\_5}}+\frac{[\mathtt{MAL\_c}]\cdot[\mathtt{PYR\_c}]}{\mathtt{v19\_2}\cdot\mathtt{v19\_4}}+\frac{[\mathtt{NADP\_c}]\cdot[\mathtt{NADPH\_c}]}{\mathtt{v19\_3}\cdot\mathtt{v19\_5}}$	Modeled as Rapid Equilibrium Random Bi Bi. All parameters from Brenda[96].

Table A.8: Mitochondrial Fluxes

Reaction	Flux expression	Reference
J20pdh_m	$\frac{\mathtt{v20\_1}\cdot[\mathtt{PYR\_m}]}{\mathtt{v20\_2}\cdot\left(1+\frac{[\mathtt{ACO\_m}]}{\mathtt{v20\_3}}\right)+[\mathtt{PYR\_m}]}$	Modeled as irreversible product inhibition. All the parameters from Brenda[96]
J21pc_m	$\frac{\mathtt{v21\_1}\cdot(\mathtt{v21\_2}\cdot[\mathtt{PYR\_m}]-[\mathtt{OAA\_m}])}{1+\mathtt{v21\_3}\cdot[\mathtt{PYR\_m}]+\mathtt{v21\_4}\cdot[\mathtt{OAA\_m}]}$	Yugi and Tomita [116]
J22cs_m	$\frac{\mathtt{v22\_1}\cdot[\mathtt{ACO\_m}]\cdot[\mathtt{OAA_m\_m}]}{[\mathtt{ACO\_m}]\cdot[\mathtt{OAA\_m}]+\mathtt{v22\_2}\cdot[\mathtt{OAA\_m}]+\mathtt{v22\_3}\cdot[\mathtt{ACO\_m}]+1}$	Yugi and Tomita [116]
J23ac_m	$\frac{\mathtt{v23\_1}\cdot[\mathtt{CIT\_m}]-\mathtt{v23\_2}\cdot[\mathtt{ICIT\_m}]}{\mathtt{v23\_3}\cdot[\mathtt{ICIT\_m}]+\mathtt{v23\_4}\cdot[\mathtt{CIT\_m}]+1}$	Yugi and Tomita [116]
J24icd_m	$\frac{\mathtt{v24\_1}\cdot\left([\mathtt{ICIT\_m}]^2+\mathtt{v24\_2}\cdot[\mathtt{ICIT\_m}]\right)}{\mathtt{v24\_3}[\mathtt{ICIT\_m}]^2+\mathtt{v24\_4}\cdot[\mathtt{ICIT\_m}]+1}$	Yugi and Tomita [116]
J25akg_m	$\frac{\mathtt{v25\_1}\cdot[\mathtt{AKG\_m}]}{1+\mathtt{v25\_2}\cdot[\mathtt{AKG\_m}]+\mathtt{V25\_3}\cdot[\mathtt{SCOA\_m}]+\mathtt{v25\_4}\cdot[\mathtt{AKG\_m}][\mathtt{SCOA\_m}]}$	Yugi and Tomita [116]
J26sco_m	$\frac{\mathtt{v26\_1}\cdot(\mathtt{v26\_2}\cdot[\mathtt{SCOA\_m}]-[\mathtt{SUC\_m}])(\mathtt{v26\_3}\cdot[\mathtt{SUC\_m}]+1)}{denom}$ $denom = 1+\mathtt{v26\_4}\cdot[\mathtt{SCOA\_m}]+\mathtt{v26\_5}\cdot[\mathtt{SUC\_m}]+\mathtt{v26\_6}\cdot[\mathtt{SUC\_m}]^2+\mathtt{v26\_7}\cdot[\mathtt{SCOA\_m}][\mathtt{SUC\_m}]$	Yugi and Tomita [116]
J27sdh_m	$\frac{\mathtt{v27\_1}\cdot([\mathtt{SUC\_m}]-[\mathtt{FUM\_m}]\cdot\mathtt{v27\_2})}{1+\mathtt{v27\_3}\cdot[\mathtt{SUC\_m}]+\mathtt{v27\_4}\cdot[\mathtt{FUM\_m}]+\mathtt{V27\_5}\cdot[\mathtt{SUC\_m}][\mathtt{FUM\_m}]}$	Yugi and Tomita [116]
J28fum_m	$\frac{\mathtt{v28\_1}\cdot[\mathtt{FUM\_m}]-\mathtt{v28\_2}\cdot[\mathtt{MAL\_m}]}{\mathtt{v28\_3}\cdot[\mathtt{MAL\_m}]+\mathtt{v28\_4}\cdot[\mathtt{FUM\_m}]+1}$	Yugi and Tomita [116]
J29mdh_m	$\frac{\mathtt{v29\_1}\cdot[\mathtt{MAL\_m}]-\mathtt{v29\_2}\cdot[\mathtt{OAA\_m}]}{1+\mathtt{v29\_3}\cdot[\mathtt{MAL\_m}]+\mathtt{v29\_4}\cdot[\mathtt{OAA\_m}]+\mathtt{v29\_5}\cdot[\mathtt{OAA\_m}][\mathtt{MAL\_m}]}$	Yugi and Tomita [116]
J30me_m	$\frac{\mathtt{v30\_1}\cdot([\mathtt{MAL\_m}]-\frac{[\mathtt{PYR\_m}]}{\mathtt{v30\_eq}})}{1+\mathtt{v30\_2}\cdot[\mathtt{MAL\_m}]+\mathtt{v30\_3}\cdot[\mathtt{PYR\_m}]}$	Modeled as Reversible Michaelis Menten. All the parameters from Brenda[96]

A.1.5 State Differential Equations

$$\frac{d[PEP\_c]}{dt} = J5pgp\_c - J6pk\_c$$
$$\frac{d[LAC\_c]}{dt} = J7ldh\_c - lacsink\_c$$
$$\frac{d[PYR\_c]}{dt} = J6pk\_c - J7ldh\_c + Vr * J9pyr\_s + J19me\_c$$
$$\frac{d[MAL\_c]}{dt} = -J16mdh\_c + Vr * (J13malh\_s + J10cit\_s - J12akhmal\_s + J11icit\_s) - J19me\_c$$
$$\frac{d[CIT\_c]}{dt} = -J17acon\_c - J15citl\_c - Vr * J10cit\_s$$
$$\frac{d[ICIT\_c]}{dt} = -J18isod\_c + J17acon\_c - Vr * J11icit\_s$$
$$\frac{d[AKG\_c]}{dt} = J18isod\_c + Vr * J12akhmal\_s - akgflow\_c$$
$$\frac{d[OAA\_c]}{dt} = J15citl\_c + J16mdh\_c$$
$$\frac{d[NADPH\_c]}{dt} = J18isod\_c + J19me\_c - J14nadph\_c$$
$$\frac{d[PYR\_m]}{dt} = -J21pc\_m + J30me\_m - J9pyr\_s - J20pdh\_m$$
$$\frac{d[ACO\_m]}{dt} = J20pdh\_m - J22cs\_m$$
$$\frac{d[CIT\_m]}{dt} = J22cs\_m - J23ac\_m + J10cit\_s$$
$$\frac{d[ICIT\_m]}{dt} = J23ac\_m - J24icd\_m + J11icit\_s$$
$$\frac{d[AKG\_m]}{dt} = J24icd\_m - J25akg\_m - J12akhmal\_s$$
$$\frac{d[SCOA\_m]}{dt} = J25akg\_m - J26sco\_m$$
$$\frac{d[SUC\_m]}{dt} = J26sco\_m - J27sdh\_m$$

$$\frac{d[FUM\_m]}{dt} = J27sdh\_m - J28fum\_m$$
$$\frac{d[MAL\_m]}{dt} = -J29mdh\_m + J28fum\_m - J10cit\_s$$
$$- J11icit\_s - J13malh\_s + J12akhmal\_s - J30me\_m$$
$$\frac{d[OAA\_m]}{dt} = -J22cs\_m + J29mdh\_m + J21pc\_m$$

A.1.6 ODE Initial Conditions

The initial condition is fixed by integrating the system from 0 initial condition till 4hrs (7200s) under appropriate glucose conditions.

A.2 Computational Settings for Solvers

A.2.1 Steady State Calculation

To calculate the steady state we used the ode15s and fsolve functions of MATLAB®. The differential equation was first integrated up to 10^7 seconds. This point was then passed to fsolve to confirm the steady state conditions had been achieved,. In order to increase stability and robustness of solvers, we generated symbolic Jacobians using SBTOOLBOX2 [97]. Since only 18% of the Jacobian coefficients were non-zero, we utilized the sparse storage mechanism as described in the ode15s and fsolve manual in order to increase the efficiency of solvers. We fixed the relative tolerance of ode15s at 1e-3 and the absolute tolerance at 1e-6 except for F6P and G6P which were fixed at 1e-12. For fsolve we choose the default values of TolX and TolF (1e-6).

A.2.2 Parameter Optimization

Parameter optimization proceeded in two steps. To begin, we fitted the glycolysis parameters to appropriate levels of the output pyruvate. In the second phase of parameter estimation some of the parameters were manually adjusted and then second subset of parameters were optimized. The least-squares objective function is defined as follows.

$$f(x) = \frac{1}{N}\sum_{i}^{n}\frac{1}{\sigma_i}\frac{xobs(x)_i - xsim(x)_i}{xobs(x)_i}$$

where N is the number of experimental time-points, $xobs(x)_i$ is the observed value of i^{th} state, $xsim(x)_i$ is the corresponding i^{th} simulated state and σ_i is the standard error of mean (SEM) of the i^{th} state. If the error is unknown then it was assumed to be 10%. The parameters were optimized in the range $.01p_{nom} \leq p_{nom} \leq 100p_{nom}$, where p_{nom} is the nominal parameter values.We used a combination of simplexSB and simannealSB of system biology toolbox for parameter optimization [97].

A.2.3 Global Sensitivity Analysis Settings

We used the variance-based Global Sensitivity Analysis (GSA) Sobol's Method, extended Fourier amplitude sensitivity test (eFAST) and partial rank correlation method (PRCC) implemented in SBTOOLBOX2 [97]. The analysis treated all model parameters expect for the glycolysis parameters. The relative parameter range variation was selected to be 100%. For the total sensitivity analysis, the objective function was defined as the sum of

the squared errors between the observed and perturbed system output values:

$$f_{obj} = \sum_{i}^{n} (x^i_{nom} - x^i_{pert})^2$$

where x_{nom} is the steady state nominal model output and x_{pert} is the steady state perturbed model output,n is the number of varaibles. In addition we calculated the sensitivities of individual variables. This can simply be defined as a squared error of each variable without any extra model evaluation.

$$f^i_{ind} = (x^i_{nom} - x^i_{pert})^2 \quad \text{for i=1..n}$$

The Total number of model simulations was selected to be 10^5, based on the suggestion of Saltelli [93] ($N = 2 * 512 *$ total number of parameters).

The system output was taken as all the state variables and fluxes participating in TCA cycle and pyruvate recycling pathways (none from the glycolysis pathway). Similarly, parameters was choosen excluding glycolysis. The total numbers of parameters for analysis was 100.

Integration Settings for Global Optimization For simulating the model for global sensitivity analysis we used the SUNDIALS [39] package (MATLAB® interface) in order to reduce the simulation time [97]. The final value was checked for steady-state as described previously using fsolve. The function was integrated using a relative tolerance of 1e-4 and an absolute tolerance of 1e-14 for all the species. With this setting the integrator output is the same as MATLAB® ode15s solver.

A.3 Parameters

Parameter Classification We classified the parameters as follows

Table A.9: Classification of different parameters

Class	Definition	Example
Class 0	Literature values	`v1_3`
Class 1	Optimized around the experimental values or estimated to fit the training data	`v0_1` or ? $\leq$ `v14_1` $\leq$?

Table A.10: Model parameters. This model contains 123 global parameters. Units: Molarity (M) Seconds (s)

Name	Value	Units	Class	Name	Value	Units	Class
`v0_1`	$2.7271 \cdot 10^{-6}$	M·s^{-1}	1	`v6_3`	2.9		0
`v0_2`	101.0544	M	1	`v7_1`	29.0969	M·s^{-1}	1
`v1_1`	$1.3424 \cdot 10^{-4}$	M·s^{-1}	1	`v7_eq`	21.121		0
`v1_2`	$3.0118 \cdot 10^{-4}$	M	1	`v7_2`	448491.0	M	1
`v1_3`	1.34		0	`v7_3`	449.0936	M	0
`v2_1`	$3.16667 \cdot 10^{-5}$	M·s^{-1}	0	`v9_1`	$3.7674 \cdot 10^{-8}$	M·s^{-1}	1
`v2_2`	0.0089	M	0	`v9_2`	0.004	M·s^{-1}	1
`v2_3`	0.9		0	`v9_3`	49.2637	M	1
`v3_1`	$7.97833 \cdot 10^{-5}$	M·s^{-1}	0	`v9_4`	187.3789	M	1
`v3_2`	$4 \cdot 10^{-6}$	M	0	`v10_1`	32514.0	M·s^{-1}	0
`v4_1`	0.001	M·s^{-1}	0	`v10_2`	84267.0	M·s^{-1}	0
`v4_2`	$3.2 \cdot 10^{-4}$	M	0	`v10_3`	$1.3 \cdot 10^{-4}$	M	0
`v4_3`	1.5		0	`v10_4`	$4.4 \cdot 10^{-4}$	M	0
`v5_1`	$3.33 \cdot 10^{-5}$	M·s^{-1}	0	`v10_5`	$3.3 \cdot 10^{-4}$	M	0
`v5_2`	$8 \cdot 10^{-6}$	M	0	`v10_6`	$4.18 \cdot 10^{-5}$	M	0
`v6_1`	$5.33 \cdot 10^{-5}$	M·s^{-1}	0	`v12_1`	5811.9	M·s^{-1}	0
`v6_2`	$1.5 \cdot 10^{-4}$	M	0	`v12_2`	6739.9	M·s^{-1}	0

Table A.11: Model parameters. This model contains 123 global parameters. Units: Molarity (M) Seconds (s)

Name	Value	Units	Class	Name	Value	Units	Class
v12_3	$3 \cdot 10^{-4}$	M	0	v20_1	$1.417 \cdot 10^{-7}$	$M \cdot s^{-1}$	0
v12_4	$7 \cdot 10^{-4}$	M	0	v20_2	$3.5 \cdot 10^{-5}$	M	0
v12_5	.0014	M	0	v20_3	$2 \cdot 10^{-5}$	M	0
v12_6	$1.7 \cdot 10^{-4}$	M	1	v21_1	0.1057	$M \cdot s^{-1}$	1
v13_1	0.8512	$M \cdot s^{-1}$	0	v21_2	0.54	M	1
v13_2	0.2721	$M \cdot s^{-1}$	0	v21_3	4424100.0	M	1
v13_3	1388.9	M	0	v21_4	$4.8528 \cdot 10^{7}$	M	1
v13_4	1111.1	M	0	v22_1	50.85	$M \cdot s^{-1}$	1
v14_1	0.0025598	$M \cdot s^{-1}$	1	v22_2	$2.5 \cdot 10^{10}$	M	1
v14_2	0.98653	M	0	v22_3	295000.0	M	0
v15_1	$4.0008 \cdot 10^{-7}$	$M \cdot s^{-1}$	1	v22_4	120000.0	M	1
v15_2	$1.2 \cdot 10^{-4}$	M	1	v23_1	0.0518	$M \cdot s^{-1}$	0
v16_1	.0036	$M \cdot s^{-1}$	0	v23_2	0.1104	$M \cdot s^{-1}$	0
v16_2	5000	$M \cdot s^{-1}$	0	v23_3	9090.9	M	0
v16_3	$8 \cdot 10^{-6}$	M	0	v23_4	2000.0	M	0
v16_4	16667	M	0	v24_1	0.1126	$M \cdot s^{-1}$	0
v17_1	0.0518	$M \cdot s^{-1}$	0	v24_2	0.0148	$M \cdot s^{-1}$	0
v17_2	0.1104	$M \cdot s^{-1}$	0	v24_3	2777.5	M	0
v17_3	9090.0	M	0	v24_4	0.63969	M	0
v17_4	2000.0	M	0	v25_1	0.0311	$M \cdot s^{-1}$	1
v18_1	1152100.0	$M \cdot s^{-1}$	0	v25_2	$1.456 \cdot 10^{9}$	M	1
v18_2	5482500.0	$M \cdot s^{-1}$	0	v25_3	$1.4546 \cdot 10^{9}$	M	1
v18_3	$2.3042 \cdot 10^{10}$	M	0	v25_4	24691.0	M	1
v18_4	142857.1	M	0	v26_1	$3.32 \cdot 10^{-5}$	$M \cdot s^{-1}$	1
v18_5	161290.3	M	0	v26_2	6.4	M	1
v18_6	$1.0965 \cdot 10^{11}$	M	0	v26_3	4.1876	M	1
v18_7	416666.7	M	0	v26_4	37.5348	M	1
v18_8	263157.9	M	0	v26_5	1478.2	M	1
v19_1	913070.0	$M \cdot s^{-1}$	0	v26_6	9509.6	M	1
v19_eq	1000		0	v26_7	236.7114	M	1
v19_2	$1.2 \cdot 10^{-4}$	M	0	v27_1	2.941	$M \cdot s^{-1}$	1
v19_3	$1.39 \cdot 10^{-6}$	M	0	v27_2	11.5344	M	1
v19_4	0.0048	M	0	v27_3	449.6613	M	1
v19_5	$5.3 \cdot 10^{-6}$	M	0	v27_4	199130.0	M	1

Table A.12: Model parameters. This model contains 123 global parameters. Units: Molarity (M) Seconds (s)

Name	Value	Units	Class
v27_5	$1.7921 \cdot 10^{8}$	M	1
v28_1	13.9024	$M \cdot s^{-1}$	1
v28_2	13.9024	$M \cdot s^{-1}$	1
v28_3	4000000.0	M	1
v28_4	880000.0	M	1
v29_1	.0016	$M \cdot s^{-1}$	1
v29_2	$2.5563 \cdot 10^{-10}$	$M \cdot s^{-1}$	1
v29_3	33263.0	M	1
v29_4	14.0754	M	1
v29_5	2742900.0	M	1
v30_1	157.8125	$M \cdot s^{-1}$	1
v30_eq	1000		1
v30_2	500	M	1
v30_3	227.2727	M	0

A.4 Supplementary Sensitivity Plots

A.4.1 Sensitivity Rankings: Overall Measures

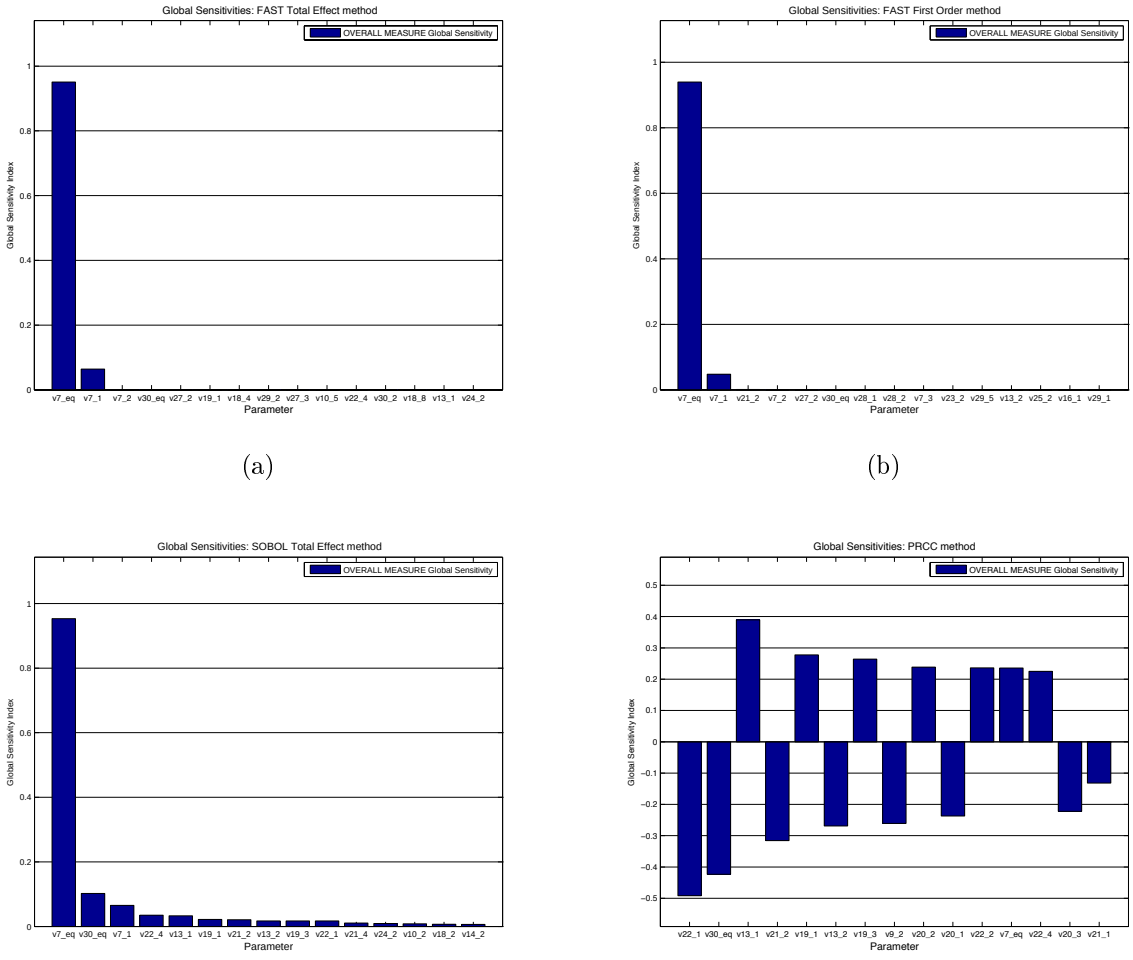

Figure A.1: Global Sensitivity Rankings of Overall Measures across different methods. Panel A eFAST total effect, Panel B eFAST first order, Panel C Sobol's total effect and Panel D PRCC. For parameters description refer to Tables A.8,A.7 and A.6

A.4.2 ICDc effect

We perturbed the V_{max} of ICDc and measured the effect on the pyruvate recycle fluxes. As expected the transport fluxes are more effected and there is no significant effect on PC and MEc or MEm. The result is shown in figure A.2.

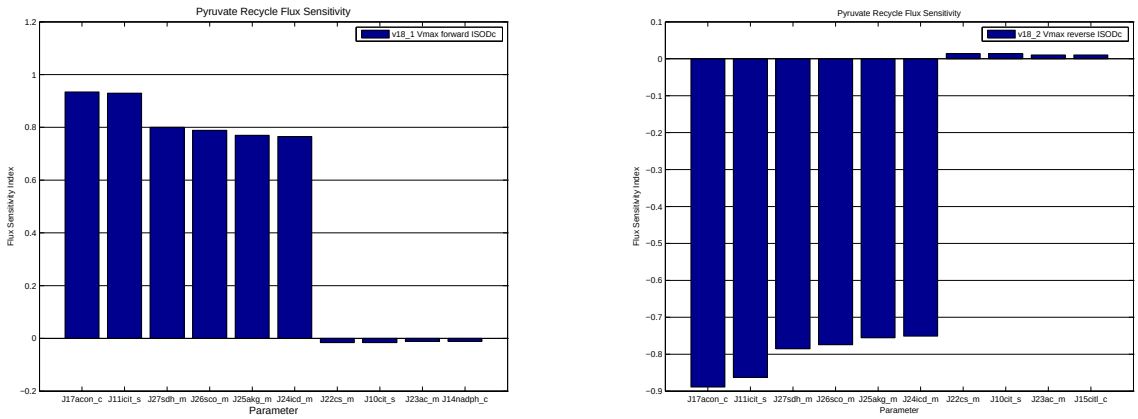

(a) (b)

Figure A.2: A.2a Effect of perturbation in V_{max} forward on fluxes. A.2b Effect of perturbation in V_{max} reverse on fluxes.

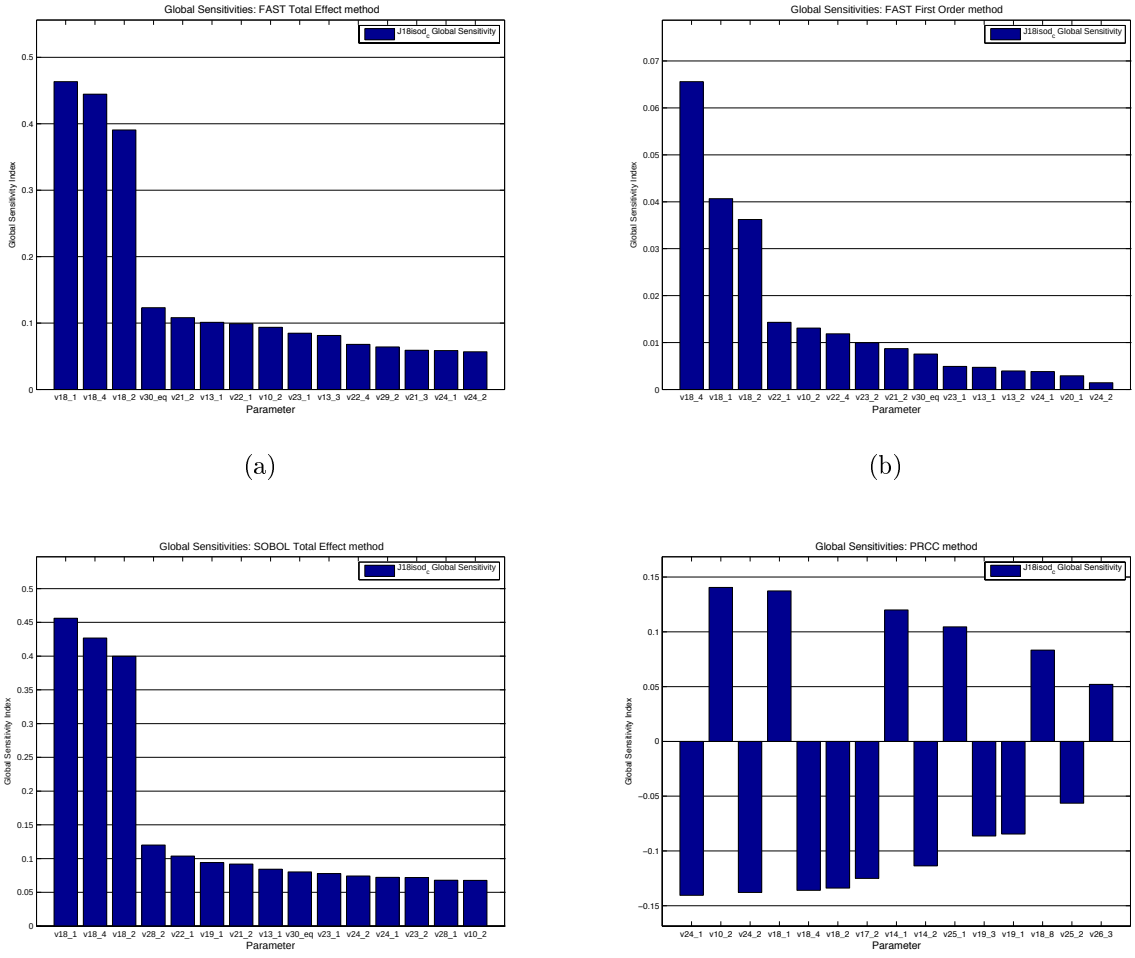

Figure A.3: Global Sensitivity Rankings of ICDc across different methods. Panel A eFAST total effect, Panel B eFAST first order, Panel C Sobol's total effect and Panel D PRCC. For parameters description refer to Tables A.8,A.7 and A.6

A.4.3 Mitochondrial Pyruvate Sensitivity

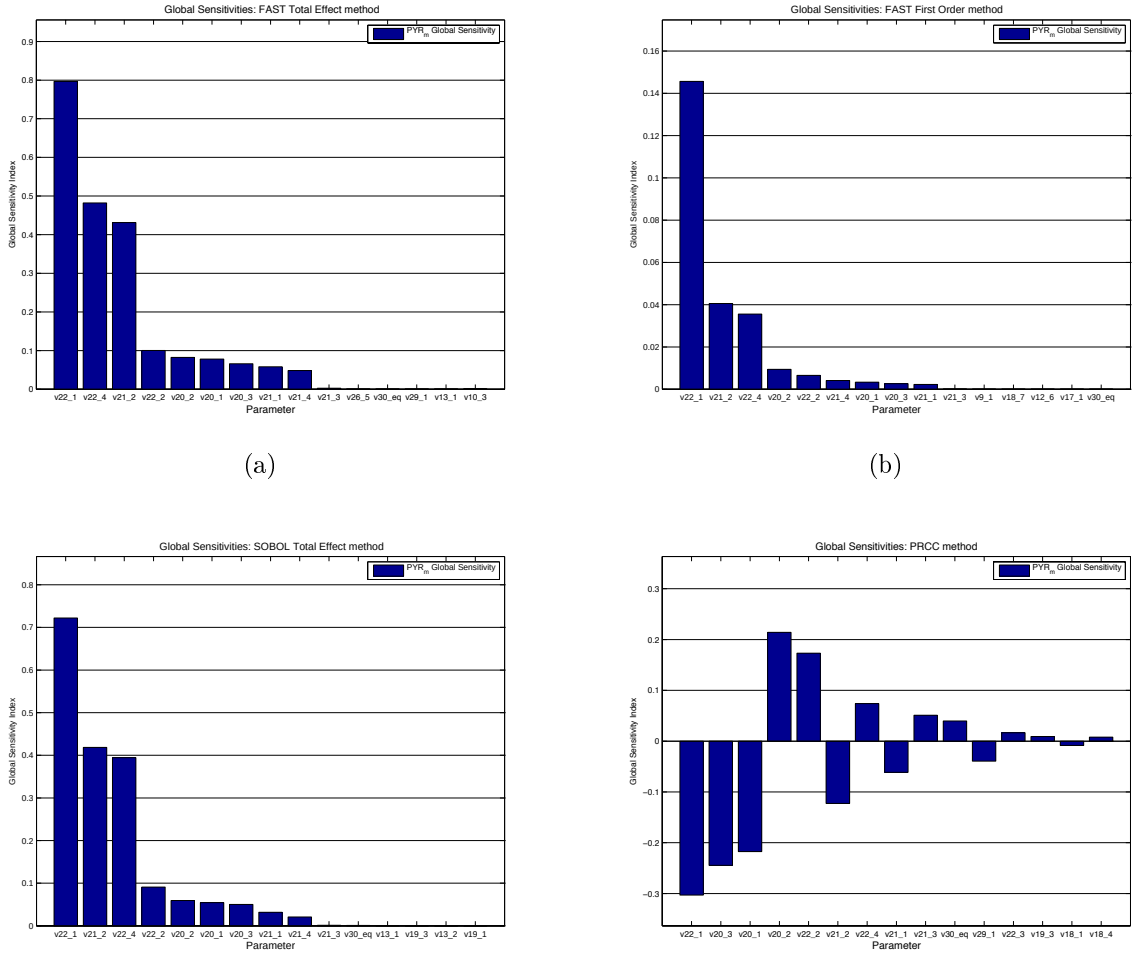

(a) (b)

(c) (d)

Figure A.4: Global Sensitivity Rankings of mitochondrial pyruvate across different methods. Panel A eFAST total effect, Panel B eFAST first order, Panel C Sobol's total effect and Panel D PRCC. For parameters description refer to Tables A.8,A.7 and A.6

References

[1] Samy M Abdel-Halim, Amel Guenifi, Akhtar Khan, Olof Larsson, Per-Olof Berggren, Claes-Goran Ostenson, and Suad Efendic. Impaired coupling of glucose signal to the exocytotic machinery in diabetic gk rats. *Diabetes*, 45(7):934–940, 1996.

[2] N. M. Alexandrov, J. E. Dennis, R. M. Lewis, and V. Torczon. A trust-region framework for managing the use of approximation models in optimization. *Structural and Multidisciplinary Optimization*, 15:16–23, 1998.

[3] L. L. Baggio and D. J. Drucker. Biology of incretins: GLP-1 and GIP. *Gastroenterology*, 132:2131–2157, 2007.

[4] J.W. Bandler, Q.S. Cheng, S.A. Dakroury, A.S. Mohamed, M.H. Bakr, K. Madsen, and J. Sondergaard. Space mapping: the state of the art. *Microwave Theory and Techniques, IEEE Transactions on*, 52(1):337 – 361, jan. 2004.

[5] S. M. Blower and H. Dowlatabadi. Sensitivity and uncertainty analysis of complex models of disease transmission: An HIV model, as an example. *International Statistical Review / Revue Internationale de Statistique*, 62(2):229–243, 1994.

[6] A. J. Booker, J. E. Dennis, P. D. Frank, D. B. Serafini, V. Torczon, and M. W. Trosset. A rigorous framework for optimization of expensive functions by surrogates. *Structural and Multidisciplinary Optimization*, 17:1–13, 1999.

[7] A. Boucher. Biochemical mechanism of lipid-induced impairment of glucose-stimulated insulin secretion and reversal with a malate analogue. *J. Biol. Chem.*, 279:27263–27271, 2004.

[8] G E Briggs and J B Haldane. A Note on the Kinetics of Enzyme Action. *The Biochemical journal*, 19(2):338–9, 1925.

[9] Martin Bücker. *Automatic differentiation applications, theory and implementations /*. Berlin ;New York : Springer, c2006, 2006.

[10] C B Chan and R M MacPhail. KATP channel-dependent and -independent pathways of insulin secretion in isolated islets from fa/fa zucker rats. *Biochemistry and cell biology = Biochimie et biologie cellulaire*, 74(3):403–410, 1996. PMID: 8883846.

[11] G. W. Cline, R. L. Lepine, K. K. Papas, R. G. Kibbey, and G. I. Shulman. ^{13}C NMR isotopomer analysis of anaplerotic pathways in INS-1 cells. *J. Biol. Chem.*, 279:44370–44375, 2004.

[12] Andrew R. Conn, Nicholas I. M. Gould, and Philippe L. Toint. *Trust-Region Methods*. SIAM, 2000.

[13] H. G. Coore and P. J. Randle. Regulation of insulin secretion studied with pieces of rabbit pancreas incubated in vitro. *Biochemical Journal*, 93(1):66–78, October 1964. PMID: 5320084 PMCID: PMC1206183.

[14] Athel Cornish-Bowden. *Fundamentals of Enzyme Kinetics*. Portland Press Limited, 59 Portland Press London U.K., 1995.

[15] R. I. Cukier, C. M. Fortuin, K. E. Shuler, A. G. Petschek, and J. H. Schaibly. Study of the sensitivity of coupled reaction systems to uncertainties in rate coefficients. i theory. *The Journal of Chemical Physics*, 59(8):3873–3878, October 1973.

[16] P. M. Dean and E. K. Matthews. Electrical activity in pancreatic islet cells. , *Published online: 27 July 1968; | doi:10.1038/219389a0*, 219(5152):389–390, July 1968.

[17] Oleg Demin and Igor Goryanin. *Kinetic Modelling in Systems Biology*. CRC Press, 2009.

[18] Andreas Drager, Nadine Hassis, Jochen Supper, Adrian Schroder, and Andreas Zell. Sbmlsqueezer: A celldesigner plug-in to generate kinetic rate equations for biochemical networks. *BMC Systems Biology*, 2(1):39, 2008.

[19] Norman Richard Draper and Harry Smith. *Applied regression analysis*. Wiley, April 1998.

[20] I. Dulubova. A Munc13/RIM/Rab3 tripartite complex: from priming to plasticity? *EMBO J.*, 24:2839–2850, 2005.

[21] G. S. Eadie. The inhibition of cholinesterase by physostigmine and prostigmine. *Journal of Biological Chemistry*, 146(1):85–93, 1942.

[22] Lars Eldén, Linde Wittmeyer-Koch, and Hans Bruun Nielson. *Introduction to Numerical Computation- analysis and MATLAB® illustrations*. Studentlitteratur AB, Lund, Sweden, 2004.

[23] K. Eto. Role of NADH Shuttle System in Glucose-Induced Activation of Mitochondrial Metabolism and Insulin Secretion. *Science*, 283(5404):981–985, 1999.

[24] D Fell. *Understanding the Control of Metabolism*, volume 2 of *Frontiers in metabolism, 2*. Portland Press, 1997.

[25] Shimpei Fujimoto, Hitoshi Ishida, Seika Kato, Yoshimasa Okamoto, Kazuo Tsuji, Nobuhisa Mizuno, Satoko Ueda, Eri Mukai, and Yutaka Seino. The novel insulinotropic mechanism of pimobendan: Direct enhancement of the exocytotic process of insulin secretory granules by increased ca2+ sensitivity inO¢ -cells. *Endocrinology*, 139(3):1133–1140, 1998.

[26] M Gembal, P Gilon, and J C Henquin. Evidence that glucose can control insulin release independently from its action on ATP-sensitive k+ channels in mouse b cells. *Journal of Clinical Investigation*, 89(4):1288–1295, April 1992.

[27] Andreas Griewank and Andrea Walther. *Evaluating Derivatives: Principles and Techniques of Algorithmic Differentiation*. SIAM, 2008.

[28] G M Grodsky and L L Bennett. Cation requirements for insulin secretion in the isolated perfused pancreas. *Diabetes*, 15(12):910–913, December 1966. PMID: 5957483.

[29] Gerold M. Grodsky, Adrienne A. Batts, Leslie L. Bennett, Carl Vcella, Nancy B. McWilliams, and Desmond F. Smith. Effects of carbohydrates on secretion of in-

sulin from isolated rat pancreas. *American Journal of Physiology – Legacy Content*, 205(4):638–644, October 1963.

[30] Segel I H. *Enzyme Kinetics: Behavior and Analysis of Rapid Equilibrium and Steady-State Enzyme Systems*. Wiley-Interscience, U.S.A, 1993.

[31] C S Hanes. Studies on plant amylases: The effect of starch concentration upon the velocity of hydrolysis by the amylase of germinated barley. *The Biochemical journal*, 26(5):1406–1421, 1932. PMID: 16744959.

[32] C J Hedeskov, K Capito, and P Thams. Cytosolic ratios of free [NADPH]/[NADP+] and [NADH]/[NAD+] in mouse pancreatic islets, and nutrient-induced insulin secretion. *The Biochemical journal*, 241(1):161–7, January 1987.

[33] C J Hedeskov, K Capito, and P Thams. Cytosolic ratios of free [NADPH]/[NADP+] and [NADH]/[NAD+] in mouse pancreatic islets, and nutrient-induced insulin secretion. *The Biochemical journal*, 241(1):161–167, 1987.

[34] R Heinrich and T A Rapoport. A linear steady-state treatment of enzymatic chains. General properties, control and effector strength. *European journal of biochemistry / FEBS*, 42(1):89–95, February 1974.

[35] Reinhart Heinrich and Stefan Schuster. *The Regulation Of Cellular Systems*. Springer, August 1996.

[36] J C Henquin. Triggering and amplifying pathways of regulation of insulin secretion by glucose. *Diabetes*, 49(11):1751–1760, 2000.

[37] J. C. Henquin, M. A. Ravier, M. Nenquin, J. C. Jonas, and P. Gilon. Hierarchy of the β-cell signals controlling insulin secretion. *Eur. J. Clin. Invest.*, 33:742–750, 2003.

[38] A. V. Hill. The possible effects of the aggregation of the molecules of haemoglobin on its dissociation curves. *J Physiol*, 40:iv–vii, 1910.

[39] Alan C. Hindmarsh, Peter N. Brown, Keith E. Grant, Steven L. Lee, Radu Serban, Dan E. Shumaker, and Carol S. Woodward. Sundials: Suite of nonlinear and differential/algebraic equation solvers. *ACM Trans. Math. Softw.*, 31(3):363–396, September 2005.

[40] Marcel H N Hoefnagel, Marjo J C Starrenburg, Dirk E Martens, Jeroen Hugenholtz, Michiel Kleerebezem, Iris I Van Swam, Roger Bongers, Hans V Westerhoff, and Jacky L Snoep. Metabolic engineering of lactic acid bacteria, the combined approach: kinetic modelling, metabolic control and experimental analysis. *Microbiology (Reading, England)*, 148(Pt 4):1003–13, April 2002.

[41] H. E. Hohmeier, H. Mulder, G. Chen, R. Henkel-Rieger, M. Prentki, and C. B. Newgard. Isolation of INS-1-derived cell lines with robust ATP-sensitive k+ channel-dependent and -independent glucose-stimulated insulin secretion. *Diabetes*, 49(3):424–430, March 2000.

[42] I.M. Global sensitivity indices for nonlinear mathematical models and their monte carlo estimates. *Mathematics and Computers in Simulation*, 55(1-3):271–280, February 2001.

[43] Brown A J. Enzyme action. *J. Chem. Soc. Trans*, 1902.

[44] Kenneth R. Jackson and Nedialko S. Nedialkov. Some recent advances in validated methods for ivps for odes. *Applied Numerical Mathematics*, 42(1-3):269 – 284, 2002.

[45] M. V. Jensen. Compensatory responses to pyruvate carboxylase suppression in islet β-cells. preservation of glucose-stimulated insulin secretion. *J. Biol. Chem.*, 281:22342–22351, 2006.

[46] Mette V. Jensen, Jamie W. Joseph, Olga Ilkayeva, Shawn Burgess, Danhong Lu, Sarah M. Ronnebaum, Matthew Odegaard, Thomas C. Becker, A. Dean Sherry, and Christopher B. Newgard. Compensatory responses to pyruvate carboxylase suppression in islet β-cells. *Journal of Biological Chemistry*, 281(31):22342–22351, 2006.

[47] Nan Jiang, Roger Cox, and John Hancock. A kinetic core model of the glucose-stimulated insulin secretion network of pancreatic β-cells. *Mammalian Genome*, 18:508–520, 2007. 10.1007/s00335-007-9011-y.

[48] Hassan Jijakli and Willy J Malaisse. Cationic events stimulated by d-glucose in depolarized islet cells. *Cellular Signalling*, 9(3вПЂБ4):283 – 290, 1997.

[49] J. W. Joseph. The mitochondrial citrate/isocitrate carrier plays a regulatory role in glucose-stimulated insulin secretion. *J. Biol. Chem.*, 281:35624–35632, 2006.

[50] J. W. Joseph. Normal flux through ATP-citrate lyase or fatty acid synthase is not required for glucose-stimulated insulin secretion. *J. Biol. Chem.*, 282:31592–31600, 2007.

[51] Jamie W Joseph, Mette V Jensen, Olga Ilkayeva, Ferdinando Palmieri, Cristina Alárcon, Christopher J Rhodes, and Christopher B Newgard. The mitochondrial citrate/isocitrate carrier plays a regulatory role in glucose-stimulated insulin secretion. *The Journal of biological chemistry*, 281(47):35624–32, 2006.

[52] Jamie W Joseph, Matthew L Odegaard, Sarah M Ronnebaum, Shawn C Burgess, Jeffrey Muehlbauer, a Dean Sherry, and Christopher B Newgard. Normal flux through ATP-citrate lyase or fatty acid synthase is not required for glucose-stimulated insulin secretion. *The Journal of biological chemistry*, 282(43):31592–600, 2007.

[53] H Kacser and J A Burns. The control of flux. *Symposia of the Society for Experimental Biology*, 27:65–104, 1973. PMID: 4148886.

[54] Minoru Kanehisa, Susumu Goto, Yoko Sato, Miho Furumichi, and Mao Tanabe. Kegg for integration and interpretation of large-scale molecular data sets. *Nucleic Acids Research*, 40(D1):D109–D114, 2012.

[55] G G Kelley, K C Zawalich, and W S Zawalich. Calcium and a mitochondrial signal interact to stimulate phosphoinositide hydrolysis and insulin secretion in rat islets. *Endocrinology*, 134(4):1648–54, 1994.

[56] A. Khan, Z. C. Ling, and B. R. Landau. Quantifying the carboxylation of pyruvate in pancreatic islets. *J. Biol. Chem.*, 271:2539–2542, 1996.

[57] Akhtar Khan, Zong Chao Ling, and Bernard R. Landau. Quantifying the carboxylation of pyruvate in pancreatic islets. *Journal of Biological Chemistry*, 271(5):2539–2542, 1996.

[58] R. G. Kibbey. Mitochondrial GTP regulates glucose-stimulated insulin secretion. *Cell Metab.*, 5:253–264, 2007.

[59] S Kirkpatrick, C D Gelatt, and M P Vecchi. Optimization by simulated annealing. *Science (New York, N.Y.)*, 220(4598):671–80, May 1983.

[60] Edda Klipp. *Systems Biology In Practice: Concepts, Implementation And Application*. John Wiley & Sons, May 2005.

[61] Peter J. M. Laarhoven and Emile H. L. Aarts. *Simulated Annealing: Theory and Applications*. Springer, June 1987.

[62] Hans Lineweaver and Dean Burk. The determination of enzyme dissociation constants. *Journal of the American Chemical Society*, 56(3):658–666, 1934.

[63] Danhong Lu, Hindrik Mulder, Piyu Zhao, Shawn C. Burgess, Mette V. Jensen, Svetlana Kamzolova, Christopher B. Newgard, and A. Dean Sherry. 13C NMR isotopomer analysis reveals a connection between pyruvate cycling and glucose-stimulated insulin secretion (gsis). *Proceedings of the National Academy of Sciences*, 99(5):2708–2713, 2002.

[64] M. J. MacDonald. Estimates of glycolysis, pyruvate (de)carboxylation, pentose phosphate pathway, and methyl succinate metabolism in incapacitated pancreatic islets. *Arch. Biochem. Biophys.*, 305:205–214, 1993.

[65] M. J. MacDonald. Feasibility of a mitochondrial pyruvate malate shuttle in pancreatic islets. further implication of cytosolic NADPH in insulin secretion. *J. Biol. Chem.*, 270:20051–20058, 1995.

[66] Michael J. MacDonald, Leonard A. Fahien, Laura J. Brown, Noaman M. Hasan, Julian D. Buss, and Mindy A. Kendrick. Perspective: emerging evidence for signaling roles of mitochondrial anaplerotic products in insulin secretion. *Am J Physiol Endocrinol Metab*, 288(1):E1–15, 2005.

[67] Willy J. Malaisse, Leonard Best, Shoji Kawazu, Francine Malaisse-Lagae, and Abdullah Sener. The stimulus-secretion coupling of glucose-induced insulin release: Fuel metabolism in islets deprived of exogenous nutrient. *Archives of Biochemistry and Biophysics*, 224(1):102 – 110, 1983.

[68] Lisa Matthews, Gopal Gopinath, Marc Gillespie, Michael Caudy, David Croft, Bernard de Bono, Phani Garapati, Jill Hemish, Henning Hermjakob, Bijay Jassal, Alex Kanapin, Suzanna Lewis, Shahana Mahajan, Bruce May, Esther Schmidt, Imre Vastrik, Guanming Wu, Ewan Birney, Lincoln Stein, and Peter D'Eustachio. Reactome knowledgebase of human biological pathways and processes. *Nucleic acids research*, 37(Database issue):D619–622, January 2009. PMID: 18981052.

[69] M. D. McKay, R. J. Beckman, and W. J. Conover. A comparison of three methods for selecting values of input variables in the analysis of output from a computer code. *Technometrics*, 21(2):239–245, May 1979.

[70] M Meredith, M E Rabaglia, and S A Metz. Evidence of a role for GTP in the potentiation of ca(2+)-induced insulin secretion by glucose in intact rat islets. *Journal of Clinical Investigation*, 96(2):811–821, August 1995. PMID: 7635976 PMCID: PMC185267.

[71] Nicholas Metropolis, Arianna W. Rosenbluth, Marshall N. Rosenbluth, Augusta H. Teller, and Edward Teller. Equation of state calculations by fast computing machines. *The Journal of Chemical Physics*, 21(6):1087–1092, June 1953.

[72] R. Milner and C. Hales. The role of calcium and magnesium in insulin secretion from rabbit pancreas studied in vitro. *Diabetologia*, 3(1):47–49, 1967.

[73] J Monod, J Wyman, and J P Changeux. On the nature of allosteric transitions: a plausible model. *Journal of molecular biology*, 12:88–118, May 1965. PMID: 14343300.

[74] Ramon E. Moore, R. Baker Kearfott, and Michael J. Cloud. *Introduction to Interval Analysis*. SIAM, April 2009.

[75] Anne Morgat, Eric Coissac, Elisabeth Coudert, Kristian B. Axelsen, Guillaume Keller, Amos Bairoch, Alan Bridge, Lydie Bougueleret, Ioannis Xenarios, and Alain Viari. Unipathway: a resource for the exploration and annotation of metabolic pathways. *Nucleic Acids Research*, 40(D1):D761–D769, 2012.

[76] Deborah M Muoio and Christopher B Newgard. Mechanisms of disease: molecular and metabolic mechanisms of insulin resistance and beta-cell failure in type 2 diabetes. *Nature reviews. Molecular cell biology*, 9(3):193–205, 2008.

[77] Sachiko Nakada, Tomohisa Ishikawa, Yuri Yamamoto, Yukiko Kaneko, and Koichi Nakayama. Constitutive nitric oxide synthases in rat pancreatic islets: direct imaging of glucose-induced nitric oxide production in β-cells. *Pflügers Archiv European Journal of Physiology*, 447:305–311, 2003. 10.1007/s00424-003-1176-y.

[78] N.S. Nedialkov. Interval tools for odes and daes. In *Scientific Computing, Computer Arithmetic and Validated Numerics, 2006. SCAN 2006. 12th GAMM - IMACS International Symposium on*, page 4, sept. 2006.

[79] J. A. Nelder and R. Mead. A Simplex Method for Function Minimization. *The Computer Journal*, 7(4):308–313, January 1965.

[80] M. Nenquin, A. Szollosi, L. Aguilar-Bryan, J. Bryan, and J. C. Henquin. Both triggering and amplifying pathways contribute to fuel-induced insulin secretion in the absence of sulfonylurea receptor-1 in pancreatic β-cells. *J. Biol. Chem.*, 279:32316–32324, 2004.

[81] C. B. Newgard and F. M. Matschinsky. Handbook of physiology, 2001.

[82] C. B. Newgard and J. D. McGarry. Metabolic coupling factors in pancreatic β-cell signal transduction. *Annu. Rev. Biochem.*, 64:689–719, 1995.

[83] Jorge Nocedal and Stephen J. Wright. *Numerical Optimization*. Springer, 1999.

[84] Richard Pavelle, Michael Rothstein, and John Fitch. Computer algebra. *Scientific American*, 245:102–113, 1981.

[85] Renjitha Pillai, Peter Huypens, Mei Huang, Stephanie Schaefer, Tanya Sheinin, Shawn D. Wettig, and Jamie W. Joseph. Aryl hydrocarbon receptor nuclear translocator/hypoxia-inducible factor-1β plays a critical role in maintaining glucose-stimulated anaplerosis and insulin release from pancreatic β-cells. *Journal of Biological Chemistry*, 286(2):1014–1024, 2011.

[86] William H. Press. *Numerical Recipes: The Art of Scientific Computing.* Cambridge University Press, September 2007.

[87] M. E. Rabaglia. α-ketoisocaproate-induced hypersecretion of insulin by islets from diabetes-susceptible mice. *Am. J. Physiol Endocrinol. Metab.*, 289:E218–E224, 2005.

[88] Sarah M Ronnebaum, Olga Ilkayeva, Shawn C Burgess, Jamie W Joseph, Danhong Lu, Robert D Stevens, Thomas C Becker, A Dean Sherry, Christopher B Newgard, and Mette V Jensen. A Pyruvate Cycling Pathway Involving Cytosolic NADP-dependent Isocitrate Dehydrogenase Regulates Glucose-stimulated Insulin Secretion. *Journal of Biological Chemistry*, 281(41):30593–30602, 2006.

[89] Sarah M Ronnebaum, Mette V Jensen, Hans E Hohmeier, Shawn C Burgess, Yun-Ping Zhou, Su Qian, Douglas MacNeil, Andrew Howard, Nancy Thornberry, Olga Ilkayeva, Danhong Lu, a Dean Sherry, and Christopher B Newgard. Silencing of cytosolic or mitochondrial isoforms of malic enzyme has no effect on glucose-stimulated insulin secretion from rodent islets. *The Journal of biological chemistry*, 283(43):28909–17, 2008.

[90] S.M. Rump. INTLAB - INTerval LABoratory. In Tibor Csendes, editor, *Developments in Reliable Computing*, pages 77–104. Kluwer Academic Publishers, Dordrecht, 1999. `http://www.ti3.tu-harburg.de/rump/`.

[91] Jerome Sacks, William J. Welch, Toby J. Mitchell, and Henry P. Wynn. Design and analysis of computer experiments. *Statistical Science*, 4(4):pp. 409–423, 1989.

[92] A. Saltelli, S. Tarantola, and K. P.-S. Chan. A quantitative Model-Independent method for global sensitivity analysis of model output. *Technometrics*, 41(1):39–56, February 1999.

[93] Andrea Saltelli. *Global Sensitivity Analysis: The Primer*. John Wiley, March 2008.

[94] Yoshihiko Sato, Toru Aizawa, Mitsuhisa Komatsu, Naomi Okada, and Takashi Yamada. Dual functional role of membrane Depolarization/Ca2+ influx in rat pancreatic β-cell. *Diabetes*, 41(4):438–443, April 1992.

[95] Maurice Scheer, Andreas Grote, Antje Chang, Ida Schomburg, Cornelia Munaretto, Michael Rother, Carola SГцhngen, Michael Stelzer, Juliane Thiele, and Dietmar Schomburg. BRENDA, the enzyme information system in 2011. *Nucleic acids research*, 39(Database issue):D670–676, January 2011. PMID: 21062828.

[96] Maurice Scheer, Andreas Grote, Antje Chang, Ida Schomburg, Cornelia Munaretto, Michael Rother, Carola SГцhngen, Michael Stelzer, Juliane Thiele, and Dietmar Schomburg. Brenda, the enzyme information system in 2011. *Nucleic Acids Research*, 39(suppl 1):D670–D676, 2011.

[97] Henning Schmidt and Mats Jirstrand. Systems biology toolbox for MATLAB®: a computational platform for research in systems biology. *Bioinformatics*, 22(4):514–515, February 2006. `http://www.sbtoolbox2.org`.

[98] Ida Schomburg, Antje Chang, and Dietmar Schomburg. BRENDA, enzyme data and metabolic information. *Nucl. Acids Res.*, 30(1):47–49, 2002.

[99] F. Schuit. Metabolic fate of glucose in purified islet cells. glucose-regulated anaplerosis in β cells. *J. Biol. Chem.*, 272:18572–18579, 1997.

[100] Frans Schuit, Anick De Vos, Salah Farfari, Karen Moens, Daniel Pipeleers, Thierry Brun, and Marc Prentki. Metabolic fate of glucose in purified islet cells. *Journal of Biological Chemistry*, 272(30):18572–18579, 1997.

[101] N Sekine, V Cirulli, R Regazzi, L J Brown, E Gine, J Tamarit-Rodriguez, M Girotti, S Marie, M J MacDonald, and C B Wollheim. Low lactate dehydrogenase and high mitochondrial glycerol phosphate dehydrogenase in pancreatic beta-cells. potential role in nutrient sensing. *Journal of Biological Chemistry*, 269(7):4895–4902, 1994.

[102] E Selkov, S Basmanova, T Gaasterland, I Goryanin, Y Gretchkin, N Maltsev, V Nenashev, R Overbeek, E Panyushkina, L Pronevitch, Jr Selkov, E, and I Yunus. The metabolic pathway collection from EMP: the enzymes and metabolic pathways database. *Nucl. Acids Res.*, 24(1):26–28, 1996.

[103] A Sener and W J Malaisse. The coupling of metabolic to secretory events in pancreatic islets: comparison between insulin release and cytosolic redox state. *Biochemistry international*, 14(5):897–902, May 1987.

[104] L. Shampine and M. Reichelt. The matlab ode suite. *SIAM Journal on Scientific Computing*, 18(1):1–22, 1997.

[105] T. Shibasaki, Y. Sunaga, K. Fujimoto, Y. Kashima, and S. Seino. Interaction of ATP sensor, cAMP sensor, ca2+ sensor, and voltage-dependent ca2+ channel in insulin granule exocytosis. *J. Biol. Chem.*, 279:7956–7961, 2004.

[106] J. Søondergaard S.N. Lophaven, H.B. Nielsen. DACE - a matlab kriging toolbox, version 2.0. report IMM-REP-2002-12.

[107] S G Straub, R F James, M J Dunne, and G W Sharp. Glucose activates both k(atp) channel-dependent and k(atp) channel-independent signaling pathways in human islets. *Diabetes*, 47(5):758–763, 1998.

[108] I. R. Sweet and F. M. Matschinsky. Mathematical model of beta-cell glucose metabolism and insulin release. I. Glucokinase as glucosensor hypothesis. *Am J Physiol Endocrinol Metab*, 268(4):E775–788, 1995.

[109] Imre Vastrik, Peter D'Eustachio, Esther Schmidt, Geeta Joshi-Tope, Gopal Gopinath, David Croft, Bernard de Bono, Marc Gillespie, Bijay Jassal, Suzanna Lewis, Lisa Matthews, Guanming Wu, Ewan Birney, and Lincoln Stein. Reactome: a knowledge base of biologic pathways and processes. *Genome Biology*, 8(3):R39, March 2007.

[110] Pal O. Westermark, Jeanette Hellgren Kotaleski, Anneli Bjorklund, Valdemar Grill, and Anders Lansner. A mathematical model of the mitochondrial NADH shuttles and anaplerosis in the pancreatic beta-cell. *Am J Physiol Endocrinol Metab*, 292(2):E373–393, 2007.

[111] Andreas Wiederkehr and Claes B Wollheim. Minireview: implication of mitochondria in insulin secretion and action. *Endocrinology*, 147(6):2643–9, 2006.

[112] Ulrike Wittig, Martin Golebiewski, Renate Kania, Olga Krebs, Saqib Mir, Andreas Weidemann, Stefanie Anstein, Jasmin Saric, and Isabel Rojas. Sabio-rk: Integration

and curation of reaction kinetics data. In Ulf Leser, Felix Naumann, and Barbara Eckman, editors, *Data Integration in the Life Sciences*, volume 4075 of *Lecture Notes in Computer Science*, pages 94–103. Springer Berlin Heidelberg, 2006.

[113] Ulrike Wittig, Renate Kania, Martin Golebiewski, Maja Rey, Lei Shi, Lenneke Jong, Enkhjargal Algaa, Andreas Weidemann, Heidrun Sauer-Danzwith, Saqib Mir, Olga Krebs, Meik Bittkowski, Elina Wetsch, Isabel Rojas, and Wolfgang MΓëller. Sabio-rk-database for biochemical reaction kinetics. *Nucleic Acids Research*, 40(D1):D790–D796, 2012.

[114] Fan Wu, Feng Yang, Kalyan C Vinnakota, and Daniel a Beard. Computer modeling of mitochondrial tricarboxylic acid cycle, oxidative phosphorylation, metabolite transport, and electrophysiology. *The Journal of biological chemistry*, 282(34):24525–37, 2007.

[115] H Yajima, M Komatsu, T Schermerhorn, T Aizawa, T Kaneko, M Nagai, G W Sharp, and K Hashizume. cAMP enhances insulin secretion by an action on the ATP-sensitive k^+ channel-independent pathway of glucose signaling in rat pancreatic islets. *Diabetes*, 48(5):1006–1012, May 1999. PMID: 10331404.

[116] Katsuyuki Yugi and Masaru Tomita. A general computational model of mitochondrial metabolism in a whole organelle scale. *Bioinformatics*, 20(11):1795–1796, 2004.

[117] Choujun Zhan and Lam Yeung. Parameter estimation in systems biology models using spline approximation. *BMC Systems Biology*, 5(1):14, 2011.

[118] Y Zhang and A Rundell. Comparative study of parameter sensitivity analyses of the TCR-activated Erk-MAPK signalling pathway. *Systems biology*, 153(4):201–11, July 2006.